Title
Pyrogeography of California: A Study of Wildfire-Climate Dynamics

Permalink
https://escholarship.org/uc/item/4v30x6dm

Author
Rother, David

Publication Date
2023

Peer reviewed|Thesis/dissertation

SAN DIEGO STATE UNIVERSITY AND

UNIVERSITY OF CALIFORNIA

Santa Barbara

Pyrogeography of California: A Study of Wildfire-Climate Dynamics

A Dissertation submitted in partial satisfaction of the
requirements for the degree Doctor of Philosophy
in Geography

by

David E. Rother

Committee in charge:
Professor Fernando De Sales, Chair
Professor Douglas A. Stow
Professor Joseph P. McFadden
Professor Charles Jones

June 2023

The dissertation of David E. Rother is approved.

Douglas A. Stow

Joseph P. McFadden

Charles Jones

Fernando De Sales, Committee Chair

April 2023

Pyrogeography of California: A Study of Wildfire-Climate Dynamics

by

David E. Rother

ACKNOWLEDGEMENTS

The research compiled for this dissertation was made possible by San Diego State University graduate student funding and was supported by the Center for Earth Systems Analysis Research at the Department of Geography. I would like to give a special thanks to my advisor, Professor Fernando De Sales, for his mentorship and guidance through the Master's and Doctorate programs. I also want to thank my Doctorate committee members Douglas A. Stow, Joseph P. McFadden, and Charles Jones for their time and valuable input.

VITA OF DAVID E. ROTHER
April 2023

EDUCATION

Bachelor of Science, California Polytechnic State University, San Luis Obispo, June 2014
Master of Science, San Diego State University, San Diego, May 2018
Doctor of Philosophy in Geography, San Diego State University and the University of California, Santa Barbara, April 2023

PROFESSIONAL EMPLOYMENT

2016-18: Graduate Research Assistant, Department of Geography, San Diego State University, San Diego
2018-2023: Teaching Associate, Department of Geography, San Diego State University, San Diego

PUBLICATIONS

De Sales F, Rother D (2020) A new coupled modeling approach to simulate terrestrial water storage in southern California. Water 12(3): 808. https://doi.org/10.3390/w12030808.

Rother D, De Sales F (2020) Impact of wildfire on the surface energy balance in six California case studies. Boundary-Layer Meteorology 178: 143-166. https://doi.org/10.1007/s10546-020- 00562-5.

Rother DE, De Sales F, Stow D, McFadden J (2022) Impacts of burn severity on short-term postfire vegetation recovery, surface albedo, and land surface temperature in California ecoregions. PLoS One 17(11): e0274428. https://doi.org/10.1371/journal.pone.0274428

Rother DE, De Sales F, Stow D, McFadden JP (2022) Summer and Fall Extreme Fire Weather Projected to Occur More Often and Affect a Growing Portion of California throughout the 21st Century. Fire 5(6):177. https://doi.org/10.3390/fire5060177

FIELDS OF STUDY

Major Field: Geography

ABSTRACT

Pyrogeography of California: A Study of Wildfire-Climate Dynamics

by

David E. Rother

Annual area burned has increased in California over the past three decades as a result of rising temperatures and a greater atmospheric demand for moisture, a trend that is projected to continue throughout the 21st century as a result of climate change. However, the impacts of climate on the size, severity, and seasonality of wildfire activity are strongly influenced by ecosystem, predominant vegetation types, weather patterns, topography, and human activity. The individual wildfire burned perimeter and ecoregion-level spatial scales adopted for this research increases the amount of local information, as well as the resolution with which fire and land managers can implement strategies and counter measures when addressing issues related to climate change. This research combines 18 years of wildfire burned area perimeter maps, high resolution land surface modeling, a suite of remote sensing datasets, and nearly a century of statistically downscaled climatological data in an effort to quantify the impact of wildfire on local meteorology, as well as the influence of climate change on extreme fire weather.

This dissertation investigates the bi-directional climate-wildfire feedback system in California through a detailed examination of the impacts of wildfire on the surface energy balance, an assessment of the influence of wildfire burn severity on the five-year postfire trajectory of three biophysical variables, and the quantification of the impacts of climate change on extreme fire weather. Results indicate that the largest changes to net radiation in the four months following ignition were primarily caused by decreases in latent heat flux following wildfire-induced vegetation removal. This vegetation removal, coupled with the lowering of albedo from ash deposition, also contributed to decreases in sensible heat flux. Further, vegetation abundance and land surface temperature did not return to prefire levels, for any burn severity class, after five years. Lastly, this work provides evidence that fire weather conditions conducive to large wildfires will become more extreme and extend later into the fall season in most areas of California by 2100. The methods of investigation used here may be applied to other regions of the world in an effort to inform the mitigation and suppression of large wildfires.

TABLE OF CONTENTS

LIST OF FIGURES

LIST OF TABLES

Chapter 1. Introduction

Wildfire is one of the primary causes of ecosystem disturbance and is inextricably linked to climate on short- and long-term time scales (Zhong et al. 2021). Over long periods of time, regional climate shapes the bounds of weather and vegetation, thus directly and indirectly influencing the size, intensity, frequency, and mean annual area burned by wildfire (Zhong et al. 2021; Bradstock 2010; Keeley 2009). Over shorter periods, weather conditions such as low relative humidity, high wind speeds, and high temperatures can dry out fuels and increase the probability of wildfire ignition and spread (Flannigan et al. 2009). Additionally, the disturbances wrought by wildfire on the land surface contribute to substantial alterations to energy, water, and carbon flux, perpetuating a cycle where wildfire alternates between driving meteorological change and responding to it (Archibald et al. 2013; Hurteau et al. 2019). In other words, wildfire-induced modifications to the land surface results in changes to biophysical properties like albedo, surface roughness, leaf area index, and the partitioning of energy into latent and sensible heat flux, which not only impacts local meteorology, but the continuity and flammability of fuels for future burning (Keeley and Syphard 2016).

The complex inter-connections between wildfire, vegetation, and weather conditions are further complicated by climate change. Over the last several decades, climate change has led to increases in fuel aridity, a longer fire season, and a growing number of extreme fire weather days each year, which have contributed to a greater total annual burned area (Goss et al. 2020; Abatzoglou and Williams 2016; Jolly et al. 2015). Furthermore, future climate change is projected to continue to impact fire intensity, the probability of extreme fire weather, and total annual burned area through the effects of drought and increased fuel aridity (Westerling and Bryant 2008; Miller and Schlegel 2006; Goss et al. 2020; Lenihan et al. 2008). However, studies attempting to predict future wildfire activity are subject to significant uncertainty stemming from issues of climate and vegetation non-stationarity, the self-regulating nature of wildfire, and the emergence of novel ecosystem states that are likely to emerge as a result of a changing climate and wildfire-induced shifts in vegetation distribution (Hurteau et al. 2019; Parks et al. 2016; Stevens-Rumann et al. 2016; Williams et al. 2007). As global climate change continues to contribute to increases in temperature and atmospheric aridity, it is critical that we understand how the drivers of wildfire vary among fine-scale ecological contexts so that strategies for the management and suppression of wildfire may be adapted to fit unique fire regimes.

This dissertation investigates the bi-directional climate-wildfire feedback system in California and has three primary objectives: (1) examine the impacts of wildfire on the surface energy balance in California; (2) assess the influence of wildfire burn severity on the five-year postfire trajectory of three biophysical variables: vegetation presence, land surface albedo, and land surface temperature; and (3) quantify and evaluate the past and expected impacts of climate change on the occurrence of extreme fire weather during an historical (1979-2014), mid-century (2041-2070), and late-century (2071-2100) period. This research combines 18 years of wildfire burned area perimeter maps, high resolution land surface modeling, a suite of remote sensing datasets, and nearly a century of statistically downscaled climatological data in an effort to quantify the impact of wildfire on local meteorology, as well as the influence of climate and climate change on wildfire occurrence.

The first objective of examining the impacts of wildfire on the surface energy balance after six historically large wildfires in California is described in Chapter 2 and is titled “Impact of wildfire on the surface energy balance in six California case studies.” The primary methodology utilized in Chapter 2 is a land surface model that has been modified to simulate the removal of vegetation and the deposition of ash within wildfire perimeters. The second objective of assessing the influence of wildfire burn severity on the postfire trajectory of three biophysical variables is addressed in Chapter 3, titled "Impacts of burn severity on short-term postfire vegetation recovery, surface albedo, and land surface temperature in California Ecoregions." In this chapter, a burn severity index, called the Relative Differenced Normalized Burn Ratio (RdNBR), was calculated at a 500-m spatial resolution for the entire state of California for 18 years. This burn severity index was used in conjunction with wildfire burned perimeters, vegetation abundance, land surface temperature, and surface shortwave albedo, to evaluate the temporal patterns of recovery after wildfires of varying degrees of severity. In Chapter 3, titled "Summer and Fall extreme fire weather projected to occur more often and affect a growing portion of California throughout the 21st century", nearly a century of historical and projected meteorological data was bias-corrected and statistically downscaled for input into two fire weather indices, vapor pressure deficit (VPD) and the Canadian Fire Weather Index System (FWI). These two indices were used to investigate where and when California will likely experience increases in the occurrence of extreme fire weather. Lastly, Chapter 5 includes a summary of results, critical findings, and concluding remarks.

Chapter 2. Impact of Wildfire on Surface Energy Balance in Six California Case Studies

2.1 Introduction

Wildfires are a destructive, costly, and sometimes fatal cause of ecosystem disturbance, and the expanding wildland-urban interface is placing a greater number of people at risk for being directly impacted by the negative effects of catastrophic wildfire (Westerling et al. 2006; Bendix and Commons 2017; Havel et al. 2018; Hostetler et al. 2018; Flint et al. 2019). In fact, wildfire activity in the western United States has increased in both frequency and total area burned, an increase that is often attributed to climatic changes such as warming temperatures and decreasing levels of precipitation (Westerling et al. 2006; Westerling and Bryant 2008; Abatzoglou and Kolden 2013; Arnold et al. 2014; Jensen et al. 2018; Flint et al. 2019). The effects of these changes can lead to a greater likelihood of high severity fire by increasing fuel aridity and subsequently leading to wildfires of greater intensity (van Mantgem et al. 2013; Abatzoglou et al. 2017). The impacts of recent wildfire activity have become increasingly evident in California, where nine of the ten largest wildfires in the state have occurred since 2000, and approximately 56,000 square kilometers have burned (Jin et al. 2015; CAL FIRE 2022; Flint et al. 2019).

The abundant diversity of California's ecosystems, topography, climate, and fuel characteristics contribute to a broad range of fire regimes. In southern California, the primary driver of wildfire is Santa Ana winds, which peak in December but can impact wildfire activity year-round (Dennison et al. 2008). Following on the tail of seasonal drought, high wind speeds coupled with low live fuel moisture content create conditions conducive to rapid spread of wildfire (Dennison et al. 2008; Jin et al. 2015; Williams et al. 2016). These clear climate-fire relationships often influence the size and severity of California wildfires, with larger, longer-lasting fires typically burning in autumn, while spring fires are, in general, more easily contained due to vegetation's higher fuel moisture content (Dennison et al. 2008; Keeley et al. 2009). However, not only do regional fire regimes affect annual area burned, the resulting disturbance to vegetation communities weakens resilience, alters species distribution, and changes regenerative patterns post-fire (Syphard et al. 2006). In fact, studies have shown that increases in fire frequency (i.e., short-interval fire recurrence of fewer than eight years) can lead to the proliferation of non-native species, as well as widespread loss of native vegetation (Syphard et al. 2006; Lippitt et al. 2013; Meng et al. 2014).

The most immediate effect of wildfire on the land surface is the removal of vegetation and the subsequent deposition of a layer of charcoal or ash (De Sales et al. 2018). Vegetation loss reduces transpiration and canopy interception while simultaneously increasing sensible heat flux, an effect that is magnified by the seasonality of vegetation growth, especially in the summer (Liu et al. 2018). The subsequent changes in surface roughness directly affects interactions between the land surface and the atmosphere by reducing the amount of turbulence at the surface, suppressing convection, and reducing net radiation (Chambers et al. 2005). Furthermore, the deposition of ash on the land surface lowers albedo, which alters the partitioning of energy into latent and sensible heat (Intergovernmental Panel on Climate Change (IPCC) 2001; Jin and Roy 2005). Impacts on post-fire surface albedo are complex, as burn severity, pre-fire vegetation structure (including density and height), soil moisture, and post-fire vegetation recovery all play a role in the degree of change (Jin and Roy 2005). In addition, albedo changes are directly linked to the distribution of net radiation and land surface temperature (Chambers et al. 2005; Liu et al. 2018). The period of time that ash remains on the surface varies widely, as its dispersal is almost entirely dependent on the erosive power of wind and rain (Bodí et al. 2014).

The wildfires investigated in this study range in size from approximately 660 to 1105 square kilometers. Burned scars of this size reduce surface roughness, decrease turbulent flow in the surface boundary layer, and increase wind speeds (Anthes 1984). These effects are amplified among California's varied topography where the removal of vegetation combined with steep slopes can contribute to stronger Santa Ana and offshore winds. In contrast, vegetated land surfaces decrease wind speeds and promote convective precipitation because of the greater turbulence intensity (Anthes 1984). As other large wildfires occur around the world (e.g., Thomas Fire in Santa Barbara, 2018; Amazon rainforest fires in 2019; Australia bushfires in 2020), the resulting burn scars can potentially alter boundary layer dynamics and diurnal cycles of turbulent fluxes (Stull 1988; Chambers and Chapin 2003; De Sales et al. 2016). The effect of wildfire burn scars on the land surface is similar to that of desertification. California's seasonal drought, coupled with warm and dry Mediterranean summers, puts the state at risk of entering a feedback loop in which newly burned scars contribute to the suppression of rainfall and the exacerbation of existing aridity (Anthes 1984; Dennison et al. 2008).

In general, studies investigating the impact of wildfire on albedo and radiation balance have not utilized land-surface modelling tools. However, these models' ability to simulate critical biophysical processes allows for comprehensive representation of wildfire impacts on the land surface (Jin and Roy 2005). The goal of this study is to explore the effects of six historic California wildfires on surface radiation balance (expressed through latent, sensible, and ground heat fluxes) through a series of land surface model simulations. The third version of the Simplified Simple Biosphere (SSiB3) vegetation biophysical model, along with daily burned area fraction derived from the MODIS approximate date of burning dataset (MCD64), were used to investigate the differences between a burned and unburned scenario. For each wildfire, a control experiment (undisturbed vegetation) and a burned experiment (vegetation removal and recovery, ash deposition and removal) were performed in order to assess the physical changes to local land surface processes caused by wildfire.

2.1.1 Study Area

The general area of interest in this study is California, where climate varies widely on a north-south and east-west gradient, with cool and wet conditions in the north-west that gradually transitions to warmer and drier conditions in the south-east, resulting in diverse land cover type distributions (Figure 1a). The northern and north-western portions of the state are predominantly covered by forests, while shrublands are widespread in the south and south-east. Similarly, vegetation cover fraction is greatest in the north-west and lowest in the south-east (Figure 1b). Three major mountain ranges traverse sections of the state of California, including the Sierra Nevada, the Coastal Range, and the Transverse Range (Figure 1c). California's diverse climate, coupled with large variability in vegetation cover and topography, has a strong influence on fuel moisture, relative humidity, surface roughness, and wind speeds (Dennison et al. 2008; Williams et al. 2019).

Six of the largest wildfires in California's recorded history were selected for closer examination as individual case studies (Table 1). The primary criterion for selection (apart from total area burned) was date of occurrence, as each simulation required four years of forcing data extending beyond the ignition date.

Table 1. Wildfire name, location (county), date of ignition, and area burned (CALFIRE 2022).

Fire	Location	Date	Area Burned [km^2]
Zaca Fire	Santa Barbara	July 2007	972.08
Witch Fire	San Diego	October 2007	801.24
Rim Fire	Tuolumne	August 2013	1041.31
Cedar Fire	San Diego	October 2003	1105.79
Rush Fire	Lassen	August 2012	1100.38
Basin Complex Fire	Monterrey	June 2008	658.90

Each case study is characterized by different predominant vegetation type, vegetation cover fraction, and topography (Hansen et al. 2000; Davis et al. 2019). While the Zaca, Witch, and Cedar case studies' primary vegetation type is shrubland, the Rim and Basin Complex case study areas are characterized by a combination of evergreen trees and shrub land cover. On the other hand, the Rush case study's vegetation distribution is predominately comprised of a mixture of shrublands, grasslands, and bare ground. In general, vegetation cover fraction is larger in the wetter northern fire sites and decreases southward where the climate is drier. The Rush fire is the exception, as its location on the leeside of the Sierra Nevada contributes to a drier climate, and therefore, low vegetation cover fraction.

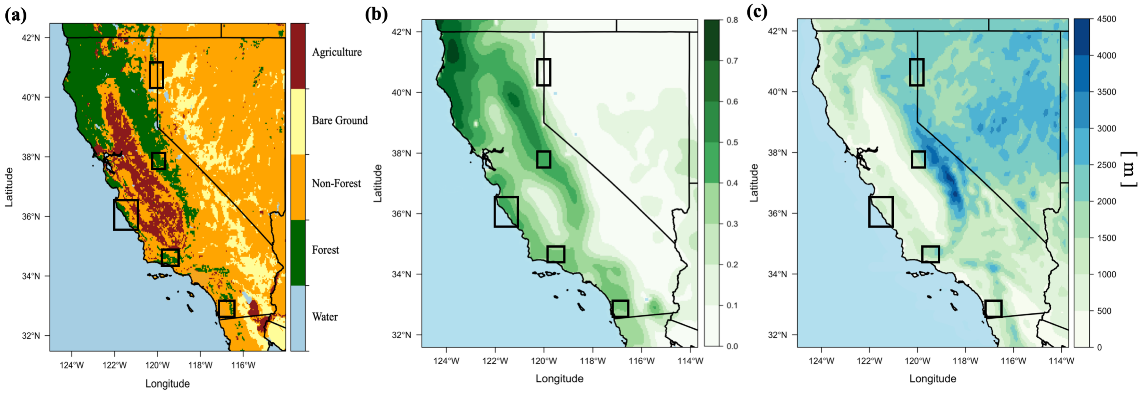

Figure 1. Study area map with wildfire case studies outlined: (a) Predominant vegetation category, (b) vegetation cover fraction, and (c) topography. In (a) the forest category includes needle-leaf evergreen and broadleaf deciduous trees, while non-forest includes grasslands, shrublands, and urban areas. Rectangles locate the six California case

studies. From north to south: Rush fire, Rim fire, Basin Complex fire, Zaca fire, and Cedar and Witch fires.

2.2 Data and Methods

2.2.1 Burned-Area Fraction

Burned area fraction (BAF) information for this study was obtained from the Moderate Resolution Imaging Spectroradiometer (MODIS) MCD64A1 product, which is available through the University of Maryland website (http://modis-fire.umd.edu). The dataset provides 500-m resolution maps of the approximate date of burning, which are retrieved by locating the occurrence of rapid changes in daily surface reflectance time series as described by Roy et al. (2002, 2008). The methodology used to generate the BAF maps from MCD64A1 is described in De Sales et al. (2016). In short, binary burned-unburned maps are aggregated to the model's resolution using a grid-cell averaging function, and subsequently implemented into the model's forcing data and onto the model's grid. In this way, monthly burned area fraction is interpolated to daily values and relayed to the model at regular intervals. Burned area fraction for the years 2003 to 2017 were calculated using this method.

Burned area fraction is largest in 2003, 2008, and 2012, with specific individual large fires accounting for large percentages of each year's total burned area (Figure 2a).

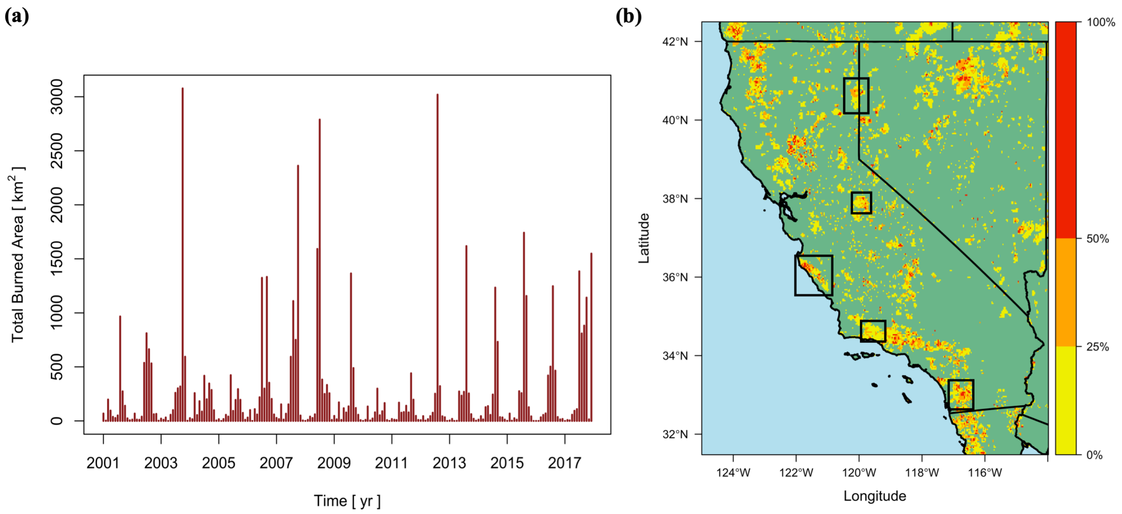

Figure 2. (a) Monthly total burned area within the California state boundary for January 2001 through December 2017. (b) Spatial distribution of total burned area including the recurrence interval for each pixel. Scale bar indicates the percentage of the total months that each pixel burned. Rectangles locate the six California case studies. From north to south: Rush fire, Rim fire, Basin Complex fire, Zaca fire, and Cedar and Witch fires.

From 2001 through 2017, wildfire is observed throughout California except the south-east area, where large swaths of sparsely vegetated desert ecosystems inhibit the occurrence of large fires. Small regions in southern, central, and northern California burned repeatedly (Figure 2b). It is not unusual for wildfires to reburn extensive areas affected in previous years. For example, the Witch fire in San Diego (2007) reburned approximately 300 km^2 of 2002, 2003, and 2004 burned scars (Keeley et al. 2009).

Wildfires burn more area within the forest land cover group than non-forest or agriculture (Figure 3).

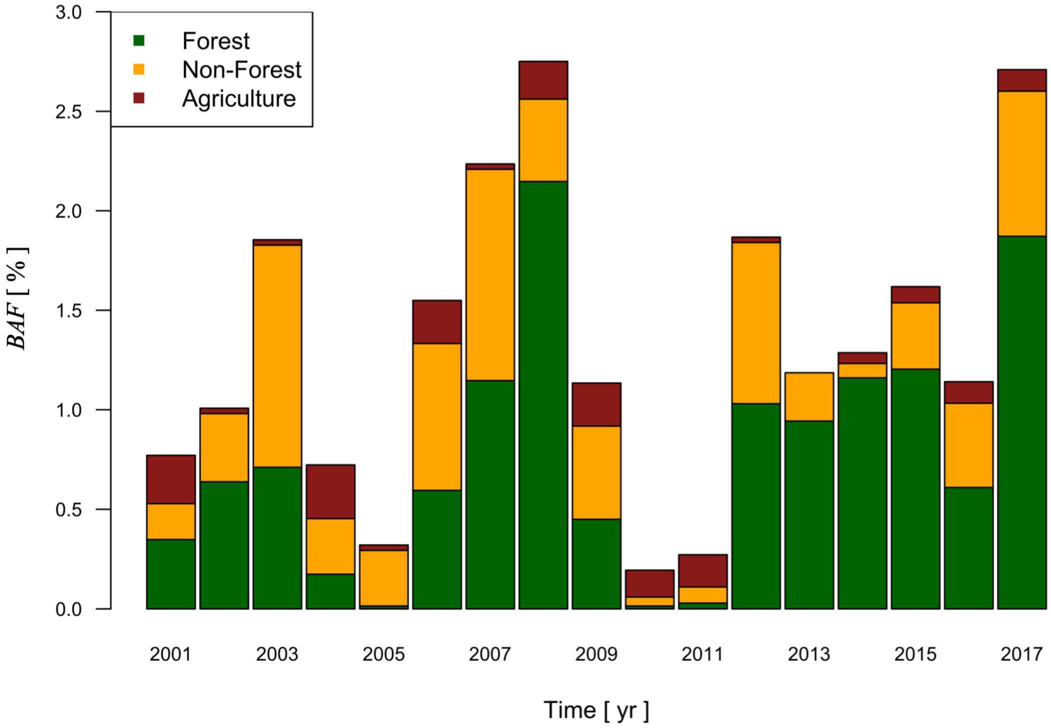

Figure 3. California state-wide average BAF extent per land cover type between 2001 and 2017.

Additionally, 2008 and 2017 were the only years that burned more than 2.5% of any combination of forest, non-forest, or agriculture types, with the greatest amount of forested land cover burned than any other year. The greatest percentage of wildfires occur in August in northern and central California, and October in southern California (Figure 4).

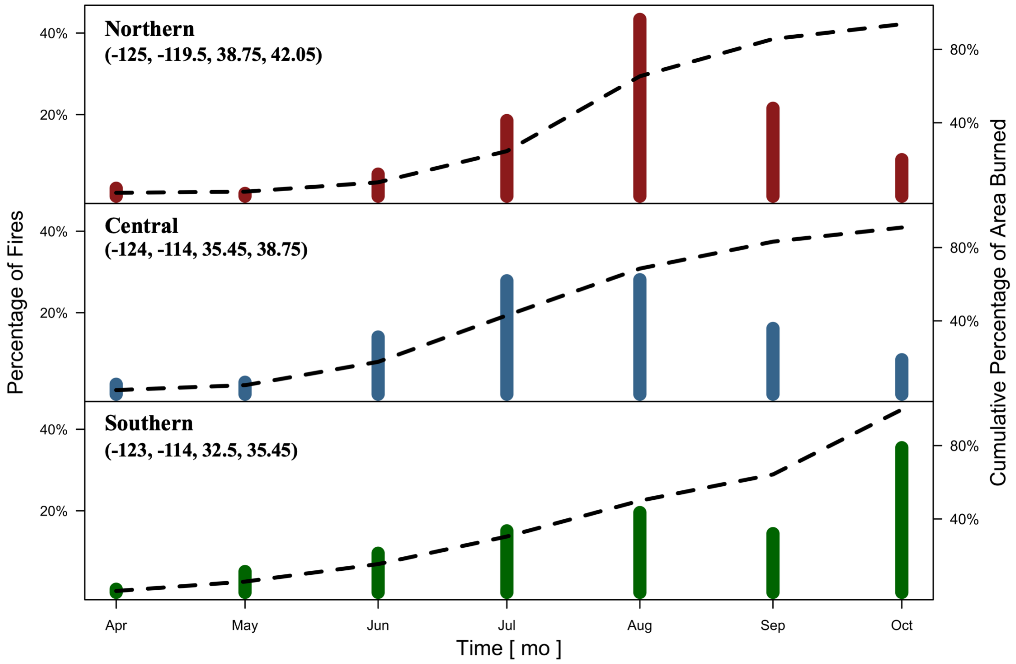

Figure 4. 2001-2017 monthly burned area fraction climatology. Left side axis represents percentage of wildfire burned area that occurred in each month in California between 2001 and 2017. Right side axis represents the cumulative percentage of area burned over the seven months shown.

Southern California's low levels of precipitation (4.7 mm mo^{-1}) and high summertime temperatures (approximately 27 °C on average), coupled with strong Santa Ana winds, drive intense autumn wildfires that are difficult to contain (Daly et al. 1997; Keeley et al. 2009). Furthermore, warm spring and summertime temperatures, coupled with dry conditions, during and preceding the fire season, decrease fuel moisture and are the primary drivers of wildfire activity in northern and central California forests (Trouet et al. 2006; Keeley and Syphard 2016). In contrast, from November to March, California experiences no significant amount of wildfire. With some exceptions (i.e., Thomas Fire, Santa Barbara, December 2017 – January 2018), relatively moist winter conditions aid fire suppression and act as a deterrent to the growth of large wildfires.

2.2.2 Vegetation Recovery and Ash Deposition

All MODIS enhanced vegetation index (MOD13A1) and the surface albedo (MOD43A3) products are utilized to calculate the vegetation recovery and ash residence time for the model experiments. The enhanced vegetation index (EVI) product is a 16-day, 500-m spatial resolution dataset that has improved sensitivity over the Normalized Difference Vegetation Index in both densely and sparsely vegetated areas due to the detachment of the canopy from the soil background (Jin et al. 2012; Didan 2015; Dintwe et al. 2017). The enhanced vegetation index reduces atmospheric background noise while retaining details concerning canopy structure, land cover, and vegetation seasonality and biophysics (Kinoshita and Hogue 2011). The dataset is used in this study to calculate post-fire vegetation recovery for the different case studies, as described in this section.

The MODIS surface albedo model product is a daily, 500-m resolution dataset that contains black and white-sky albedo for MODIS bands 1-7 and the visible, near infrared, and shortwave bands (Schaaf and Wang 2015). The shortwave albedo product was chosen for this study because it has been used successfully in previous research to obtain values for post-fire albedo recovery (Lyons et al. 2008; Samain et al. 2008; Jin et al. 2012; Gatebe et al. 2014; Huang et al. 2015; Dintwe et al. 2017).

A similar methodology to that described in Dintwe et al. (2017) is used to obtain the average recovery period for vegetation and surface albedo within each case study domain (Figure 5).

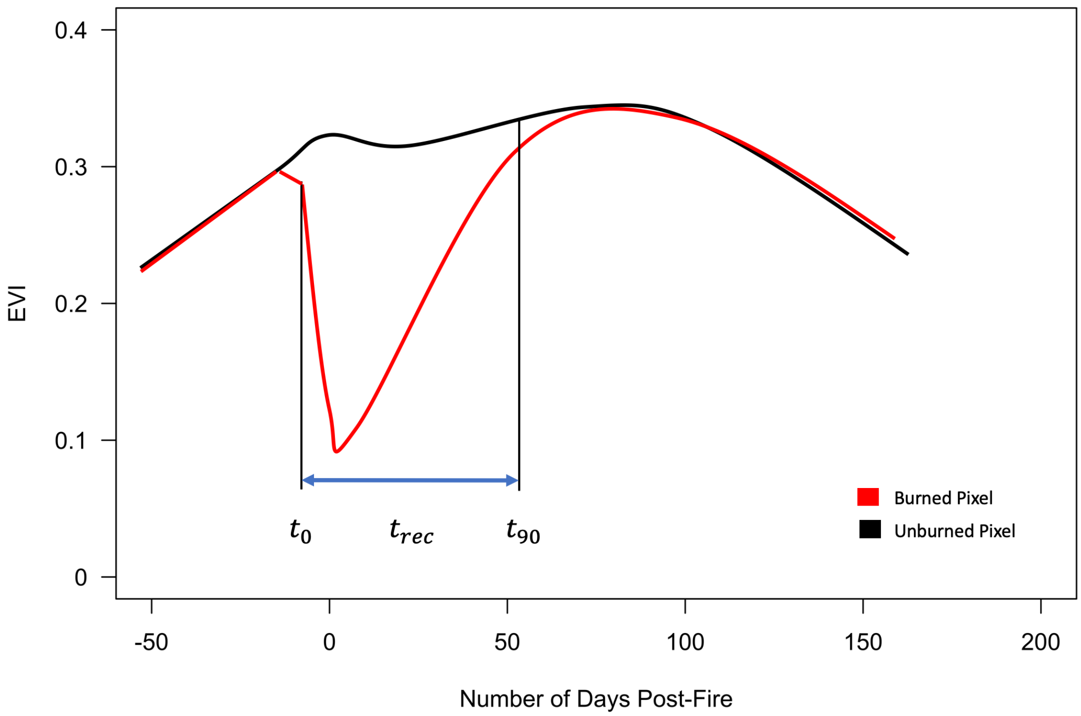

Figure 5. Diagram depicting the methodology used to obtain the average recovery interval for EVI and shortwave albedo within each case study domain.

First, an arbitrary number of burn pixels distributed throughout each burned area are selected. A 1-km buffer is applied to each selected pixel so that the EVI or albedo value at multiple points are included in an average, which is done to increase the representativeness of the burned pixel samples and to decrease the noise in the data. Next, neighbouring unburned pixels are selected from outside the burned area. Unburned pixels were considered valid if they displayed similar EVI or albedo signals as the burned pixels over a period of two years prior to the fire (Gatebe et al. 2014). Time series comparisons of burned and unburned points indicate a clear date of burn (t_0) as well as a date at which EVI and albedo values return to within 90% of the unburned pixel (t_{90}), which are used to calculate the recovery time (t_{rec}):

$$t_{rec} = t_{90} - t_0 \tag{1}$$

The average recovery period was obtained using Eq. 1 for all selected burned points for both EVI and surface albedo (Table 2). The interval of time that land surface albedo is disturbed ranges from 46 to 279 days. The Zaca case study has the shortest albedo disturbance period of 46 days, while the Rush case study has the longest, with 279 days. Vegetation recovery periods are generally longer and range from 221 to 890 days. The Rim case study has the longest vegetation recovery period of 890 days, and the Rush case study has the shortest, with 221 days (Table 2).

Table 2. Ash removal and vegetation recovery period for each case study. Units: day.

Fire Name	Ash removal	Vegetation recovery
Zaca Fire	46 ± 32.8	695 ± 170.5
Witch Fire	51 ± 36.6	328 ± 159.8
Rim Fire	183 ± 61.4	890 ± 212.4
Cedar Fire	60 ± 26.4	338 ± 144.9
Rush Fire	279 ± 66.9	221 ± 83.9
Basin Complex Fire	171 ± 66.9	664 ± 279.9

2.2.3 Simplified Simple Biosphere Model

The Simplified Simple Biosphere land surface model (SSiB) is used to calculate the effects of wildfires on the surface heat fluxes. The model employs satellite-derived leaf area index and vegetation cover fraction as surface boundary conditions for all simulations, and to describe the seasonal state of vegetation (Xue et al. 1991; Xu et al. 2014). The satellite-based vegetation classification map has a resolution of approximately 5-km and contains 12 distinct land cover types that are generated from Advanced Very High Resolution Radiometer satellite measurements (Hansen et al. 2000). The North American Regional Reanalysis dataset is used as forcing and initial conditions for all simulations (Mesinger et al. 2006).

In addition to a California-wide 10-km resolution domain, which is used to assess the model's performance, separate 1-km resolution domains are created for each individual fire in the case study and used to assess post-fire impacts on the surface energy balance.

2.3 Experimental Design

Two different experiments were conducted to examine the effects of burned area on radiation balance after six historic California wildfires. The first experiment was treated as a control simulation, with no disturbances to vegetation or surface albedo following the fire. The conditions in this simulation are meant to represent unburned, observable conditions and are a baseline with which the burned experiments are compared. This experiment is referred to as the unburned or control simulation.

The defining components of the second experiment (referred to as the burned experiment) are the removal and recovery of vegetation, as well as the deposition and removal of a layer of ash on the land surface. The burning of vegetation is simulated by depleting the leaf area index (LAI) and vegetation cover fraction every 24 hours, following Eq. 2, where LAI_U, BAF, and SR represent the unburned LAI, burned area fraction, and the vegetation survival rate, respectively. Values of SR are listed in De Sales et al. (2016). A similar equation is used to degrade vegetation cover fraction:

$$LAI = LAI_U \; [1 - BAF\,(1 - SR)] \tag{2}$$

Ash deposition is represented in the model through a darkening of the land surface in the model grid cells registering burned area, which is in accordance with the changes in surface reflectance associated with albedo decrease post-fire (Govaerts et al. 2002; De Sales et al. 2018). In the interval of time after a fire and before the removal of ash, shortwave and near-infrared surface albedo are arbitrarily set to 0.1 to simulate the decrease in surface reflectance caused by charcoal and ash (De Sales et al. 2016, 2018). After each fire's unique albedo recovery time has elapsed, the albedo of the land surface transitions to that of bare ground until vegetation recovers, a methodology used to imitate the removal of ash deposition by wind and rain (Bodí et al. 2014). Vegetation recovery and ash residence time (obtained using the methodology describe in section 2.2.2) for each individual wildfire inform the model and provide a more accurate and complete picture of vegetation dynamics, as well as the biophysical processes characterizing each location (Dintwe et al. 2017).

2.4 Results

2.4.1 Model Performance

Before analyzing the impacts of fire, we evaluate the model's performance under unburned conditions. A 7-year SSiB simulation for the entire state of California is validated here against the North American Land Data Assimilation (NLDAS) dataset (Mesinger et al. 2006). Monthly averages of temperature and net radiation are compared to NLDAS for the time period of March 2005 through December 2012. These climate variables were chosen for validation because they are the focus of this burned area impact assessment. It is important to establish the SSiB as a reliable tool with which to run experiments, while simultaneously gaining a better understanding of meteorological patterns and possible areas of uncertainty in the model.

The SSiB is able to simulate temperature throughout the state of California, with the greatest difference from the NLDAS average appearing in the high elevation areas of the Sierra Nevada Mountains, located in the eastern portion of central California, where temperature tends to be overestimated (Figure 6a).

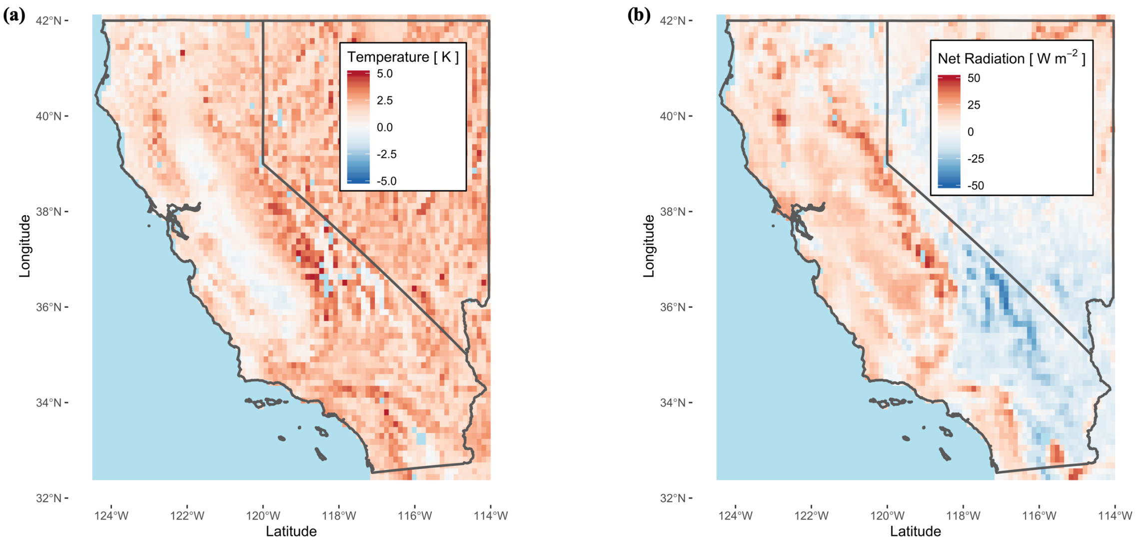

Figure 6. Average annual (a) temperature and (b) net radiation difference between control simulation and the NLDAS dataset for March 2005 – December 2012.

This area also exhibits positive biases in surface net radiation, while the south-eastern region is underestimated to roughly the same degree. These discrepancies between the model and NLDAS could potentially be caused by differences in the resolution of each respective topography and land cover representation (Xia et al. 2012).

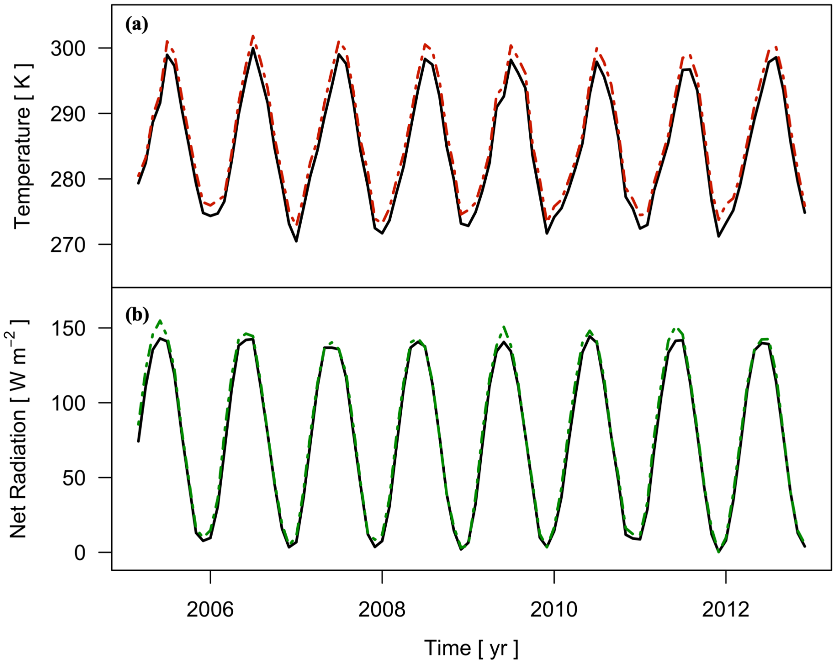

Figure 7. NLDAS and SSiB datasets for the entire state of California for the period of March 2005 through December 2012. (a) temperature (red) (b) net radiation (green). Solid lines represent the NLDAS dataset, while the dashed lines represent the SSiB simulation.

Time series comparisons of the two datasets show slight overestimation of temperature in the summer and underestimation in the winter, while net radiation is very well simulated throughout the duration of the test period (Figures 7a, b).

California-average monthly bias, root-mean-square error, and correlation coefficient between SSiB and NLDAS were calculated to further test the model's performance (Table 3).

Table 3. Bias, root-mean-square error, and correlation for NLDAS data and SSiB control simulation.

Variable	Metric	
Temperature [K]	Bias	1.83
	RMSE	1.87
	Cor	0.99
Net Radiation [W m^{-2}]	Bias	3.91
	RMSE	5.12
	Cor	0.99

On average, the model overestimates temperature and net radiation by 1.83 K and 3.91 W m^{-2}, respectively. The annual cycles of both variables are well simulated by the model (r^2 = 0.99, $p < 0.001$).

Overall, these results indicate that the SSiB land surface model is capable of accurately simulating the net radiation balance and temperature of California and can be used to reliably assess the impact of wildfire burned area on the region's energy balance.

2.4.2 Wildfire Impacts

Burned simulations, characterized by the removal and recovery of both vegetation and a layer of ash, were performed for each of the six historic California wildfires. In an effort to understand the impacts that wildfire burned area have on land surface-atmosphere energy exchange, the partitioning of radiation into sensible and latent heat flux is analyzed for each fire. The mean difference between burned and unburned simulations provides information on whether the overall change in energy balance was positive or negative, while maximum and minimum difference indicates the general range of the fluctuation from the control. A spatial and temporal difference between burned and unburned LAI aids in the analysis.

Spatial distributions of monthly average latent heat flux spanning the duration of the vegetation recovery period shows a decrease in all of the burned areas within each case study domain, except for the Rush Fire where there was an average increase of 0.5 W m^{-2} and a minimum difference of -5.0 W m^{-2} (Fig. 8e). The prevalence of non-forest type vegetation (including groundcover, broadleaf shrubs with bare soil, and broadleaf shrubs with ground cover), a small mean change in LAI, and low vegetation cover fraction may contribute to the distinct patterns of change in the Rush case study.

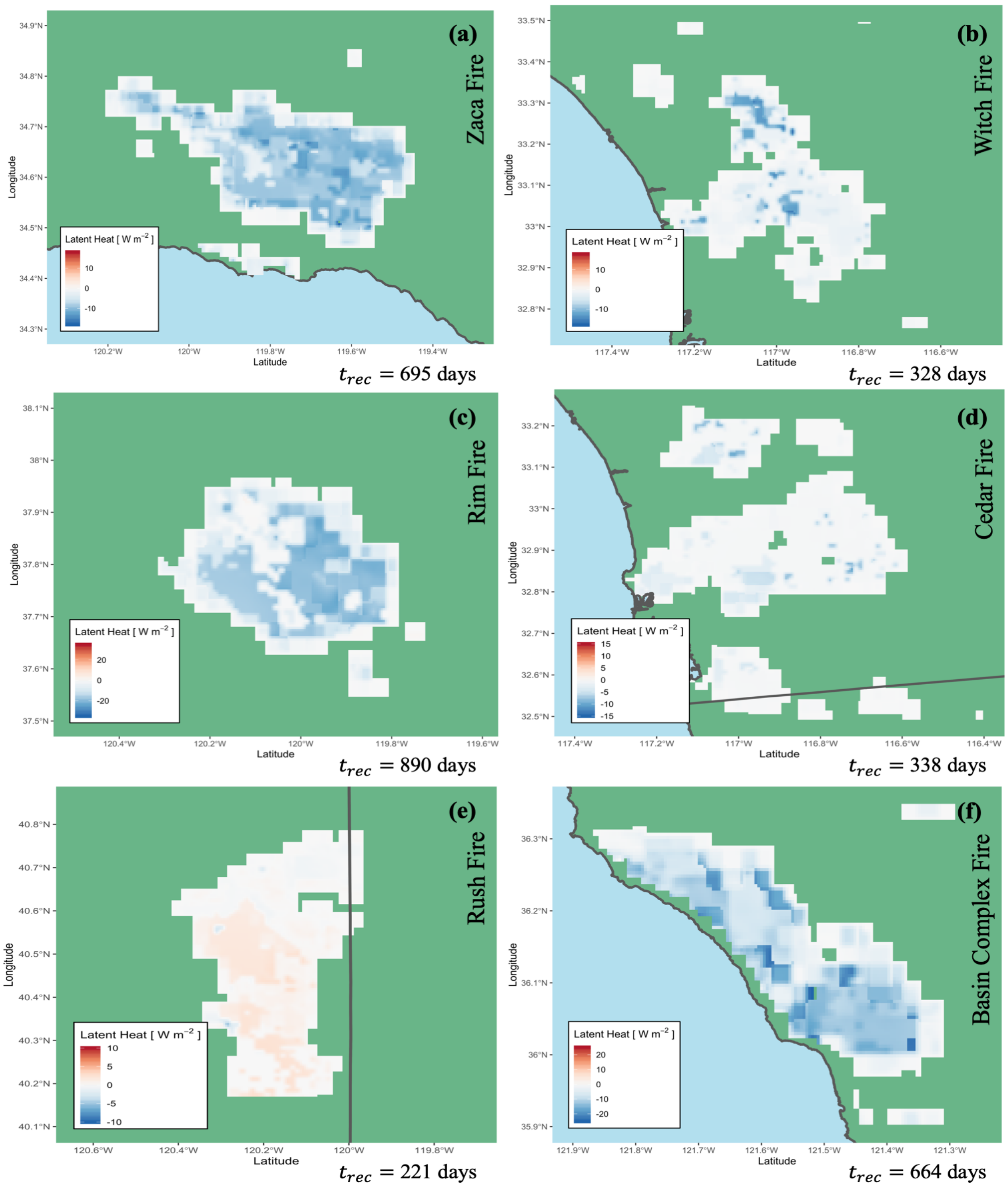

Figure 8. Difference between the burned and unburned latent heat flux (a) Zaca, (b) Witch, (c) Rim, (d) Cedar, (e) Rush, and (f) Basin Complex fires.

The Witch and the Cedar fires have similar minimum differences of -16.6 and -10.2 W m^{-2}, respectively, while the Zaca, Rim, and Basin Complex fires have larger minimum differences of -18.4, -24.0, and -25.2 W m^{-2}, respectively (Table 4). The Witch and Cedar burned areas have similar vegetation type distributions, however, the Witch study has a larger percentage of needle-leaf evergreen tree cover. The Zaca, Rim, and Basin Complex studies contain the largest amount of forest-type vegetation covers.

Table 4. Mean, maximum, and minimum values obtained from the monthly average difference of latent heat flux, sensible heat flux, net radiation, and leaf area index for the burned and unburned experiments during each wildfire's unique vegetation recovery period. Spatial categories represent the difference between means of the burned and unburned simulations for the vegetation recovery period (as in Figures 8, 10, 12). Temporal categories represent the mean differences between the burned and unburned time series (as in Figures 9, 11, 13).

	Zaca	Witch	Rim	Cedar	Rush	Basin Complex
Spatial						
Latent Heat Flux						
Mean	-5.8	-1.8	-8.9	-0.7	0.5	-7.6
Min	-18.4	-16.6	-24.0	-10.2	-5.0	-25.2
Max	0.02	0.02	1.7	0.3	3.0	0.1
Sensible Heat Flux						
Mean	-1.3	-0.4	-3.0	1.5	12.7	-3.0
Min	-15.5	-10.8	-19.7	-39.3	-0.03	-22.7
Max	20.6	15.1	22.4	18.1	36.8	19.6
Net Radiation						
Mean	-7.0	-2.2	-11.9	0.9	13.2	-10.5
Min	-25.4	-23.3	-35.8	-41	-1.0	-29.3
Max	18.8	6.9	22.0	18.1	39.3	4.8
LAI						
Mean	-0.5	-0.3	-3.5	-0.6	-0.2	-0.9
Min	-1.5	-1.0	-7.1	-6.6	-2.6	-2.1
Max	-1.2	-1.4	0	0	0	0
Temporal						
Latent Heat Flux						
Mean	-7.0	-2.3	-9.8	-0.7	0.5	-7.2
Min	-17.6	-4.3	-49.9	-3.7	-0.6	-28.8
Max	-1.3	2.0	6.4	1.3	3.6	7.1
Sensible Heat Flux						
Mean	-2.8	-2.9	-8.0	-0.1	12.7	-5.9
Min	-18.2	-8.3	-47.8	-5.0	0.5	-38.5
Max	5.1	4.6	17.3	7.7	26.5	16.2
Net Radiation						
Mean	-9.7	-5.2	-17.8	-0.7	13.2	-13.0
Min	-21.3	-12.0	-41.7	-4.1	-0.7	-31.6
Max	0.5	2.7	4.2	6.8	26.5	-0.01
LAI						
Mean	-0.6	-0.4	-3.9	-0.6	-0.2	-1.0
Min	-0.8	-0.5	-4.6	-0.9	-0.2	-1.4
Max	-0.1	-0.1	-0.6	-0.4	-0.1	-0.6

The Zaca burned scar shows the most uniform distribution of latent heat flux change, with the greatest decreases occurring in the middle of the scar and little to no change on the outside of the fire perimeter (Figure 8a). According to the model's vegetation map, the greatest changes in latent heat flux within the Zaca study's domain occur in the same areas as needle-leaf evergreen trees, while the smaller changes on the outside of the burned area occur where broadleaf trees with ground cover are located. In contrast, the Cedar fire displays little to no change in large portions of its burn scar, with concentrated areas of decreased latent heat flux in the northern and central sections, where broadleaf shrubs with bare soil is the predominate vegetation type (Figure 8d). The Witch fire burned much of the same territory of San Diego county as the Cedar fire and displays similar patterns of latent heat flux change, including several areas of concentrated latent heat flux decrease (where needle-leaf evergreen trees are found), however, the Witch fire has a greater mean decrease of -1.8 W m^{-2} (Figure 8b). The Rim fire burn scar shows distinct regions that did not change within larger areas that show significant reductions in heat flux (Figure 8c). In the Rim study, needle-leaf evergreen trees are found in the areas with the greatest amount of latent heat flux change.

Time series analyses also indicate decreases in average monthly latent heat flux in all six fires except for the Rush fire, which had an average increase of 0.5 W m^{-2} (Figure 9e).

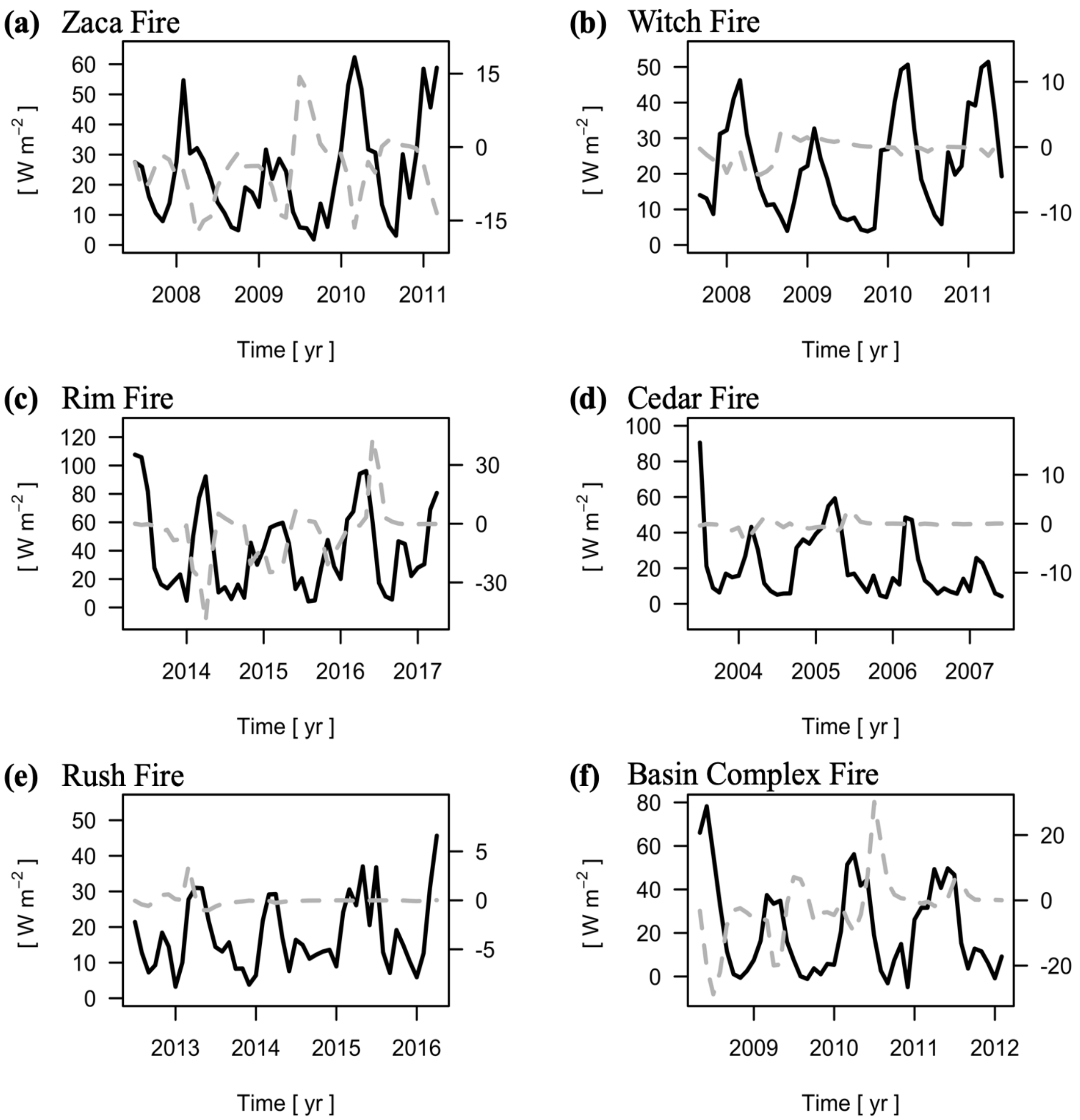

Figure 9. Average unburned latent heat flux (solid line) and the post-fire change in the flux (grey line) for the (a) Zaca, (b) Witch, (c) Rim, (d) Cedar, (e) Rush, and (f) Basin Complex fires.

The Zaca, Rim, and Basin Complex fires experience the largest minimum differences between burned and unburned experiments, with -17.6, -49.9, and -28.8 W m^{-2}, respectively. The Zaca and Basin Complex fires have periods when the latent heat flux was greater than the unburned simulation, both occurring during the summer of the third year (Figures 9a, f). The latent heat flux in the Basin Complex burned simulation, while greater than the unburned, still follows the decreasing trend of the unburned during this time, however, the Zaca burned simulation increases relative to the control. Furthermore, the Zaca fire's increase in latent heat flux relative to the unburned occurs after the vegetation recovery period, while the Basin Complex occurs during. While the greatest changes occur during the vegetation recovery period for the Witch, Cedar, Rush, and Basin Complex fires (after which the burned scenario becomes roughly equal to the unburned), the Zaca and Rim fires experience differences in latent heat flux throughout the duration of the simulation (Figures 9a, c).

The impact of burned area on sensible heat flux results in spatial heterogeneity of change in each of the six case studies (Figure 10).

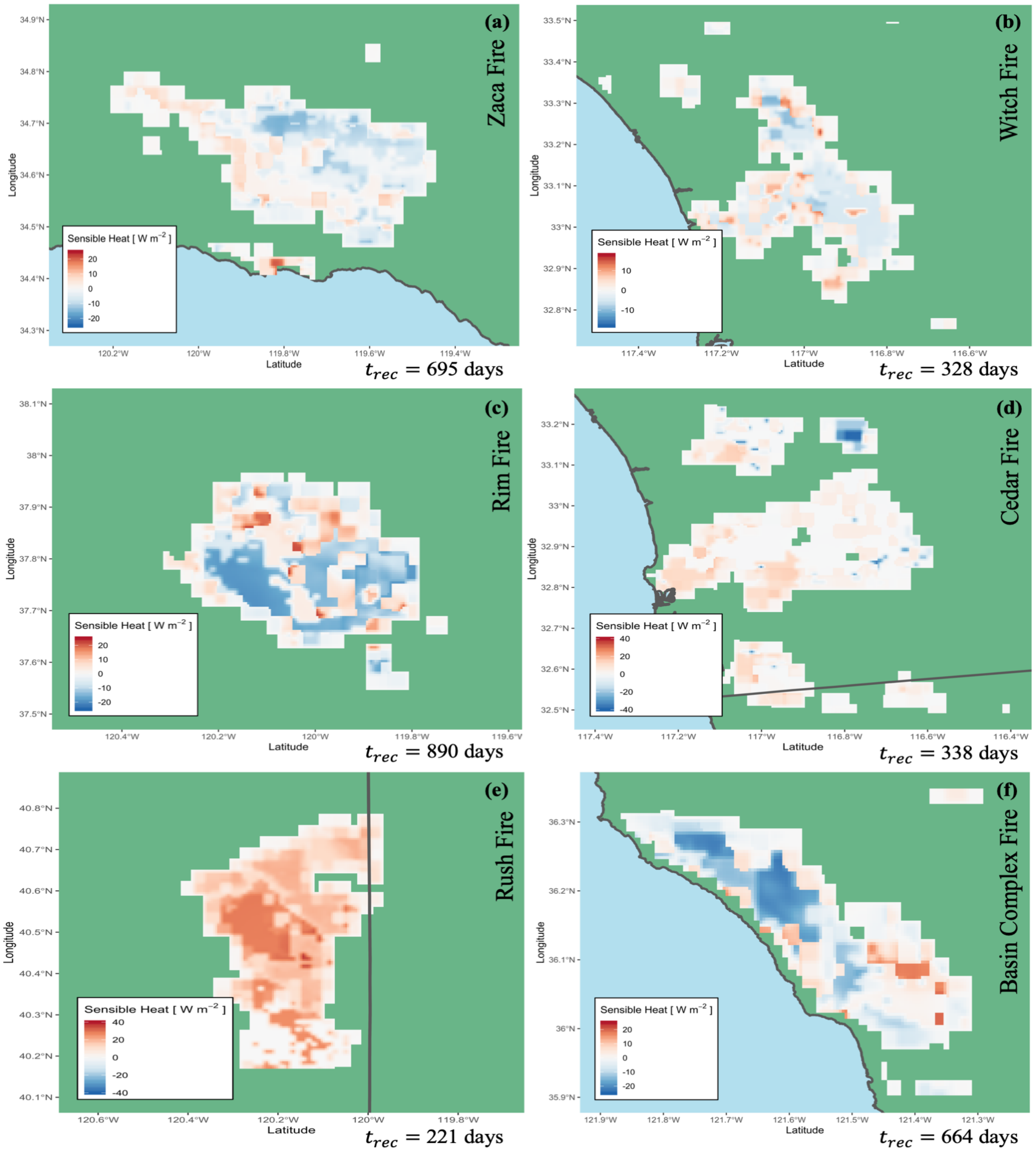

Figure 10. Same as Figure 8 except for sensible heat flux.

The Rush fire and the Cedar fire are the only cases that did not experience an average decrease in sensible heat, in fact, they average an increase of 12.7 and 1.5 W m^{-2}, respectively. Furthermore, the Rush fire was the only burn scar that experienced increases in sensible heat flux across the entire burned area with no decreases (Figure 10e). The Cedar fire case study displayed similar spatial patterns, however, there was a large patch of sensible heat decrease in the northern part of the domain (consequence of the Mataguay fire, July 2004, which burned approximately 35 km^2 and was predominately needle-leaf evergreen tree vegetation type), where the large minimum difference of -39.3 W m^{-2} occurred (Figure 10d). The Zaca fire experienced average decreases in the eastern and northern portions of the burned area and increases in the western and southern portions (Figure 10a). The Zaca fire's single largest point of sensible heat increase relative to the unburned simulation is along the coastline in the southern portion of the domain. Changes in sensible heat flux within the Rim fire perimeter display a similar spatial distribution as latent heat flux (Figure 10c). In fact, the Rim fire shows decreases in sensible heat in the same areas where latent heat flux decreased and increases in sensible heat where there was no substantial change in latent heat flux. There are several points within the Rim fire perimeter where sensible heat increased significantly, with the maximum change of 22.4 W m^{-2}. Similarly, the Basin Complex fire displays several points of large sensible heat increase, with a maximum change of 16.2 W m^{-2} (Figure 10f). Overall, there was wide variability in the impact of burned area on sensible heat flux, with the largest increase relative to the unburned scenario after the Rim fire (36.8 W m^{-2}), while the largest decrease occurred in the Cedar fire case study (-39.3 W m^{-2}).

According to monthly averaged time series, the Rush fire (Figure 11e) was the one case study to average an increase relative to the unburned scenario (12.7 W m^{-2}).

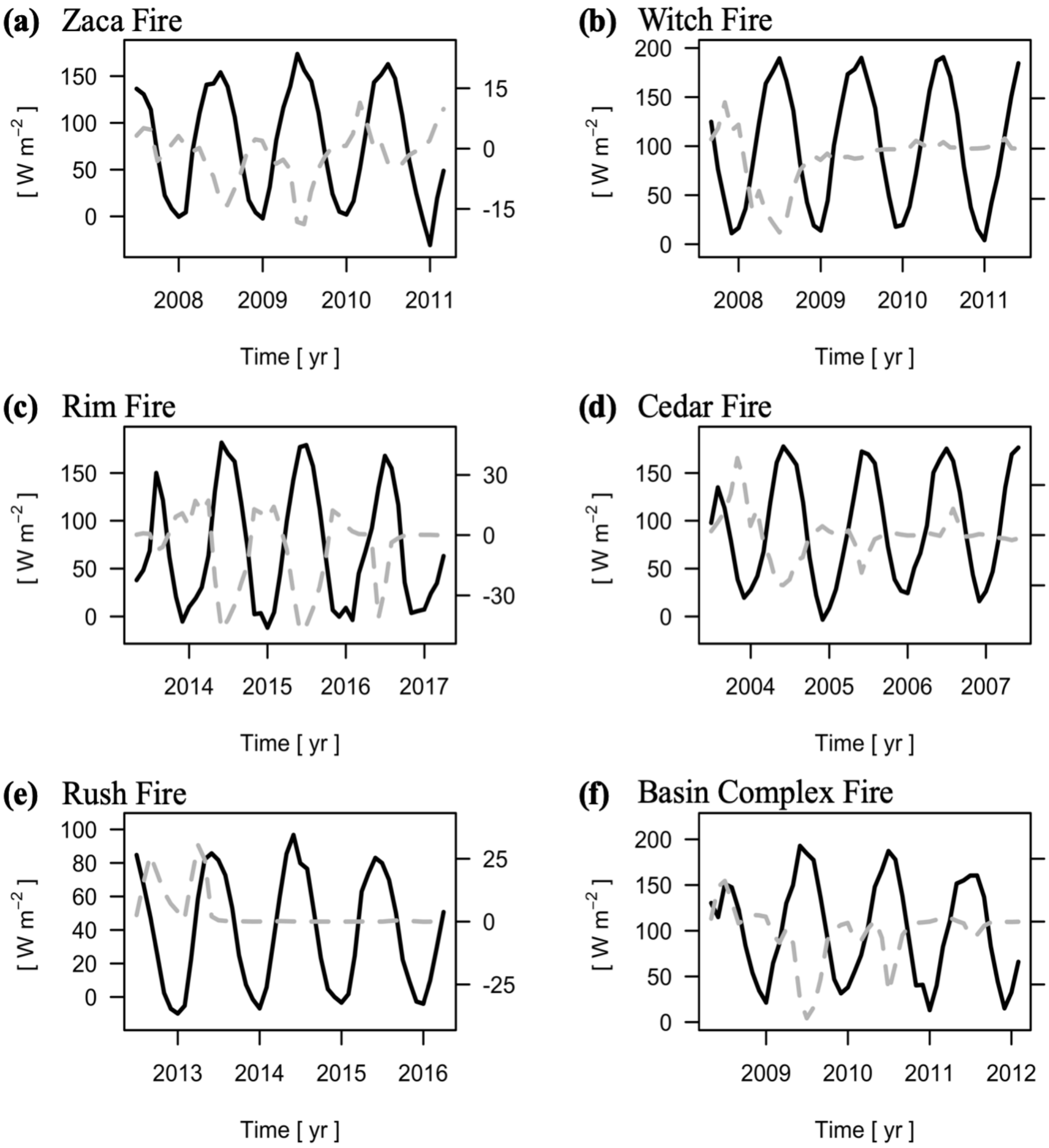

Figure 11. Same as Figure 9 except for sensible heat flux.

This increase is evident during the first year of the simulation, peaking in the spring of 2013, before returning to the unburned values with no further change (Figure 11e). The remaining fires all experienced a mean decrease in sensible heat flux. While the increase in heat flux at the beginning of the Rush fire simulation is the largest, the other fires display an initial increase in sensible heat flux as well, though, the differences were small. Additionally, the Cedar fire shows the smallest range of variability, fluctuating between -5.0 and 7.7 W m^{-}

^{2}, while the Rim fire had the largest, -47.8 to 17.3 W m^{-2}. Also, similar to latent heat flux, the most notable changes occur during the period of vegetation recovery immediately post-fire.

Net radiation was calculated by adding latent, sensible, and ground heat flux. Spatial differences between burned and unburned simulations vary heterogeneously, with increases and decreases occurring in the same fire perimeter, although the distribution of change appears to be more uniform, as the partitioning of energy into sensible and latent heat flux is more balanced (Figure 12).

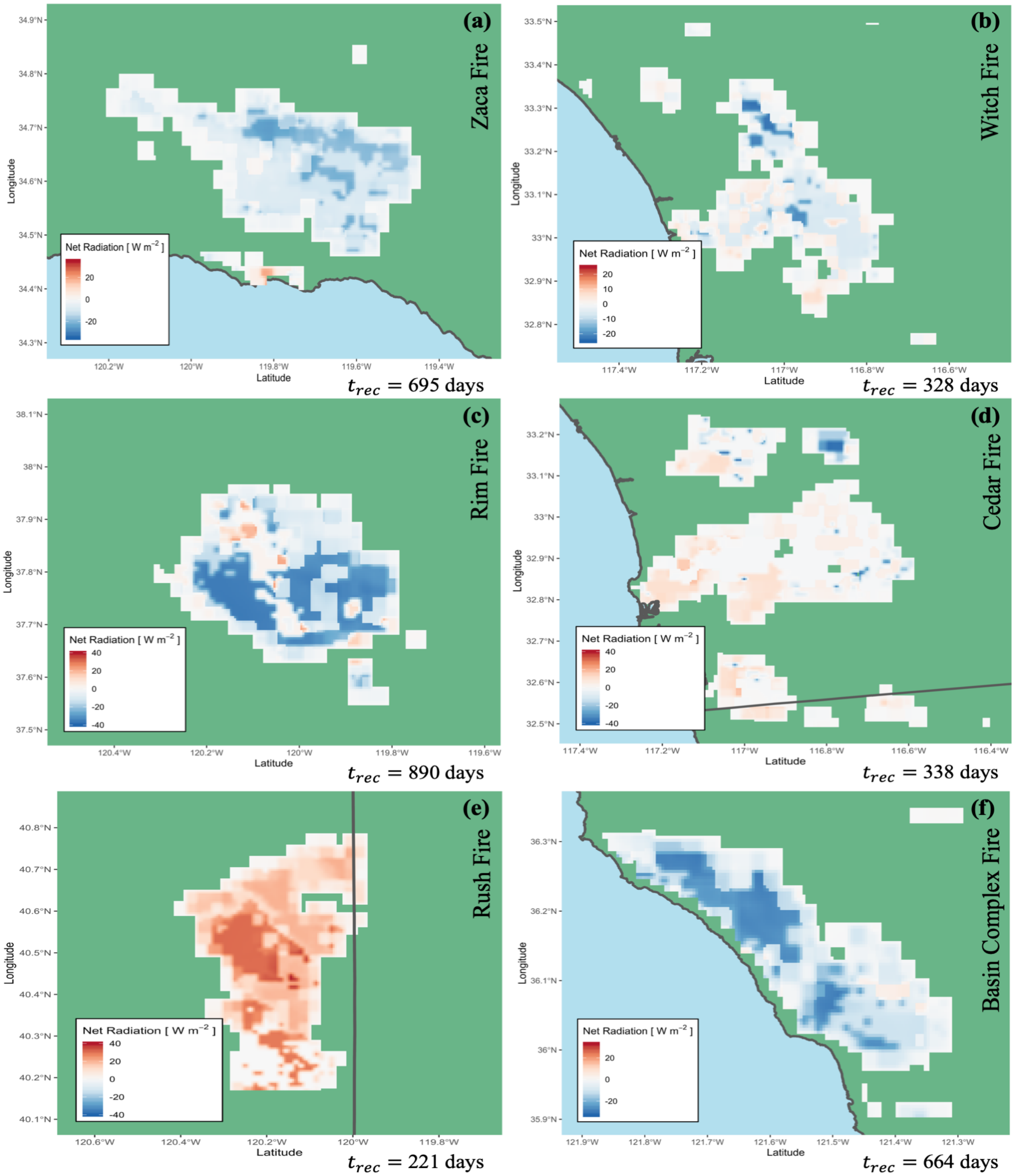

Figure 12. Same as Figure 10 except for net radiation.

Variability from the control scenario was large in all the case studies, however, the largest differences were found in the Cedar and Rim case studies, whose minimum and maximum differences were -41.0 and -35.8 W m^{-2}, and 22.0 and 39.3 W m^{-2}, respectively (Table 4). Changes in net radiation in the Zaca case study appears to have equal contributions from decreases in latent and sensible heat flux in the northern portion of the burned area, but there is a balance in the southern portion of the domain where overall change was small (Figure 12a). The concentrated areas of decreased net radiation in the Witch case study are predominantly a result of decreased latent heat, and the areas where net radiation increased were caused by increases in sensible heat flux (Figure 12b). In the Rim case study, latent and sensible heat decreased in the same areas and contributed to large regions where net radiation changed significantly (Figure 12c). Since the Cedar fire did not display any substantial change in latent heat flux, changes in net radiation are clearly dominated by the partitioning of sensible over latent heat flux (Figure 12d). The Rush fire case study is similar to the Cedar study, as increases in sensible heat flux clearly contribute the most to changes in energy balance (Figure 12e). In fact, net radiation increased relative to the unburned simulation by as much as 39.3 W m^{-2}. Furthermore, spatially averaged decreases in sensible heat flux are apparent in the northern portion of the Basin Complex fire, while decreases in both latent and sensible heat flux compound in the southern portion of the domain (Figure 12f).

Time series displaying the difference between burned and control simulations indicate that the Rush fire was the one case study that averages an increase in net radiation (13.2 W m^{-2}), a result of partitioning of sensible over latent heat flux (Figure 13e).

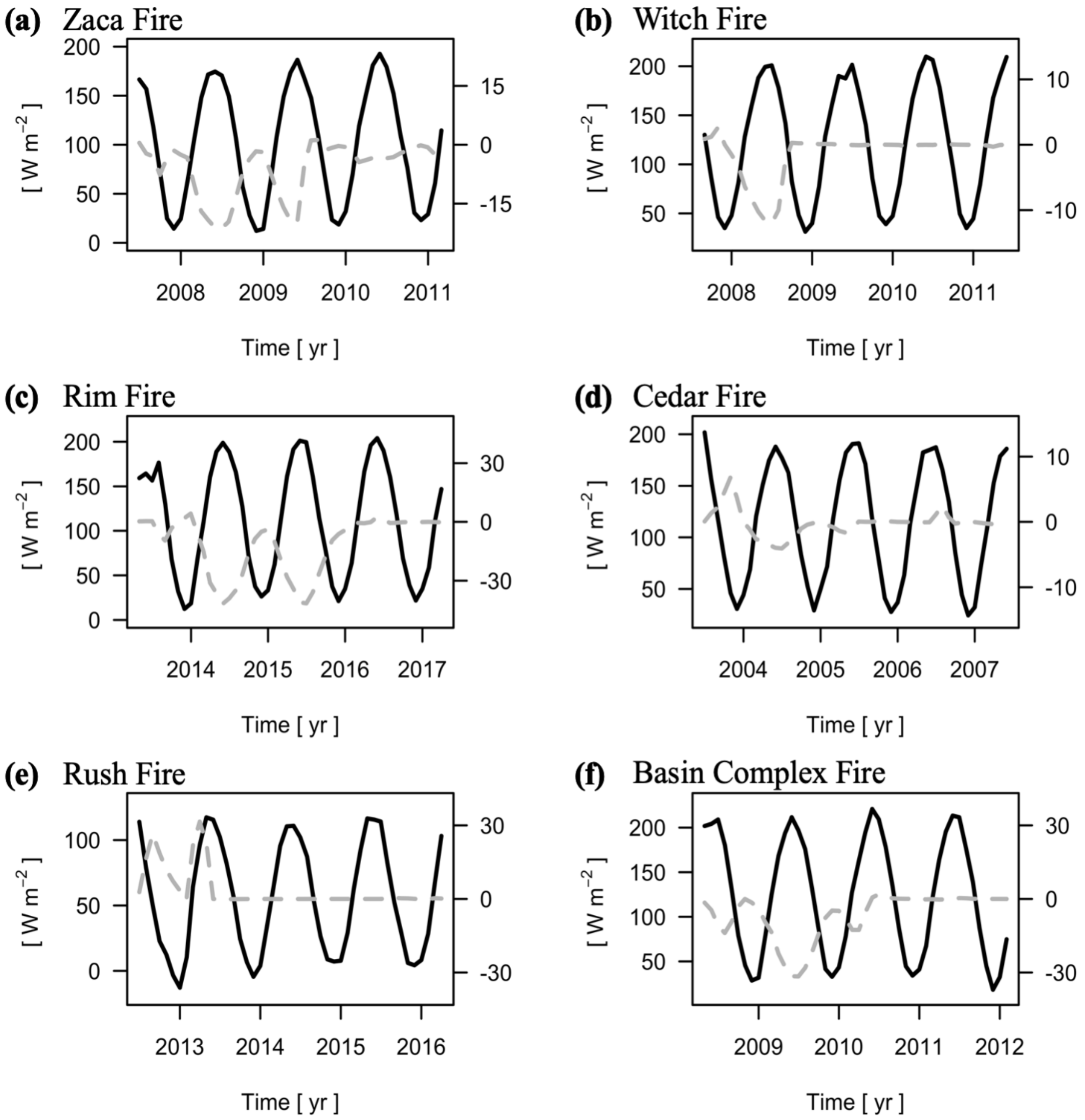

Figure 13. Same as Figure 9 except for net radiation.

Among the other fires, the greatest maximum difference in net radiation was from the Cedar fire (6.8 W m^{-2}), while the greatest minimum difference was the Rim fire (-41.7 W m^{-2}). Temporally averaged latent heat flux contributes a greater amount to the changes in net radiation than sensible heat flux for the Zaca, Rim, Cedar, and Basin Complex fires.

An analysis of the difference in simulated burned and unburned *LAI* indicates that there is a relationship between sensible heat flux and vegetation cover. The largest spatially averaged mean decreases in sensible heat are associated with the largest mean decreases in *LAI* (i.e., Rim, Basin Complex, Zaca). Here we refer to changes in *LAI* as the average amount of fire-related vegetation degradation that occurs within the vegetation recovery period in each case study. However, this relationship is not apparent in the case studies that average an increase in sensible heat (Cedar, Rush), as different vegetation, albedo, and energy balance dynamics are at play. For context, the Rush fire had the lowest mean *LAI* change (-0.2), indicating that this region had the smallest variability in *LAI* values between the burned and unburned simulations, and that the average unburned *LAI* is low (Table 4). On the other hand, the Rim fire had the largest mean change in *LAI* (-3.5), indicating that there was significant variability in the amount of vegetation simulated in the burned and unburned simulations. Spatial analysis of *LAI* distribution in each of the domains shows that the greatest decreases in sensible heat flux occur in the same areas as the greatest fire-related vegetation loss, while increases in sensible heat are associated with smaller differences between burned and unburned vegetation cover (i.e., Rush fire). For example, the Cedar case study's relatively large mean change in *LAI* (-0.6), as well as the large minimum difference in spatially averaged sensible heat flux (-39.3 W m^{-2}, are explained by this phenomenon, as these impacts are primarily a result of the burning of large amounts of vegetation in the north-eastern section of the domain (Figure 10d).

2.5 Discussion

The partitioning of energy into sensible and latent heat flux is largely dependent on moisture availability and the presence of vegetation (Chambers and Chapin 2003). In California, where individual fires are capable of burning for tens of thousands of kilometers, the associated rapid removal of vegetation has the immediate effect of reducing evapotranspiration and increasing sensible heat flux. In addition, the initial decrease in albedo due to ash deposition can increase the amount of energy available at the surface (Chambers and Chapin 2003). Here we show that it is possible to model the impact of wildfire burned area on surface climate, that the impact on radiation balance is climatologically significant, and that the disturbance can be quantified and used to inform future modelling endeavors.

One of the most remarkable aspects of our results is the variability found in the spatial distribution of heat flux within the case study domains. For example, within a single burned-area perimeter we find that there is significant variability in net radiation changes, particularly the sensible heat component (Figure 10). Average increases and decreases of sensible heat flux within close proximity likely result from differences in vegetation cover. Initially, as more heavily vegetated regions (with high *LAI* and lower relative albedo values) transition to char and subsequently bare ground, the reduction in evapotranspiration will dominant over the increase in sensible heat flux caused by the effects of ash deposition as in the Rim, Basin Complex, and Zaca fires (Table 4). However, over time, high *LAI* regions transitioning to bare ground might experience substantial decreases in sensible heat flux as the land surface coupling with the atmosphere is greatly diminished (Figure 11). Meanwhile, the conversion of vegetation types such as shrubland and groundcover to char and then bare ground can cause the increases in sensible heating to dominate, because the effect of ash deposition outweighs changes in canopy coupling to the atmosphere, as observed in the Rush and Cedar fires (Figures 10d, e). This behavior has been described in works by Chambers et al. (2005). So, varying with albedo recovery period, regions within each burn perimeter with higher *LAI* are more likely to experience spatially averaged decreases in sensible heat flux, whereas more sparsely vegetated areas show an increase. We see this phenomenon in the Rim fire, where a distinct outline of relatively sparse vegetation exhibits sensible heat increase, while the surrounding forested region shows a decrease (Figure 10c).

Immediately post-fire, the lowering of the albedo of the land surface, caused by char and ash deposition, is associated with greater radiation absorption at the surface and an increase in sensible heating. The degree of change in albedo varies based on pre-fire vegetation characteristics, soil reflectance, burn severity, and vegetation recovery (Jin and Roy 2005). Initial increases in sensible heat flux due to char and ash deposition are often balanced by a reduction in latent heat flux due to the removal of vegetation, however, the impact of ash deposition on sensible heat partitioning dominates where fire-related impacts on vegetation are low, as observed in the Witch, Cedar, and Rush fires (Figures 13b, d, e). Thus, increases in net radiation (primarily partitioned into sensible heat flux) at the beginning of simulations for fires in sparsely vegetated areas are likely caused by the deposition of ash on the surface immediately following the large fire (Figures 11 and 13).

While ash deposition affects the partitioning of energy for a short period after a fire, the removal of vegetation displays its own unique signature. Initially, large reductions in biomass cause more energy to be partitioned into ground heat fluxes at the expense of latent heat, warming the surface (Figures 11). These results are corroborated by other studies that found that average net radiation increases more in non-forested landscapes compared to forest, as canopy properties (i.e., surface roughness) were impacted more strongly in forested landscapes, leading to a greater decrease in atmosphere-surface coupling (Anthes 1984; Andre et al. 1989; Chambers and Chapin 2003; Beringer et al. 2005; Chambers et al. 2005). In other words, where low-lying vegetation is common and there is little to no canopy, the increase in net radiation as a result of ash deposition and a lowered surface albedo dominates over the decrease in latent heat flux (Rush, Cedar). We see this effect most strongly in the Witch, Rush, and Cedar fires, where a large proportion of the burned land surface has a low average *LAI*, and there is weaker surface-atmosphere coupling. In addition, vegetation recovery time varies broadly among the six chosen wildfires, and the fires with the shortest recovery time (Rush, Cedar), and the largest ratio of ash deposition to vegetation recovery, appear to generate more net radiation while the longer recovery times experience decreases (Rim, Basin Complex). This supports the notion that vegetation recovery and ash deposition periods of similar length can increase net radiation at the surface due to the overpowering effect of ash deposition over vegetation removal, especially where vegetation is sparse (Rush).

2.6 Conclusion

This study investigated the impacts of wildfire burned area on surface radiation budget and energy exchange, as well as the importance of vegetation recovery on land surface processes. A selection of six historic California wildfires were chosen and a burned and unburned simulation was performed for each. A 10-km control simulation for the state of California indicated that the model is capable of accurately reproducing temperature and net radiation in the study areas, and its results may be used as a benchmark against which the burned simulations can be compared. In the burned simulations, the albedo of the land surface is lowered to imitate the effect of ash deposition on the land surface and vegetation is removed for a period of time unique to each domain's common vegetation index. This methodology highlights the role of post-fire vegetation recovery on the partitioning of energy into sensible and latent heat flux.

Spatially and temporally averaged latent heat flux decreased in all the case studies except the Rush fire. The greatest changes occurred in the Rim, Basin Complex, and Zaca fires, with spatially averaged decreases of 8.9, 7.6, and 5.8 W m^{-2}, respectively. Spatially averaged decreases in latent heat flux comprised a greater proportion of the total change in net radiation for the Zaca, Witch, Rim, and Basin Complex fires, while the Cedar and Rush fires experienced a greater partitioning of energy into sensible heat. Every case study recorded a decrease in temporally averaged sensible heat flux except the Rush fire, which recorded a mean increase of 12.7 W m^{-2}, accounting for the majority of its total change in net radiation (13.2 W m^{-2}). We hypothesize that this increase in net radiation after the Rush fire is a result of small changes in mean *LAI* as well as an extended ash deposition period that leads to the dominance of sensible heating. Initial increases in sensible heating due to the effect of ash deposition were recorded after every fire, however, this change was balanced by decreases in latent heat flux (i.e., the removal of vegetation) in the Zaca, Rim, and Basin Complex burned areas. Finally, the greatest changes in temporally averaged net radiation occurred in the Rim (-41.7 W m^{-2}), Basin Complex (-31.6 W m^{-2}), and Rush (26.5 W m^{-2}) fires.

Results also indicate a clear relationship between fire-related degradations in *LAI* and heat flux. For example, wildfires that occur in areas of low-lying vegetation are associated with increases in sensible heat flux (an effect that is magnified by long albedo recovery times) (Rush), while the burning of heavily vegetated regions are associated with the largest decreases in sensible and latent heat flux (Rim, Basin Complex). This phenomenon is especially apparent in the Cedar fire case study, where a large amount of vegetation was burned in a single portion of the domain, leading to substantial decreases in sensible heat flux, and disproportionately influencing the spatially averaged minimum difference. Future work with the SSiB modelling tool can inform how wildfire and subsequent vegetation recovery alters critical biophysical processes across a spectrum of burn severities.

With this study the immediate impacts of wildfires on local meteorology become more apparent. Around the world, larger and larger burned areas will reduce the cooling effects of evapotranspiration, while simultaneously warming the land surface via sensible heat. These changes to the properties of the land surface have a strong influence on post-fire vegetation succession and planetary boundary layer development, making ecosystems more vulnerable to the impacts of wildfire and climate change (Syphard et al. 2006).

Chapter 3. Impacts of Burn Severity on Short-Term Postfire Vegetation Recovery, Surface Albedo, and Land Surface Temperature in California Ecoregions

3.1 Introduction

The annual burned area in California has grown since 2000, with dramatic increases in 2017, 2018, and 2020 (Williams et al. 2019). The surge in wildfire activity in recent years is often cited as being a result of moisture deficits exacerbated by seasonal summer drought, reduced snowpack, early spring snowmelt, increased aridity, and accelerated vegetation die-off (Westerling et al. 2006; Westerling et al. 2008; Spracklen et al. 2009; Williams et al. 2019). These wildfire risk factors are projected to worsen under Intergovernmental Panel on Climate Change (IPCC) warming scenarios and contribute to the growing amount of total annual burned area (Westerling et al. 2008; Westerling et al. 2011; Barbero et al. 2015; Williams et al. 2019). In California, the impacts of anthropogenic climate change on wildfire activity and wildfire related land cover change will likely vary seasonally and spatially due to the diversity of climate, topography, and vegetation distributions (Williams et al. 2019). Also, climate change is likely to have further impacts on biophysical response by influencing the moisture conditions that can determine the rate of vegetation recovery, the species, structure, and flammability of the succeeding flora, as well as the frequency of future wildfire occurrence (Westerling et al. 2011; Bright et al. 2019).

Wildfire related land cover change on the scale of California's large burned areas alters boundary layer climate and has a significant impact on surface energy balance through changes to net radiation (Rother and De Sales 2020). The immediate effect of wildfire on the land surface is the deposition of a layer of charcoal, or ash, which decreases albedo and increases sensible heat flux (Veraverbeke et al. 2012; Dintwe et al. 2017; Rother and De Sales 2020). The postfire change in albedo is highly dependent on the severity of the fire and is generally short-lived, as the ash is soon dispersed by wind and rain (Veraverbeke et al. 2012; Dintwe et al. 2017). At the same time, the removal of vegetation is more often associated with a decrease in latent heat flux and an increase in sensible heating, as decreased evaporative cooling can lead to increases in land surface temperature. Land surface temperatures can rise by up to 8 °C after wildfire events, with the duration of the change varying based on vegetation and ecosystem type (Bremer et al. 1999; Amiro et al. 2006; Wendt et al. 2007). Furthermore, the duration and magnitude of many of these wildfire-induced biophysical impacts are highly dependent on burn severity (Veraverbeke et al. 2012).

Burn severity refers to wildfire-induced modifications to the soil surface and vegetation conditions, and is controlled by a suite of factors including terrain slope, pre-disturbance vegetation composition, weather and climate conditions, and fuel characteristics (Key and Benson 2005; Lutes et al. 2006; Gitas et al. 2009; Keeley 2009; Bright et al. 2019). High severity fires are defined by complete canopy mortality and the burning of the entire top layer of soil, while low severity fires tend to burn for a shorter period of time and result in the loss of ground and understory vegetation (Keeley 2009; Bright et al. 2019). Significant alterations to the land surface associated with high severity burns change the spectral reflectance of vegetation and underlying soil, making remote sensed datasets ideal for studying their patterns. A number of studies have used satellite-derived datasets to study the effects of land surface disturbances on the recovery of vegetation in Mediterranean ecosystems (Hope et al. 2007; Meng et al. 2014; Petropoulos et al. 2014; Fernandez-Manso 2016). In addition, the burn severity associated with any particular wildfire may have important implications for vegetation recovery (Meng et al. 2015; Bright et al. 2019). Furthermore, an ecoregion-level understanding of the biophysical response to wildfire will help land managers identify ecosystems and wildland-urban interfaces particularly at risk for the consequences of high severity fires and weakened vegetative resilience (Meng et al. 2015).

Here we investigate the impact of burn severity on vegetation recovery, albedo change, and land surface temperature in California between 2003 and 2020. In addition, we analyze the amount or magnitude and distribution of burned area, EVI, surface albedo, and land surface temperature within California ecoregions, as well as the correlations between burn severity, EVI, and land surface temperature. Our metric for burn severity, a MODIS-derived relative differenced Normalized Burn Ratio (RdNBR) dataset, was used to stratify the early-summer postfire averages for three biophysical variables into three burn severity classes. Our primary research objective was to quantify the impact of burn severity on vegetation recovery, albedo, and land surface temperature across the state in the first five years after fire. Through the ecoregion-specific calculation of burned severity thresholds and their use in the analysis of EVI, land surface albedo, and temperature, we hope to help land managers foresee consequences of, and determine areas at risk for, high severity fire. In addition, five-year postfire trajectories of EVI, albedo, and temperature will improve the reliability of land surface models when simulating the impacts of wildfire on the land surface.

3.2 Materials and Methods

Postfire EVI recovery, albedo change, and land surface temperature (LST), as well as all burn severity metrics, including relative differenced Normalized Burn Ratio (RdNBR), were analyzed using Moderate Resolution Imaging Spectroradiometer (MODIS) satellite data. We are aware that the coarse spatial resolution of MODIS imagery requires some sacrifice to spatial heterogeneity. However, the high temporal frequency and wide-area coverage of the MODIS data allow for a focus on the temporal patterns of vegetation recovery, albedo, and land surface temperature change.

3.2.1 California Ecoregions and Land Cover Types

The study area is California, where the U.S. Environmental Protection Agency has defined seven ecoregions used here for analysis: Southern California Mountains (SCM), Southern California Coast (SCC), Central California Foothills (CCF), Klamath (K), Cascades (C), Eastern Cascades (EC), and Sierra Nevada (SN) (Griffith et al. 2016) (Figure 14). It is important to note that three ecoregions within California were excluded from the analysis. The Marine West Coast Mountains region was removed from the analysis because it experienced significantly fewer fires than the other ecoregions (~2500 total burned pixels; 3% burned area). Also, the North American Desert (i.e. southeast and northeast California) rarely experiences wildfire (~15000 total burned pixels, 2% burned area). In fact, only one large wildfire occurred in this region between 2003-2020 (i.e. the Rush Fire, Lassen County, August 2012) and so does not provide a comprehensive view of the entire ecoregion over the duration of the study period, as the study of a single fire is outside the scope of this project. Following this, the California Central Valley, a major agricultural hub in the United States, is removed from analysis due to the predominance of crop land cover types and irrigated agriculture that does not experience vegetation recovery in a comparable way to other land cover types. Additionally, the Central Valley experiences a high frequency of small fires of low severity that are filtered out after the application of burn severity thresholds.

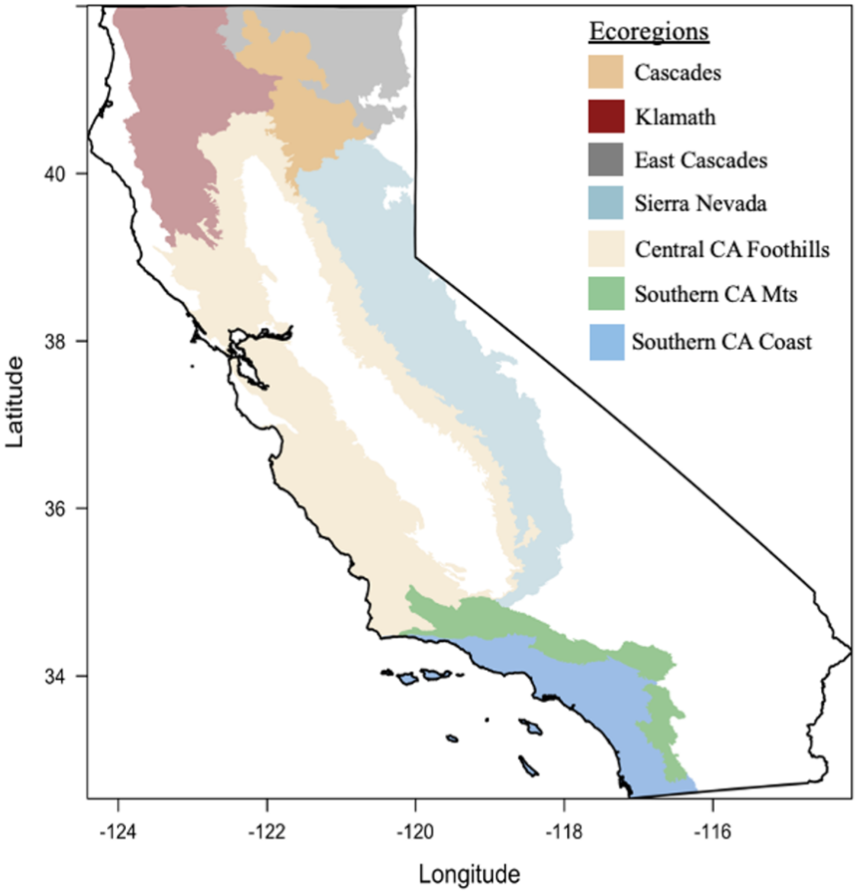

Figure 14. Ecoregions of California, including Southern California Mountains (SCM), Southern California Coast (SCC), Central California Foothills (CFF), Klamath (K), Cascades (C), East Cascades (EC), and Sierra Nevada (SN). Areas in white represent coastal zones, Central Valley agriculture and desert areas. The coastal zone in northwest California and the desert zone in the south and northeast are removed from analysis due to rare occurrence of wildfire. The Central Valley was removed from the analysis due to the predominance of crop land cover, irrigated agriculture, and the high frequency of low severity fires that are filtered out after the application of burn severity thresholds. Ecoregions of California (Griffith, 2016): https://doi.org/10.3133/ofr20161021.

We used the MODIS Version 6 MCD12Q1 500-m Land Cover Type to analyze the pre- and postfire characteristics of the land surface (Friedl et al. 2002; Friedl et al. 2010). This product is derived from supervised classifications of reflectance data and provides 17 global land cover types, including needleleaf forest, broadleaf forest, closed shrublands, woody savanna, grasslands, and others (Friedl and Sulla-Menashe 2019). We calculated the percentage of each vegetation type that remained unburned for the duration of the study period, as well as the mean early-summer EVI for five predominant land cover types (Table 5).

Table 5. Land Cover characteristics for the unburned regions of each ecoregion averaged for 2003 - 2020.

	Southern California Mountains	Southern California Coast	Central California Foothills	Klamath Mountains	Cascades	Eastern Cascades	Sierra Nevada
Total Land (total 500 m pixels)	89263	117026	446343	201138	84997	107530	305702
Burned Area (%)[a]	46	25	16	31	6	7	17
Nonburned Areas (number of 500 m pixels)	47861	88028	376989	138994	79548	99845	253509
Percentage of Land Cover Types (%)							
Needleleaf	3	0	3	63	37	2	21
Closed Shrublands[b]	14	8	13	23	46	6	21
Open Shrublands	20	4	3	0	0	0	5
Savanna	28	12	17	3	9	8	21
Grasslands	33	23	51	6	6	78	27
Mean Early-Summer EVI[c]							
Needleleaf	0.36	0.32	0.42	0.42	0.36	0.32	0.39
Closed Shrublands	0.24	0.22	0.3	0.34	0.29	0.24	0.33
Open Shrublands	0.18	0.16	0.18	0.28	0.17	0.14	0.15
Savanna	0.24	0.27	0.27	0.31	0.3	0.26	0.27
Grasslands	0.23	0.18	0.19	0.29	0.23	0.19	0.23

Overall, the prevailing land cover type within the unburned areas of the Klamath ecoregion is needleleaf forest (63%); the Eastern Cascades ecoregion is mostly grassland (78%); the Cascades are most substantially needleleaf forest (37%) and closed shrublands (46%); the Central California Foothills ecoregion is mostly grasslands (51%) (Table 5). For our purposes of land cover analysis, the closed shrubland category includes both closed shrublands and woody savanna vegetation types.

3.2.2 Fire History

The location and approximate date-of-burn information for California wildfires that occurred between January 2003 and December 2020 was obtained from the MODIS MCD64A1 product (Giglio et al. 2015). Additionally, this burned area product was also used to calculate the total annual burned area within the seven ecoregions of California for the years 2003-2020. MODIS identifies burned areas by measuring changes in surface reflectance (Roy et al. 2002). The majority of land surface areas that burn each year are a consequence of large wildfire events, and MODIS pixels classified as burned more than once within the study period were not included in the calculation of total burn pixels.

3.2.3 MODIS Enhanced Vegetation Index and Albedo

To analyze the presence of vegetation on the land surface, we used the MOD13Q1 Version 6 Enhanced Vegetation Index (EVI) 16-day, 250-m resolution product. MOD13Q1 can discriminate between canopy and canopy background and has an improved atmospheric correction for cloud and aerosol contamination (Jin et al. 2012; Didan 2015). Here we use EVI as a measure of vegetation productivity and refer to vegetation recovery synonymously with EVI recovery to describe the trajectory of postfire EVI towards prefire values. Mean early-summer EVI was calculated for individual vegetation types within each ecoregion (Table 5). Mean EVI was highest for all vegetation types within the Klamath region. Overall, the SCM and the EC had the lowest average mean early-summer EVI. In addition, needleleaf forest had a higher mean early-summer EVI within each ecoregion than any other vegetation type.

For the analysis of land surface albedo, we used the 500-m resolution MCD43A3 Version 6 White-Sky shortwave albedo model product at a 3-day temporal resolution (Schaaf and Wang 2015). MODIS shortwave albedo ($0.3 – 5.0\ \mu$m) has been successfully used to measure albedo response to wildfire in previous studies (Lyons et al. 2008; Samain et al. 2008; Jin et al. 2012; Gatebe et al. 2014; Huang et al. 2015; Dintwe et al. 2017).

3.2.4 MODIS Land Surface Temperature

Collection 6 MODIS MYD21A2 Land Surface Temperature (LST) data were used for this study to calculate five-year postfire recovery patterns within pixels of varying levels of burn severity. MYD21 is an 8-day 1-km product that is derived through a Temperature/Emissivity Separation technique using thermal infrared bands 29 (8.4 - 8.7 μm), 31 (10.78 - 11.28 μm), and 32 (11.7 – 12.27 μm), as well as land surface temperature (Hulley 2017). In addition, a Water Vapor Scaling correction is applied to account for biases during warm and humid weather. MYD21 has been evaluated against ground-based measurements and is shown to have a bias of -0.2 °C (Jin and Liang 2006; Wang et al. 2007; Wang and Liang 2009; Ma et al. 2019).

3.2.5 Burn Severity

We calculated Normalized Burn Ratio (NBR, eq. 1) using MOD13Q1 surface reflectance band 2 (841-876 nm) and band 7 (2105-2155 nm). NBR is a spectral index that has been widely used to analyze the post-disturbance effect of wildfire on the land surface (French et al. 2008; Soverel et al. 2010; Veraverbeke et al. 2010; Jin et al. 2012; Parks et al. 2014; Hislop et al. 2018; Shvetsov et al. 2019), and studies evaluating NBR against on-the-ground estimates of burn severity have found strong correlations (Van Wagentendonk et al. 2004; Key 2006; Hudak et al. 2007; Keeley 2009; Bright et al. 2019). NBR uses differences in reflectance between the near infrared and shortwave infrared wavelengths, normalized by the sum of the two bands, to measure changes to the land surface after wildfire events, such as deposition of char and ash, removal of vegetation, decreased moisture content, and exposed soil (Vlassova et al. 2014; Bright et al. 2019; Shvetsov et al. 2019). We calculated an early-summer NBR (June 26 - August 12) for California for each year within the time period January 2002 through December 2020.

$$NBR = \frac{((Band\ 2)-(Band\ 7))}{((Band\ 2)+(Band\ 7))} \tag{3}$$

Healthy vegetation displays strong reflectance in the near infrared band (band 2) and low reflectance in the shortwave (band 7), while recently burned areas show the opposite (Keeley 2009). Therefore, low NBR values indicate recently burned areas (or low vegetation), while high NBR values indicate healthy vegetation. Prefire NBR was calculated as the average NBR within burned area perimeters in the year before the fire, while postfire NBR was calculated by measuring average NBR in the same burn perimeter the year after the fire.

We also calculated the differenced Normalized Burn Ratio (dNBR) by subtracting average postfire NBR from average prefire NBR (dNBR=prefireNBR - postfireNBR). dNBR time series were generated for the early-summer period for each year from January 2002 - December 2021. While dNBR utilizes pre- and postfire imagery to calculate an absolute change, the relative differenced Normalized Burn Ratio (RdNBR) measures burn severity relative to prefire surface reflectance (Miller and Thode 2007), and is calculated as:

$$RdNBR = \frac{dNBR}{\sqrt{|prefireNBR|}} \tag{4}$$

RdNBR assesses changes in near infrared and shortwave infrared radiation in the context of post-disturbance variations in vegetation and soil moisture (Jin et al. 2012). RdNBR has been shown to be more robust when comparing fires across landscapes, and more accurately differentiates levels of burn severity within heterogeneous landscapes (Miller and Thode 2007; 2010). Values typically range from –1.5 to +1.5, with positive numbers indicating varying degrees of burn severity (when postfire NBR is negative), while negative values indicate varying levels of vegetation recovery (when postfire NBR is positive). Burn severity thresholds for low, moderate, and high severity were derived for each ecoregion from the cumulative distribution of RdNBR for 20%-45%, 45%-75%, and >75% percentiles. These percentile groups span a different range of RdNBR values for each ecoregion, and thus are more dynamically suited to regions with varying prefire surface reflectance, which allows for a more standardized and informed classification of burn severity across landscapes compared to a single set of thresholds applied to all ecoregions. It is important to note that burned pixels with RdNBR values below the 25th percentile were considered recovered, or unchanged, and are not included in this study, as the surface reflectance values in the postfire image returned to roughly that of the prefire image after one year.

Statistical testing involved calculating the correlation coefficient for pre- and postfire NBR with RdNBR, as well as ΔEVI and ΔLST with RdNBR (change refers to the difference between the pre- and first year postfire images unless otherwise specified). Pearson correlation values were found using cortest() function in the *R* programming software. In order to obtain the correlations for each ecoregion, the pre- and postfire early-summer average of NBR, RdNBR, EVI, and LST was calculated within each year's burned area. The temporal correlation, using one average for each variable for 2002-2021 was then obtained for the pairs listed above. This correlational analysis provided a useful metric with which to analyze the dominant controlling factor in the calculation of RdNBR (pre- or postfire NBR). It was also a useful tool for understanding the relationship between postfire biophysical response and burn severity. In addition, by comparing the biophysical changes that occur between the first-year pre-fire and the first-year post-fire (i.e. differenced indices), we could quantify the largest changes between a burned and unburned land surface.

3.2.6 Fire-Year Postfire Averages

We focused on the temporal dimension of burn severity's impact on biophysical variables by analyzing the early-summer averages for EVI, shortwave albedo, and land surface temperature within seven ecoregions and three burn severity classifications during the first five years after fire. Burned areas were considered for the years 2003-2020, which allowed for the inclusion of one year pre-fire (2002) and one year post-fire (2021) at the beginning and end of the time series (i.e. five years of postfire data were not required for a given year of burned area data to be included in the analysis). Early-summer averages were obtained for each biophysical variable by calculating their mean value within annual ecoregion specific burned areas between approximately June 26 and August 12 in each year from 2002 to 2021. We chose early-summer because California's vegetation tends to peak annually during this season and this time period represents the beginning of the state's fire season. A single early-summer average from each year allows for the efficient calculation of RdNBR across multiple years, as well as a clear indication of the recovery pattern over five years post-fire. For each variable and burn severity classification we plotted postfire response for the five years following the wildfire. In addition, the pre-fire early-summer average was calculated for each variable. We understand that by calculating burn severity with surface reflectance imagery one-year post-fire, we incorporate an entire year of postfire recovery, which may vary within ecoregions. However, the high temporal frequency of the sampling in the MODIS datasets, as well as the inclusion of seven ecoregions with different predominant vegetation types and climates, provides important detail to this temporal study of biophysical response.

3.3 Results

3.3.1 Burned Area and Burn Severity Analysis

The spatial distribution of wildfires indicates that many of the large fires that occurred in the northern California ecoregions burned in the summer months of July, August, and September (Figure 15a). However, in southern California, fires burned predominantly in August, September, and October. In fact, the Thomas Fire, which burned in Santa Barbara and Ventura counties of southern California in 2017 was the only large wildfire to burn in December. Burn severity maps indicated that average RdNBR in the SCC and CCF ecoregions is predominately categorized as low severity, while the K and SCM experienced more fires of moderate and high severity (Figure 15b).

Total burned area for the entire study area during the 2003-2020 study period was 66807 km^2, which is ~20% of the study area. The average early-summer RdNBR falls within the low burn severity range for each respective ecoregion (Table 6). However, the K, C, and SN ecoregions show the highest prefire NBR values, indicating larger amounts of prefire vegetation (Table 6).

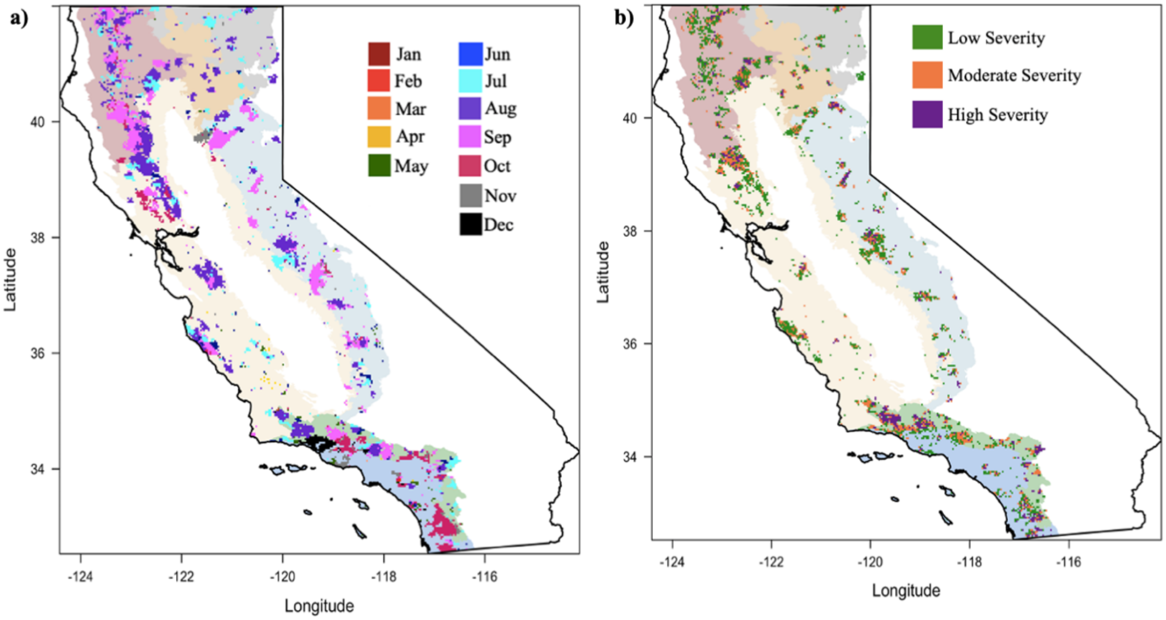

Figure 15. All burned areas by month for the time period of January 2003 - December 2020 (a) and all burned area by burn severity class for the time period of January 2003 - December 2020 (b). The seven ecoregions are larger polygons represented in low saturated colors (as in Figure 14). For panel (a), a binary burned-unburned mask was generated for each month of the MCD64A1 Monthly Burned Area product and the sum for each month calculated. For panel (b), RdNBR was derived from MOD13Q1 surface reflectance data, burn severity thresholds were applied, and the spatial distribution of burn severity plotted (see Methods).

Table 6. Burned area characteristics for each ecoregion averaged for the period 2003-2020.

	Southern California Mountains	Southern California Coast	Central California Foothills	Klamath Mountains	Cascades	Eastern Cascades	Sierra Nevada
Burned Area (square kilometers)	10351	7250	17339	15536	1362	1921	13048
Number of 500 m pixels	41402	28998	69356	62144	5449	7685	52193
Summer EVI (prefire)[a]	0.24 (±0.3)	0.19 (±0.02)	0.25 (±0.05)	0.4 (±0.05)	0.29 (±0.07)	0.27 (±0.13)	0.31 (±0.04)
Summer EVI change (first year after fire)[b]	-0.07 (±0.04)	-0.02 (±0.03)	-0.06 (±0.03)	-0.15 (±0.04)	-0.1 (±0.05)	-0.04 (±0.04)	-0.1 (±0.04)
Summer RdNBR	0.46 (±0.21)	0.29 (±0.55)	0.34 (±0.14)	0.44 (±0.11)	0.32 (±0.34)	0.24 (±0.25)	0.47 (±0.14)
Summer dNBR	0.26 (±0.12)	0.07 (±0.08)	0.17 (±0.08)	0.33 (±0.1)	0.27 (±0.16)	0.1 (±0.1)	0.3 (±0.12)
Summer NBR (prefire)	0.21 (±0.08)	0.05 (±0.06)	0.23 (±0.1)	0.58 (±0.11)	0.37 (±0.14)	0.22 (±0.19)	0.4 (±0.11)
Summer NBR (first year after fire)	-0.01 (±0.06)	-0.01 (±0.07)	0.07 (±0.07)	0.24 (±0.1)	0.14 (±0.12)	0.12 (±0.21)	0.1 (±0.07)
Summer Albedo (prefire)	0.13 (±0.02)	0.14 (±0.01)	0.15 (±0.02)	0.11 (±0.01)	0.11 (±0.01)	0.13 (±0.02)	0.11 (±0.01)
Summer Albedo (first year after fire)	0.15 (±0.02)	0.15 (±0.01)	0.15 (±0.02)	0.1 (±0.01)	0.11 (±0.02)	0.13 (±0.02)	0.11 (±0.01)
Summer LST (prefire)	314.6 (±4.07)	316.68 (±2.26)	316.68 (±3.77)	305.4 (±2.97)	308.42 (±3.09)	314.47 (±5.48)	308.24 (±2.54)
Summer LST (first year after fire)	320.33 (±2.73)	3.19 (±2.64)	320.65 (±2.97)	309.26 (±2.86)	313.11 (±4.52)	317.44 (±6.02)	313.26 (±3.24)

The CCF ecoregion recorded the most burned area (17339 km^2), while the Cascades ecoregion recorded the least (1362 km^2) (Table 6). Roughly 17600 km^2 burned in the southern California ecoregions of SCM and SCC combined, while over 30000 km^2 burned in the northern California ecoregions of K, C, EC, and SN (Table 6). Warm and dry late spring and summertime meteorological conditions drive northern California fires in the months of

June through August, while low levels of precipitation (4.7 mm mo^{-1}) and high summertime temperatures (~27 °C on average), along with Santa Ana winds, drive southern California fires in August through October (Daly et al. 1997; Keeley 2009; Jin et al. 2014).

California ecoregion specific total annual burned area was plotted for 2003-2020 (Figure 16). Total burned area, including all seven ecoregions, was high in 2008, 2017, 2018, and 2020 when 6382 km^2, 6710 km^2, 9165 km^2, and the remarkable 22764 km^2 of land area were burned, respectively.

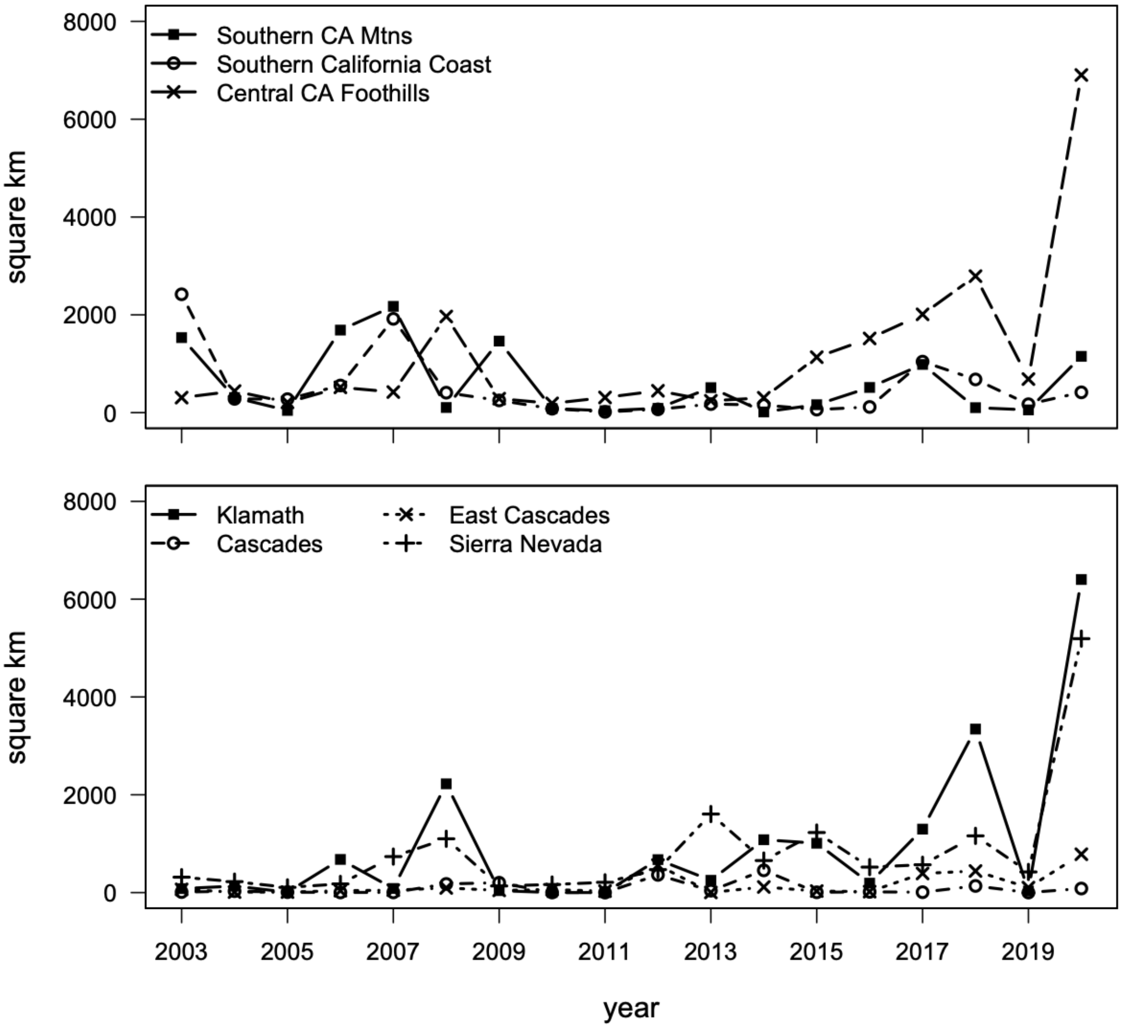

Figure 16. California ecoregion specific total annual burned area for 2003-2020 based on MODIS MCD64A1 approximate date-of-burn product. Ecoregions are split into

roughly southern (top) and northern (bottom) California. Total burned area each year represented in square kilometers.

In 2008 and 2018, the most land area burned within the Klamath ecoregion; however, in 2017, more land burned in the CCF, SCM, and SCC ecoregions compared to the northern California regions. More land burned in SCM, SCC, and CCF ecoregions than in the K, C, EC, and Sierra Nevada ecoregions in eleven of the eighteen years of the study period, however, between 2012 and 2015 more area burned in K, C, EC, and Sierra Nevada. The CCF saw a steady increase in total annual burned area between 2015 and 2018, a decrease in 2019, and a dramatic increase in 2020. In fact, 2018 and 2020 each broke the previous record for annual burned area, with 2020 totals of 6904 km^2, 6402 km^2, and 5192 km^2 of burned area in the CCF, K, and SN ecoregions respectively (total of 18498 km^2 combined in a single year).

RdNBR frequency distributions were plotted for each ecoregion and for several dominant land cover types found throughout California, including needleleaf forest, closed and open shrubland, savanna, and grassland (Figure 17). RdNBR derived burn severity threshold ranges were recorded below (Table 7). The lower limit of the low burn severity threshold ranged from 0.13 in the SCC to 0.44 in the SCM. The lower limit of the moderate burned severity threshold ranged from 0.33 in the SCC to 0.63 in the SCM, while the lower limit of the high burn severity threshold ranged from 0.65 in the SCC to 0.82 in the SCM (Table 7). The upper limit of +1.5 for the high burn severity threshold was chosen because RdNBR values start to reach their asymptote in this range, and values above this limit are likely caused by misregistration, clouds, or other non-land cover related anomalies (Key and Benson 2005).

Table 7. RdNBR low, moderate, and high burn severity thresholds for each ecoregion derived from RdNBR cumulative distributions.

RdNBR Thresholds	**Low**	**Moderate**	**High**
So. CA Mountains	0.44 – 0.62	0.63 – 0.81	0.82 – 1.5
So. CA Coast	0.13 – 0.32	0.33 – 0.64	0.65 – 1.5
Central CA Foothills	0.21 – 0.4	0.41 – 0.63	0.64 – 1.5
Klamath	0.33 – 0.48	0.49 – 0.72	0.73 – 1.5
Cascades	0.32 – 0.49	0.5 – 0.69	0.7 – 1.5
East Cascades	0.23 – 0.4	0.41 – 0.66	0.67 – 1.5
Sierra Nevada	0.35 – 0.53	0.54 – 0.77	0.78 – 1.5

The cumulative frequency distribution of RdNBR values within ecoregions indicates that the SCC, CCF, and EC have the greatest frequency of RdNBR values <0.4, thus the lower limits to the low burn severity thresholds are lower than in other ecoregions (Figure 17, Table 7). Conversely, the SCM, SN, and K ecoregions have the lowest frequency of RdNBR values <0.4, thus the lower limit to these region’s low burn severity thresholds are comparably higher. According to the cumulative distribution, a greater number of pixels of RdNBR <0.4 will decrease the limit of the low burn severity class (i.e. SCC), while a distribution skewed towards higher RdNBR values will increase the lower limit (i.e. SCM). So, in this way, regardless of the variation in size of each ecoregion and the total number of burned pixels, it is the distribution of RdNBR values across the burn severity spectrum that determines each threshold.

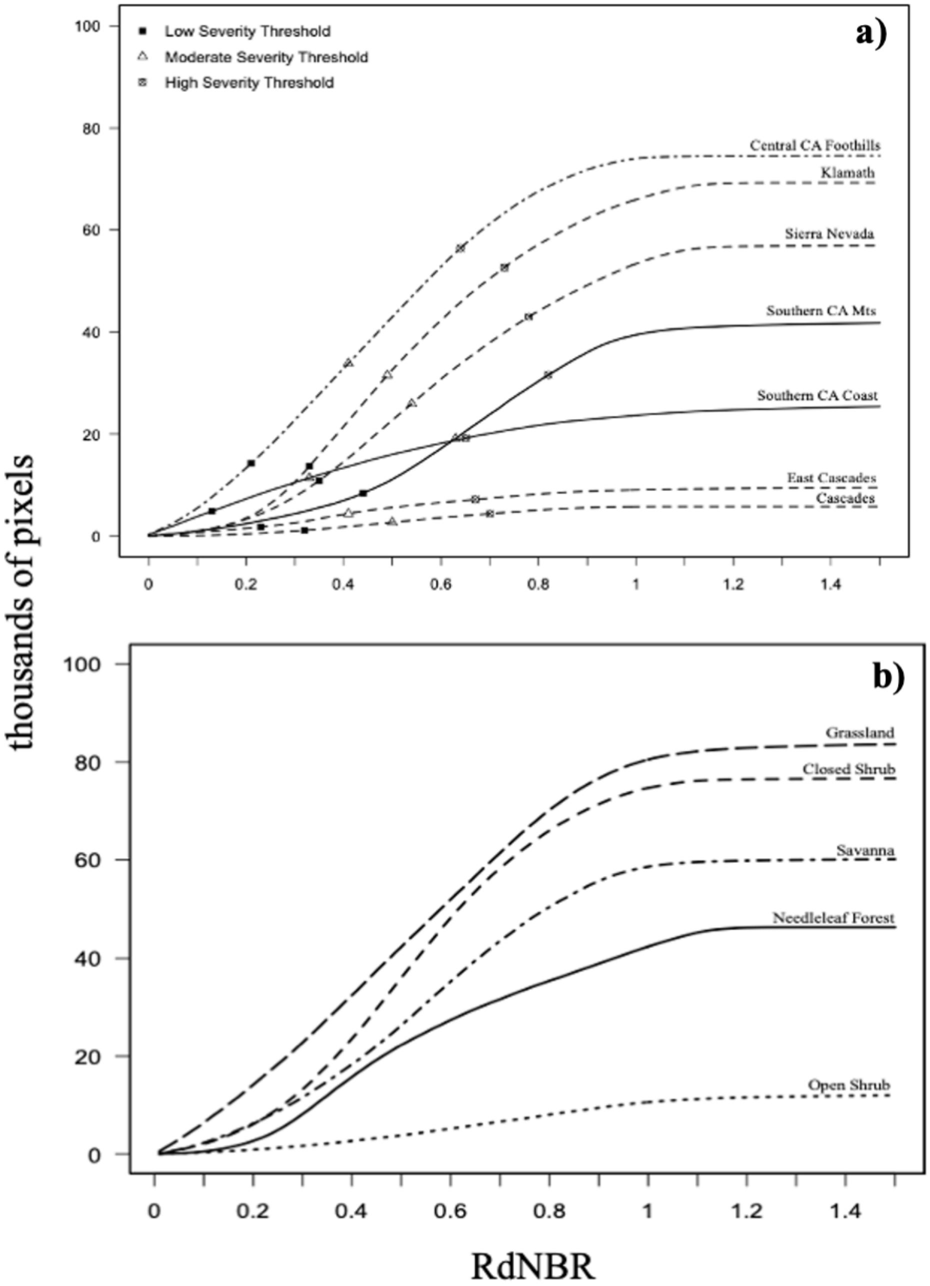

Figure 17. Histograms for RdNBR averaged for the entire study period of 2003-2020. Symbols mark the lower limits of low, moderate, and high burn severity class respectively; (a) RdNBR by ecoregion, and (b) RdNBR by individual vegetation type. Burn severity thresholds for each ecoregion were calculated from the cumulative frequency distribution of RdNBR pixel values (see Methods).

Similar analysis of the RdNBR histogram by vegetation type indicates that grasslands burn at low severity more than other ecoregions, while needleleaf forest and open shrub experience a greater frequency of RdNBR >0.8 (Figure 17b). While closed shrub burns at a greater frequency compared to savanna, their distributions of RdNBR values are similar until ~0.3, at which point the closed shrub distribution increases more rapidly through the moderate burn severity (0.4-0.6) range compared to savanna. Overall, grassland and closed shrub yielded the greatest number of pixels affected by some level of burn severity one-year post-fire (Figure 17b).

Correlations between average early-summer burn severity (RdNBR) and postfire NBR were all negative, with the strongest correlations in the SCM (-0.89) and SCC (-0.76) (Table 8). In addition, early-summer RdNBR and ΔEVI were highly negatively correlated for each ecoregion, indicating that high burn severity is associated with wildfire-induced vegetation removal (i.e. more vegetation burned by wildfire). Strong correlations between RdNBR and ΔEVI are expected because both indices are sensitive to infrared reflectance (Key and Benson 2005; Jin et al. 2012).

Table 8. Pearson temporal correlations (r values) between average early-summer burn severity (RdNBR) and burned area averages of six biophysical variables within each of the seven ecoregions of California.

	Southern California Mountains	Southern California Coast	Central California Foothills	Klamath Mountains	Cascades	Eastern Cascades	Sierra Nevada
Prefire NBR	**0.77**	0.04	0.42	0.28	**0.71**	-0.12	**0.58**
Postfire NBR	**-0.89**	**-0.76**	**-0.52**	**-0.61**	-0.43	**-0.55**	**-0.62**
Prefire EVI	**0.77**	0.18	0.36	0.27	**0.6**	-0.29	**0.47**
ΔEVI [a]	**-0.9**	**-0.57**	**-0.78**	**-0.83**	**-0.85**	**-0.82**	**-0.86**
Prefire LST	**-0.69**	-0.35	-0.26	-0.28	0.04	-0.12	-0.36
ΔLST	**0.87**	0.35	**0.69**	**0.77**	**0.67**	**0.84**	**0.89**

In addition, correlations between ΔLST and burn severity are all positive and significant (except for SCC), ranging from 0.69 (CCF) to 0.89 (SN) (Table 8). This positive relationship implies that larger increases in postfire land surface temperatures are associated with higher burn severity. These increases in postfire temperature associated with high severity fires have severe implications for ecosystem health and vegetation recovery.

3.3.2 Vegetation Recovery

The highest prefire EVI values and the greatest decrease of EVI after one-year post-fire, regardless of burn severity class, were found in the K, C, and SN ecoregions (Figures 18d, e, g). Early-summer EVI decreased in the year following wildfire due to vegetation removal, and high severity fires were associated with the largest decrease and lowest value of EVI one year later (Figure 18). Decreases in EVI for low severity fires after one year ranged from 0.02 in the SCC to 0.14 in the K, while decreases in EVI after high severity fires ranged from 0.06 in the SCC to 0.25 in the K (Figure 18).

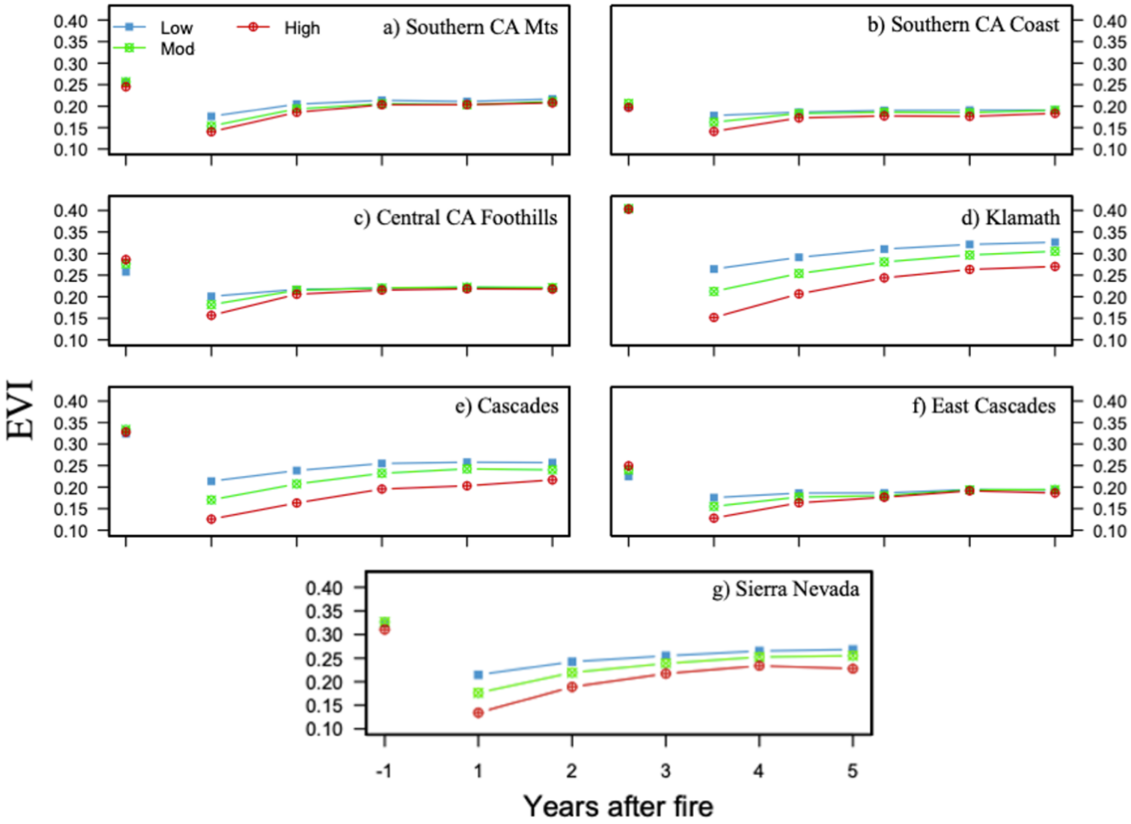

Figure 18. Prefire EVI and five-year early-summer postfire trajectory (a-g). Average early-summer postfire EVI for one year pre-fire through five-years post-fire for each ecoregion SCM, SCC, CCF, K, C, EC, and SN. Prefire and postfire EVi are burned area averages.

The rate at which EVI recovered towards the prefire value was different for each ecoregion. EVI did not recover to prefire levels after five years post-fire for any burn severity class in any ecoregion. However, during the first two years post-fire, EVI recovery occurred more rapidly after high severity burns in all ecoregions. Overall, the SCC exhibited the least amount of wildfire-induced EVI change while the K ecoregion had the largest. In addition, K had the fastest rates of recovery for all burn severity classes relative to the prefire averages. The comparatively quick recovery of EVI towards a plateau in the SCM, SCC, and CCF (~1-3 years) may be associated with the more rapid recovery of their predominant grassland and savanna vegetation types, as these ecoregions experienced a large proportion of low and moderate severity burns (Figure 18b). Also, five-year average early-summer EVI after high severity fires remained lower than all other burn severity classes.

3.3.3 Albedo Change

Average prefire albedo was highest in the SCM, SCC and CCF ecoregions (0.123 - 0.144) and lowest in the K, C, EC, and SN (0.101 - 0.124) (Figures 19a, b, c). The East Cascade ecoregion had the largest variation in average prefire albedo among burn severity classes (0.01). Prefire albedo values were lowest in high severity burned areas in the SCM, SCC, CCF, C, and EC ecoregions.

In the first year after fire, albedo decreased below prefire levels in all three burn severity classes in the K, C, EC, and SN ecoregions, but increased above prefire levels in the SCM, SCC, and CCF. In the K, C, EC, and SN, albedo levels generally increased continuously for five years post-fire, and albedo values in the fifth-year post-fire were above prefire levels in the C, EC, and SN.

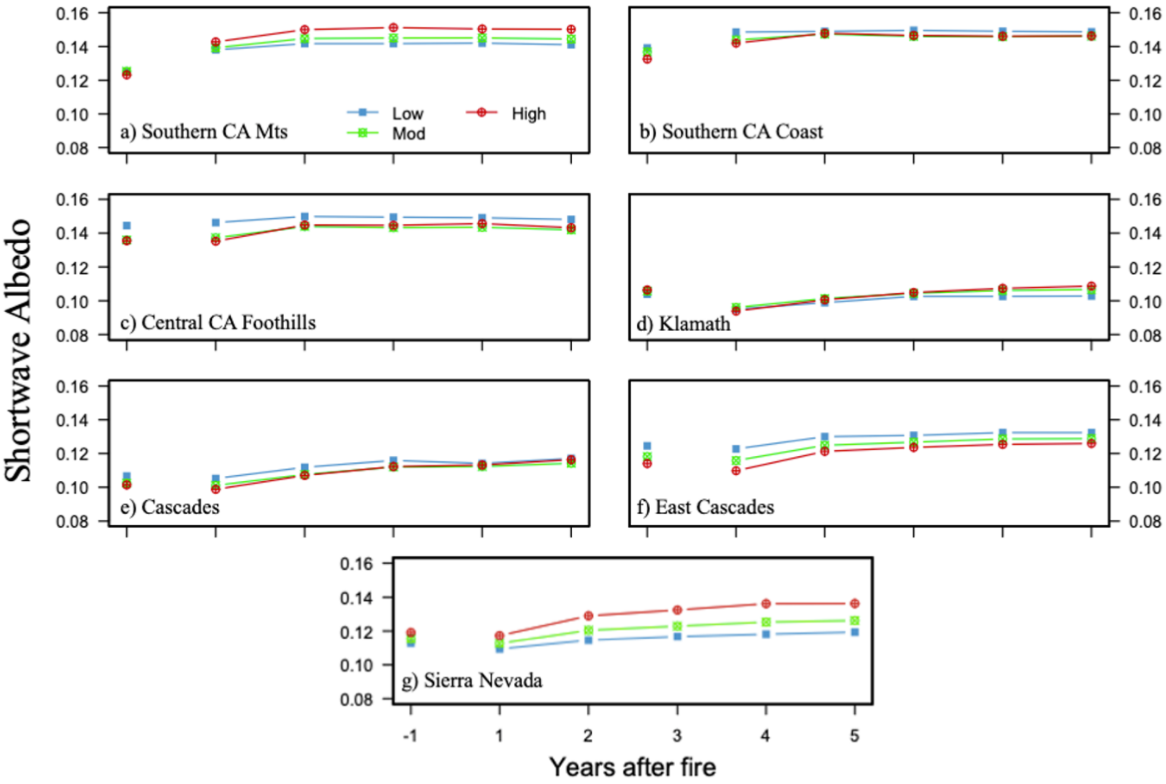

Figure 19. Prefire albedo and five-year early-summer postfire trajectory (a-g). Average early-summer surface shortwave albedo response for the first-year post-fire through five-years post-fire for each ecoregion SCM, SCC, CCF, K, C, EC, and SN. Prefire and postfire albedo area burned area averages.

Postfire trajectories in the SCM, SCC, and CCF displayed different behavior relative to the northern California ecoregions. Whereas the K, C, EC, and SN ecoregions experienced one-year postfire decreases, albedo values increased up to 0.02 in the SCM and 0.01 in the SCC after the first year, with the largest increases in the most severely burned areas (Figures 19a, b). However, albedo in the CCF did not change substantially in any burn severity class after one year, but both the moderate and high burn severity class had an increase between year one and two (Figure 19c). In the ecoregions that experienced decreases after the first-year post-fire, albedo values tend to exceed prefire values by years two and three (Figures 19d-g).

3.3.4 Land Surface Temperature

Average prefire LST is lowest in the K ecoregion (305.4 K) and highest in the SCC (316.68 K) (Figure 20, Table 6). The greatest prefire LST difference among burn severity classes within a single ecoregion is 1.9 K in the CCF. However, prefire LST in regions that experienced high severity fires was higher than it was in regions of low and moderate severity in K, SN, SCM, and SCC ecoregions. LST increased in the first-year post-fire in all ecoregions regardless of burn severity, and the greatest increases in LST were associated with high severity fires (Figure 20). Increases in LST after low severity fires ranged from 3.1 in the CCF to 5.8 K in the SCM, while increases in LST after high severity fires ranged from 5.5 K in the EC to 8.6 K in the SCM.

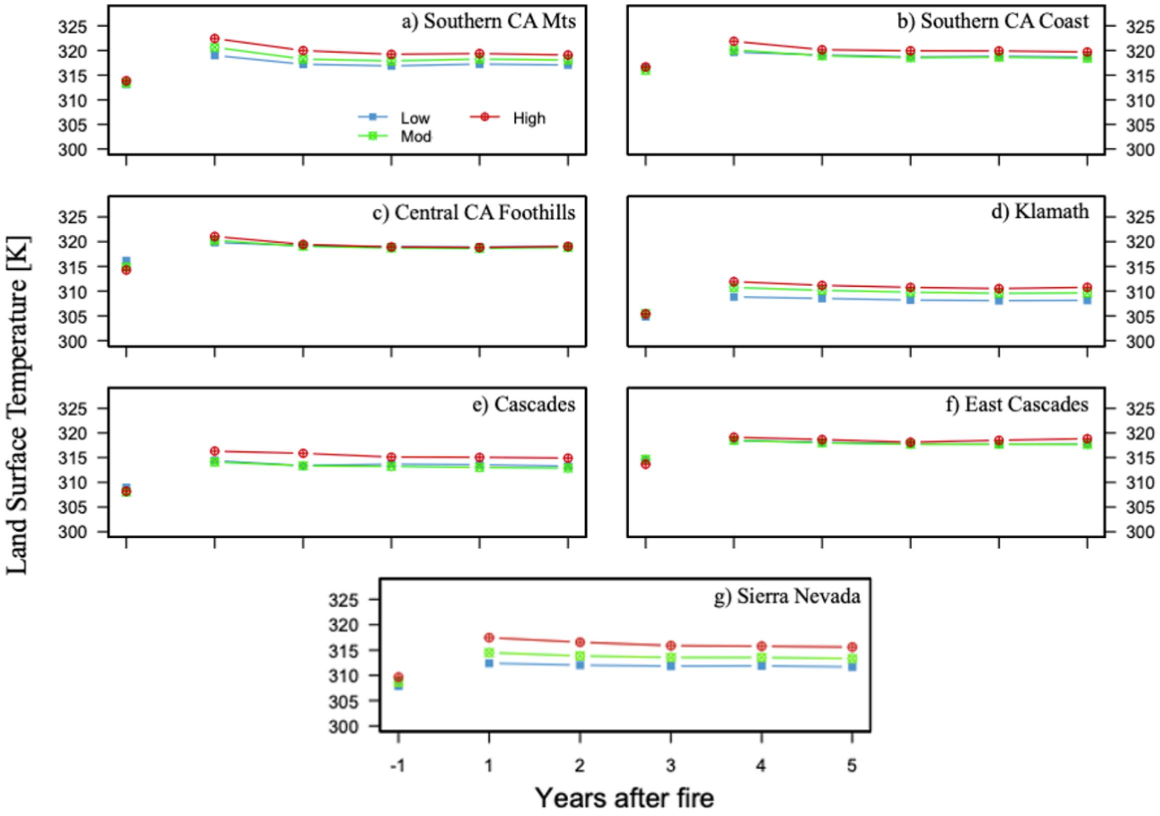

Figure 20. Prefire land surface temperature and five-year early-summer postfire trajectory (a-g). Average early-summer land surface temperature first-year pre-fire

through five-years post-fire for each ecoregion SCM, SCC, CCF, K, C, EC, and SN. Prefire and postfire LST are burned area averages.

The rate at which LST recovered towards prefire levels was different for each ecoregion, however, overall, postfire LST did not return to prefire temperatures after five years in any ecoregion in any burn severity class. Furthermore, LST after high severity fires rose to a higher temperature and remained elevated over temperatures in low and moderate burn severity areas in the SCM, SCC, K, C, and SN. Across all ecoregions and burn severity classes, the trajectory of postfire temperature over five years tended to remain stable, with minimal increases and decreases in temperature after the initial postfire increase in the first year.

3.4 Discussion

3.4.1 Role of Burn Severity in Vegetation Recovery

We found that three features account for most of the covariation between vegetation recovery response and burn severity in California's ecoregions. First, the largest decreases in first year postfire EVI, regardless of burn severity class, occur in the same ecoregions that have the highest mean prefire early-summer EVI (i.e. K, C, and SN) (Table 5, Figure 18). This pattern indicates that all fires, regardless of burn severity level, tend to result in greater amounts of vegetation removal in ecoregions with high prefire EVI (e.g. high biomass areas). For example, the average prefire EVI value for low severity fires in the Klamath ecoregion is 0.4, and the average ΔEVI one-year post-fire is 0.14. So, even though ΔEVI is greatest for high severity fires across ecoregions, the SCC ecoregion, with one of the lowest average prefire EVI values for high severity fires (0.2) experiences a 0.06 one-year postfire decrease - less than half of the Klamath ecoregion's low severity ΔEVI. Our results that show strong correlations between RdNBR and ΔEVI, as well as large prefire EVI in northern California ecoregions that experience the greatest first-year ΔEVI, are consistent with studies that found that higher prefire EVI in the Cascade and Klamath regions of northern California were associated with a greater likelihood of high severity fires (Yang et al. 2017; Parks et al. 2018; Meigs et al. 2020). Furthermore, Parks et al. (2018) found that low severity fires were more likely to occur in areas with lower prefire EVI, which is similar to what we found in the spatial distribution of RdNBR derived burned area in southern California (2018a) (Figure 15b). In addition, the impact of wildfire on NDVI, a similar vegetation index as EVI, was greater for needleleaf trees than it was for shrubs, an effect that was corroborated with satellite imagery and aerial photos (Thompson and Spies 2009).

Second, fires that burned at high severity are associated with greater ΔEVI across all ecoregions compared to less severe fires (Figure 18). In other words, changes in the amount of live fuel between the prefire and one-year postfire images increases with burn severity. This relationship, demonstrated by the strong negative correlation between ΔEVI and RdNBR (i.e. large changes in EVI after higher severity fire), is expected, as both indices are primarily influenced by the magnitude of change between near and shortwave infrared wavelengths. However, the high correlation observed between ΔEVI and RdNBR may also be a result of the previously mentioned association between vegetation type and degree of EVI or NDVI change (Yang et al. 2017).

The third feature that describes the relationship between postfire vegetation recovery and burn severity is the rate at which EVI approaches prefire levels over the course of five years. Throughout the five-year postfire interval, relative to average prefire EVI values, EVI recovers faster after high severity fires in all ecoregions. Rapid recovery of vegetation in the first years after wildfire is likely due to the growth of shrubs and other herbaceous vegetation.

Furthermore, our results are corroborated by other studies that show that, while NDVI (a vegetation index similar to EVI) recovers fastest during the first two to three years post-fire, the effects of high severity burns can still be observed five or more years later, and lower NDVI values were found after high severity fires (Collins and Roller 2013; Crotteau et al. 2013; Meng et al. 2015). Further, in the ecoregions that had smaller ΔEVI after the first year (i.e. SCM, SCC, CCF, EC), EVI trajectories for low, moderate, and high burn severity tended to converge by the third-year post-fire (Figures 18a-c, f). By identifying which ecoregions are more likely to experience high severity burns, land and fire management can focus resources on areas experiencing high degrees of postfire ecological change and erosion, or are at an increased risk for habitat endangerment (Miller and Thode 2007; Keeley 2009).

3.4.2 Burn Severity and Albedo Change

One of the most immediate effects of wildfire on the land surface is the removal of vegetation and the deposition of ash (De Sales et al 2018; Rother and De Sales 2020). By definition, high severity fires are often stand replacing disturbances that lead to rapid changes in the biophysical characteristics of the land surface. Abrupt changes to the partitioning of energy from latent to sensible heat flux (associated with the removal of vegetation) can increase the amount of net radiation available at the surface (Chambers et al. 2005; Rother and De Sales 2020).

Postfire albedo change may be highly dependent on plant type, phenology, and burned severity, as a predominantly forested region will likely experience a different postfire albedo trajectory than a grassland or savanna (Figures 19c-d). Postfire albedo may decrease after high severity fire in a biomass rich area like the K, C, or SN ecoregion for a year or more because forest recovers at a slower rate than grassland and shrub (Figures 19d-e, g). On the other hand, ecoregions that contain predominantly grassland and savanna land cover types (i.e. SCM, SCC) are more likely to experience initial increases in postfire albedo, as one year is a sufficient amount of time to remove all traces of ash deposited on the surface and for vegetation to start recovering (Figures 19a-b). It is important to note that ash residence time varies widely, and decreases in albedo caused by ash deposition can be offset by the regrowth of early successional plants like shrubs and grasses, which tend to have higher albedos (Lyons et al. 2008; Jin et al. 2012; Bodi et al. 2014; Meng et al. 2014). In fact, one study found that albedo increases in the first postfire summer are likely related to exposure of bare ground after ash is dispersed in the winter, while subsequent increases each year following are due to the regeneration of vegetation (Veraverbeke et al. 2012). This effect was observed within the SCM, SCC, and CCF ecoregions, where albedo in the first-year post-fire increased, while the K, C, EC, and SN ecoregions experienced decreases (Figure 19).

Prefire albedo levels were lower, and fires of all severity levels resulted in greater decreases in the K, C, and SN ecoregions relative to the SCM, SCC, CCF, and EC, likely due to the differential effects of fire on vegetation with higher EVI values. In addition, ecoregions with an abundance of live fuel (i.e. high EVI), tend to have lower albedos. Thus, greater average pre-fire EVI and lower average pre-fire albedo are both associated with high severity fires. Additionally, seasonal differences in albedo may also be responsible for some of the variation in first-year postfire values, as soil moisture content and plant growth during and after the rainy season has a direct effect on albedo (Samain et al. 2008; Veraverbeke et al. 2012).

3.4.3 Burn Severity and Land Surface Temperature

To our knowledge, a small number of studies have investigated the connections between burn severity and land surface temperature, and only a few for regions within the state of California (Harris et al. 2011; Veraverbeke et al. 2011; Veraverbeke et al. 2012; Zheng et al. 2016). Further investigation into the relationships between burn severity, vegetation recovery, and LST may lead to the use of LST as indicators of burn severity, as postfire increases in temperature were found to change proportionately with NDVI and slowly return to pre-fire levels as vegetation recovers (Harris et al. 2011). Additionally, the analysis of postfire recovery patterns of land surface temperature will strengthen our understanding of the impacts of fire on surface energy balance and improve the reliability of simulated land surface processes within models.

Albedo and land surface temperature are closely related biophysical characteristics of the land surface that are impacted by wildfire and burn severity (Vlassova et al. 2014; Zheng et al. 2016). Wildfire-induced alterations to the land surface can persist for years, leading to increased aridity, as well as changes to diurnal energy and temperature fluctuations. In fact, there may be significant seasonal variation in the wildfire related impact on land surface temperature, with large changes during the summer and small changes during the winter (Veraverbeke et al. 2012). However, the initial decrease in albedo and increases in radiation absorption and surface temperature associated with post-fire ash deposition tends to be short-lived, as the gradual process of plant regeneration contributes to the return of land surface temperatures to their pre-disturbance levels.

Here, the relationships between ΔEVI, ΔLST, and burn severity are less clear, as LST increased post-fire in all ecoregions, but remains elevated for the duration of the postfire years, regardless of the amount of EVI recovery (Figures 18 and 20). For example, the K, C, and SN had the greatest ΔEVI in the first-year post-fire, as well as the fastest rate of recovery towards prefire levels, however, increases in LST in these ecoregions remain mostly stable, only gradually diminishing towards average prefire LST over five years. A study extending further than five years post-fire would be necessary in order to investigate the length of postfire temperature change in California ecoregions.

The projected impacts of climate change on California ecosystems, including increasing temperatures and vapor pressure deficit, may significantly alter existing fire regimes (Zhang et al. 2020; Zhong et al. 2021). In general, warmer temperatures and drier conditions increase the risk for wildfire (assuming the presence of vegetation), and the addition of further postfire increases in temperature may push already stressed ecosystems past their ability to adapt (Johnstone et al. 2016).

3.5 Conclusions

We analyzed the influence of burn severity on vegetation recovery, albedo, and land surface temperature in seven California ecoregions between the years 2003 and 2020 based on MODIS satellite data derived products. Normalized Burn Ratio datasets were used to calculate RdNBR for the entire state for the duration of the study period. Early-summer averages were stratified into three burn severity classes and their prefire average and trajectory for the first five years post-fire plotted. Strong negative correlations were found between postfire NBR and RdNBR, as well as ΔEVI and RdNBR. We found that the largest decreases in EVI after one-year post-fire occur in the ecoregions with the highest prefire EVI values (i.e. K, C, SN). In addition, the greatest decrease in EVI and the fastest recovery towards prefire values occurred after high severity fires (in all ecoregions). Also, EVI did not recover to prefire values after five-years post-fire in any burn severity class in any ecoregion. We found that the lowest prefire albedo values occurred in the same ecoregions with the highest prefire EVI. First-year postfire albedo decreased in the K, C, EC, and SN ecoregions, but increased after one year in the SCM, SCC, and CCF. Differences in first-year postfire change are likely due to variations in the duration of ash residence times, rate of plant regeneration, and average albedo of early successional plants (such as grasses and shrubs). After five years post-fire, albedo values were larger than prefire values in all ecoregions except K. We found that first-year postfire increases in LST were greatest within high severity burned areas. All ecoregions experienced a postfire increase in LST that remained relatively stable throughout the five-years post-fire with only gradual decreases towards prefire levels.

An improved understanding of the biophysical response to large-scale wildfires becomes increasingly important as California's high summertime temperatures and seasonal summer droughts continue to drive record-breaking fire seasons. Furthermore, the spatial distribution of burn severity, along with a comprehensive understanding of postfire response of important indicators of ecosystem health (like the presence of vegetation and large changes in LST), can inform fire and land management in their efforts to effectively mitigate and suppress large wildfires in key areas. In addition, the temporal analysis of postfire EVI, albedo, and temperature may improve the accuracy and inform the conceptualization of future modeling of wildfire impacts on land surface processes.

Chapter 4. Summer and Fall Extreme Weather Projected to Occur More Often and Affect a Growing Portion of California throughout the 21st Century

4.1 Introduction

Numerous research studies indicate that wildfire activity in the western United States has increased over the past few decades due primarily to increases in temperature, decreases in precipitation, and increases in atmospheric aridity (Abatzoglou and Williams 2016; Keeley and Syphard 2016; Williams et al. 2019; Goss et al. 2020; Dong et al. 2021). Furthermore, by the end of the 21st century, anthropogenic global warming will contribute to increased risk of extreme fire weather through the effect of rising temperatures (Touma et al. 2021). However, the impacts of climate on fire regime vary dramatically by ecosystem, predominant vegetation types, topography, and human activity. These complex relationships between climate and wildfire are apparent in California, where climate, vegetation, and topography vary significantly from east to west and north to south.

For example, large parts of southern California experience near continuous high fire danger in the summer and fall, as high temperatures, seasonal drought, and the onset of the Santa Ana wind season combine to increase the risk of severe wildfire. In these areas, wildfire is rarely limited by weather conditions governing fire spread, but by availability of fuel to burn. On the other hand, in forested ecosystems, where deep rooted vegetation is less susceptible to short-term variations in moisture, the limiting factor may be fire spread potential or dried fuel available to burn (Bonan 2008; Bradstock 2010). Therefore, the effects of climate change on wildfire in California, specifically projected increases in temperature and aridity, will not impact all ecosystems equally, but will be strongly dependent on vegetation distribution and will be more likely to place flammability-limited ecosystems (i.e., forested) at a greater risk for catastrophic wildfire (McKenzie and Littell 2017; Littell 2018). Furthermore, understanding the broad range of outcomes regarding the impacts of climate change on extreme fire weather risk is critical because climate change may lead to the loss of existing climate regimes and the emergence of novel ecosystem states, impacting the distribution of biomass (i.e., continuity and flammability), fire spread potential, and ignition (Williams et al. 2007; Johnstone et al. 2016).

One of the most valuable tools for assessing historical and projected climate variability, especially the meteorological variables that govern wildfire on a regional scale, are global climate models, or GCMs (Abatzoglou and Brown 2012). The Coupled Model Intercomparison Project (CMIP) provides a standardized platform for the collection and analysis of GCM model output with the intent of studying natural and anthropogenic climate variability. The most recent release of GCM output for the CMIP Phase 6 provides a new suite of climate model data for use in a wide range of disciplines. While GCMs are often used for the evaluation of long-term variations in climate, there are significant limitations to their use for the study of wildfire impact assessment and fire weather potential. The main limitation is that climate model output is typically of coarse resolution and is subject to significant bias (Abatzoglou and Brown 2012). The mismatch between the spatial scale at which key variability in fire weather variables fluctuate (<10-km), and that of GCM output (>100-km), creates a need to account for these spatial differences.

One method of adjusting the resolution of available GCM output to that which is needed for the evaluation of fire weather variables is statistical downscaling. These methods allow for the reduction in systematic biases inherent to numerical weather prediction systems, as well as an enhancement of grid cell resolution in order to account for the effects of topography and other land surface features (Li et al. 2010). One method of statistical downscaling for use in wildfire risk assessment is bias correction and spatial downscaling (BCSD) (Abatzoglou and Brown 2012). BCSD is a two-step process that involves the bias correction of coarse-scale GCM data using local observations that have been aggregated to the model's resolution (Abatzoglou and Brown 2012). Bias correction techniques include scaling, delta methods, and empirical quantile mapping. In addition, spatial downscaling utilizes techniques such as linear or multiple regression to apply statistical relationships (e.g., slope, y-intercept) derived from high resolution observational data to coarse resolution GCM data in order to improve the resolution (Zhang et al. 2020). The major assumption made with statistical downscaling methods is that of climate stationarity. It is assumed that the relationships between the coarse and fine scale historical datasets, calculated by the statistical model, will stay the same in the future (with climate change), and that when these models are applied to projected datasets the outcomes will be valid (Li et al. 2010; Abatzoglou and Brown 2012; Zhang et al. 2020).

In order to track changes in, and probability of, extreme fire weather over time, fire weather indices are often calculated using weather station, reanalysis, or global climate model data. Two commonly used fire weather indices are vapor pressure deficit (VPD) and the Canadian Fire Weather Index System (CFWIS) (van Wagner 1987; Lawson and Armitage 2008). The CFWIS relies on regular inputs of noon-day temperature, 24-hr precipitation accumulation, 10-m wind speed, and relative humidity, and is comprised of six components: three fuel moisture codes and three fire behavior metrics, with the primary purpose of assessing the effect of weather on fuels and potential fires. In general, higher values indicate a more severe risk for ignition or spread of large wildfire (Lawson 1977; Lawson and Armitage 2008).

On the other hand, VPD, defined as the difference between saturation vapor pressure and actual vapor pressure, is a commonly used metric for the quantification of atmospheric aridity in relation to wildfire risk assessment, and is highly correlated with annual area burned (Seager et al. 2015; Abatzoglou and Williams 2016; Williams et al. 2019). VPD accounts for the non-linear (exponential) relationship between saturation vapor pressure and temperature, thus better representing moisture stress and flammability (Seager et al. 2015). In fact, maximum VPD in the entire United States is found each year in the desert southwest region, not only affecting agricultural production via crop health but increasing the risk of wildfire ignition and spread (Seager et al. 2015). Furthermore, two-thirds of historical (2001-2018) increases in extreme VPD in the western United States is attributable to anthropogenic warming (Zhuang et al. 2021).

The objective of this research is to utilize bias correction and statistical downscaling to enhance the spatial representations of CMIP6 simulations for the purposes of assessing the potential impacts of climate change on the occurrence of extreme fire weather. Bias corrected and statistically downscaled daily CMIP6 data (~4-km spatial resolution), covering an historical (1981-2010), mid-century (2041-2070), and late-century (2071-2100) period, will be used as input for two fire weather indices, including the Canadian Fire Weather Index (CFWIS; now referred to as FWI) and vapor pressure deficit (VPD). In order to determine the effects of climate change on the occurrence of extreme fire weather in California ecoregions, we investigate the frequency at which daily index values exceed the average daily historical 95th percentile. We also calculate the extent of each ecoregion that is likely to experience values greater than the 30-year average spatial 95th percentile value for each time period. In addition, time series analysis includes fire weather anomalies relative to an historical period, as well as 30-year Julian-day averages. The diversity of factors that influence fire regime in California, as well as the immense range of biophysical characteristics, require an ecoregion scale analysis. The effects of climate change on extreme fire weather will not be homogeneous, however, our fine scale analysis will allow policy makers and land managers to anticipate changes in climate and determine the areas that are most likely to experience the consequences of increased fire potential.

4.2 Materials and Methods

4.2.1 Study Area

The primary study area is California (Figure 21). We chose to analyze the effects of climate change on extreme fire weather within ten ecoregions of California (Griffith et al. 2016; Level III and IV Ecoregions of Continental United States 2021). These regions include the Southern California Mountains (SCM), Southern California Coast (SCC), Central California Foothills (CCF), Central Valley (CV), North American Desert (NAD), Sierra Nevada (SN), Klamath (K), Cascades (C), East Cascades (EC), and Marine West Coast Mountains (MWCM).

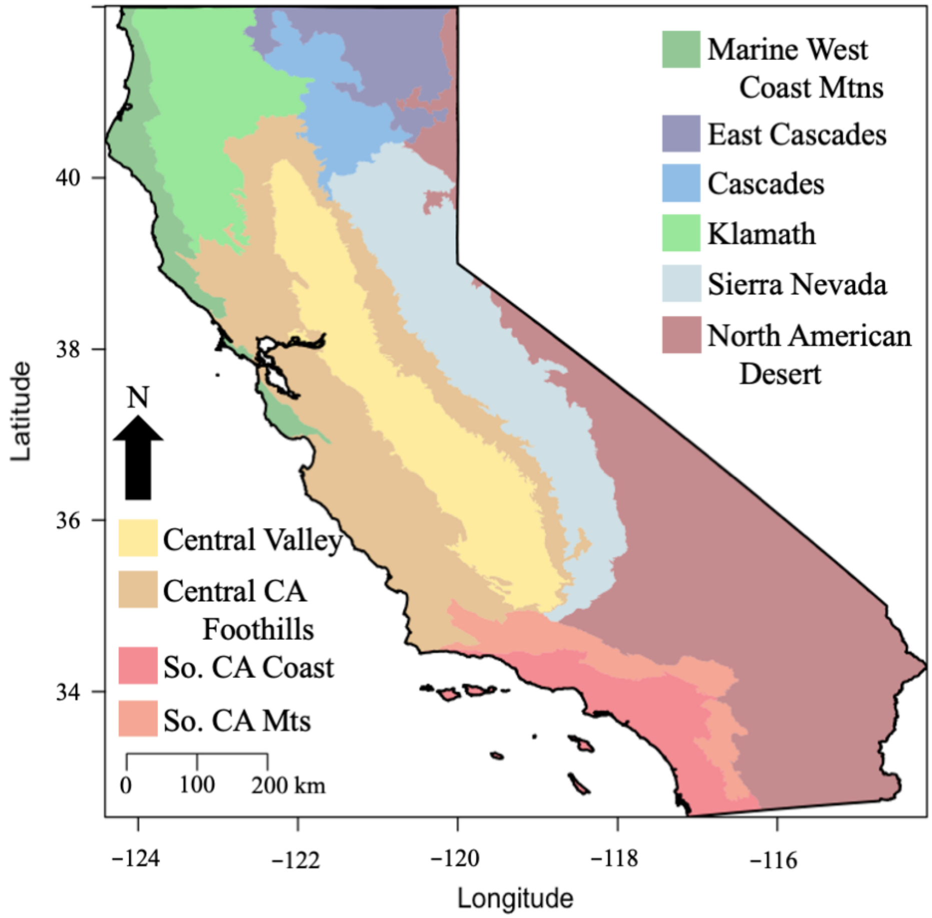

Figure 21. Ecoregions of California, including the Southern California Mountains (SCM), Southern California Coast (SCC), Central California Foothills (CCF), Central Valley (CV), North American Desert (NAD), Sierra Nevada (SN), Klamath (K), Cascades (C), East Cascades (EC), and Marine West Coast Mountains (MWCM).

Each of these regions is characterized by different dominant ecosystem types that give rise to California's diverse fire regimes, including vegetation, climate, soil types, land use, and hydrology (Griffith et al. 2016). An ecoregion specific analysis will allow for a nuanced understanding of how climate change may impact extreme fire weather relative to historical conditions within homogeneous regions of particular climate and vegetation types.

4.2.2 Statistical Downscaling Method

Daily near surface maximum air temperature, 24-hr precipitation accumulation, 10-m wind speed, and 2-m relative humidity were acquired for three CMIP6 models (including MIROC6, EC-Earth3, and MRI-ESM2-0), for an historical (1981-2010), mid-century (2041-2070), and late-century (2071-2100) period, from the data repository at the Earth System Grid Federation (https://esgf-node.llnl.gov/search/cmip6/, accessed on 1 January 2021). We derived daily relative humidity from specific humidity, sea level pressure, geopotential height, and near surface air temperature. Future climate projections for a mid- and late-century period were obtained for the Representative Concentration Pathway (RCP8.5), “high emissions” scenario. All bias correction and downscaling methods were completed using a 4-km gridded meteorological climate dataset called gridMET (Abatzoglou 2013). We used the entirety of the gridMET historical period (i.e., 1979-2014) to train the bias correction algorithm, and in order to avoid training and testing our BCSD output with the same data (i.e., gridMET), we validated the results of the BCSD methodology with two independent observational datasets (see Section 4.3.1).

A bias correction technique known as empirical quantile mapping was applied separately to the four climate variables for each of the three CMIP6 model outputs. This algorithm adjusted the simulation’s (i.e., CMIP6) empirical distribution based on observed patterns (i.e., gridMET) and was used to correct both historic and future climate projections generated by the CMIP6 models (Li et al. 2010). Bias correction methods are often applied to GCM output in order to address inherent biases that arise when modeling earth system processes. The bias corrected GCM data was interpolated to the high-resolution observational grid (i.e., gridMET) using a thin plate spline function and the relationship between the two grids were then estimated to generate regression functions for each grid cell (Hancock and Hutchinson 2006). The linear regression models were then applied to the bias corrected and interpolated GCM data to complete the downscaling.

To elaborate, this spatial downscaling methodology uses regression functions to estimate the linear relationships (in this case the slope and intercept) between the original, high-resolution gridMET data and a "smoothed" estimate, before applying those statistical parameters to the bias corrected CMIP6 data in a simple linear model to obtain the final downscaled, high-resolution output (Hoar and Nychka 2022). For this research, the study area domain was comprised of approximately 70-100 grid cells in the CMIP6 simulations, whereas the gridMET observational data has ~81,000 locations over the same area. In the first step, a thin plate spline interpolation was used to predict CMIP6 values at the gridMET scale, with no addition of topographic or climatological information. This resulted in "smoothed" CMIP6 data that is identical to the original data but sampled at a much greater frequency. In the next step, a linear regression function was derived from the raw and smoothed gridMET datasets at each grid cell location, for each month of the year (~81,000 grid cells × 12). These month-specific linear regression models were applied to the "smoothed" CMIP6 data to obtain the final downscaled product for each variable.

A square-root transformation was applied to the precipitation data before downscaling to account for its skewed distribution (Juras 1994; Fu et al. 2010). The final bias corrected and downscaled product of each variable was averaged to obtain an ensemble mean and used in the calculation of the two fire weather indices. Daily maximum temperature, 24-hr rainfall, 10-m wind speed, and daily minimum relative humidity were used to calculate FWI, while daily maximum temperature and daily minimum relative humidity are used to calculate VPD.

Due to the fact that maximum temperature and minimum relative humidity are used for the calculation of VPD, we make it clear that VPD may be considered "maximum VPD".

4.2.3 Climate Model Simulations of Extreme Fire Weather in California Ecoregions

The BCSD CMIP6 GCM data were used for three primary analyses of extreme fire weather in California, as well as an additional analysis of Julian-day climatology. We used maximum daily surface temperature, minimum relative humidity, and 2 pm wind speed, as daily noon-time data requirements were not available for all models. Prior to the analysis, 1979-2014 BCDS product was validated against two observational analysis datasets, the North American Regional Reanalysis (NARR, psl.noaa.gov/data, accessed on 1 March 2022) and TerraClimate (Mesinger et al. 2006; Abatzoglou et al. 2018).

Analysis of extreme fire weather consisted of four main components. First, we calculated the June, July, August (JJA) and the September, October, November (SON) seasonal-mean FWI and VPD averages for each ecoregion, as well as for the entire state of California, for an historical (1981-2010), mid-century (2041-2070), and late-century (2071-2100) time period. The historical mean, calculated individually for each ecoregion and for each season, was used as a baseline with which the mid-century and late-century anomalies were calculated. In addition, the relative change (relative to the historical time period) of FWI and VPD in the mid- and late-century periods was calculated. We consider a unique baseline for each ecoregion, in addition to a California state-wide assessment, for each season, in order to properly account for the entire range of climate conditions found across California, and to assess projected changes in each zone relative to their particular local historical climate.

Second, the seasonal, ecoregion specific, daily FWI and VPD averages were used to calculate a 95th percentile value (FWI_{95}; VPD_{95}), which was then used as a threshold for the mapping of the frequency with which fire weather indices exceed that 95th percentile value during the historical, mid- and late-century periods. The maximum occurrence of a given index value above the 95th percentile is 91, or, in other words, all the days in that season in a given year. In order to evaluate the spatial distribution of extreme fire weather throughout the 21st century, the difference in the total number of days per year that exceed the 95th percentile was taken between the mid- and late-century and the historical period. In addition, the ecoregion average number of days per year that exceed the 95th percentile was calculated.

Third, 30-year JJA and SON seasonal average FWI and VPD were calculated for each ecoregion. Considering all grid points within each ecoregion for that 30-year average, the 95th percentiles are calculated and subsequently used as thresholds to determine the extent within each region that will experience FWI and VPD exceeding those values. Frequency distributions of 30-year spatial average FWI and VPD values were plotted for each ecoregion.

Finally, Julian-day averages spanning the entire 30-year periods were calculated for FWI and VPD. Daily climatologies intend to show changing peaks in average maximum values, as well as the lengthening or shortening of each ecoregion's fire season.

4.3 Results

4.3.1 Validation of Historical Simulations

Before investigating the impacts of climate change on extreme fire weather, we evaluate the CMIP6 Raw and BCSD ensembles against an observational ensemble that includes NARR and TerraClimate. However, TerraClimate has not released a minimum relative humidity dataset, so in this case, CMIP6 was validated exclusively with NARR. Spatial statistics, including correlation, bias, and root-mean square error (e.g., sCor, sBias, sRMSE) were calculated after resampling all observations and Raw CMIP6 data to the high resolution BCSD (~4-km). In this way, the improved skill of the bias correction and downscaling was demonstrated against a basic resampling. Temporal statistics (tCor, tBias, tRMSE) were calculated using monthly averages spanning the entire historical period (1979-2014). The difference in resolution between the TerraClimate observations (~4-km), raw MIROC6 (1.4° × 1.4°), and BCSD ensemble (~4-km) are shown below for annual average maximum temperature in 1979 (Figure 22).

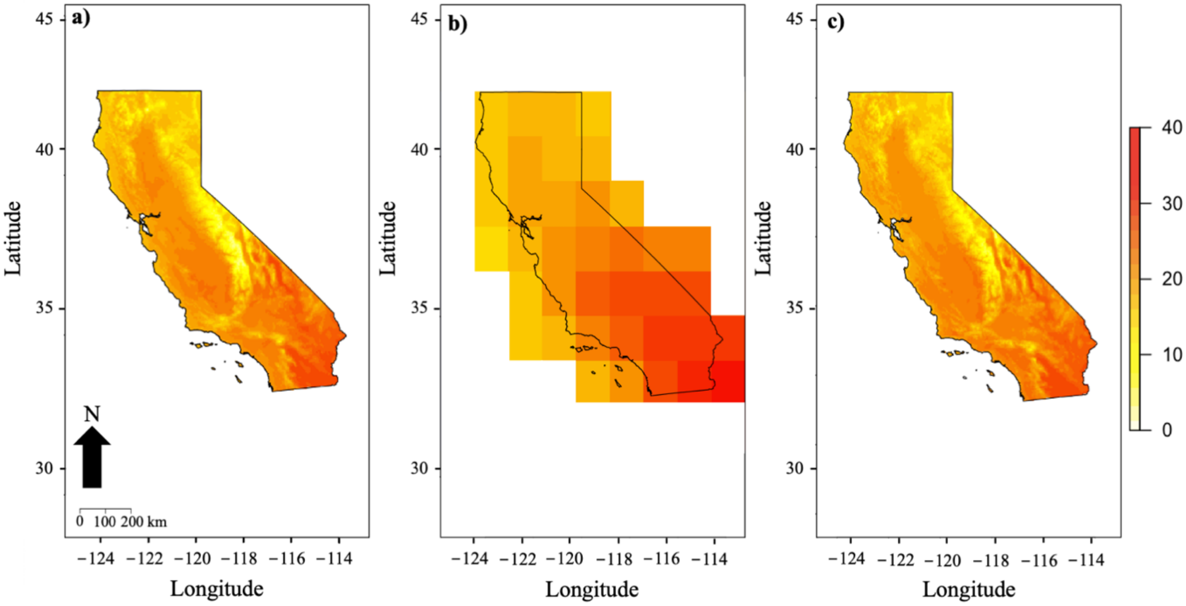

Figure 22. Average maximum temperature for 1979 (a) TerraClimate (b) Raw MIROC6 (c) BCSD Ensemble. Units: °C.

Spatial correlations between CMIP6 BCSD and the observations were high for all variables, especially for maximum temperature, precipitation accumulation, and minimum relative humidity, with 0.97, 0.88, and 0.87, respectively—all of which were higher relative to the CMIP6 Raw (Table 9). Furthermore, sRMSE and sBias were higher for the CMIP6 BCSD relative to the CMIP6 Raw for all variables except temperature, which showed a higher sBias in the CMIP6 Raw. A substantially higher sCor and sBias in the wind speed resulted between the Raw and the BCSD, with sCor increasing by 0.4 and sBias by 0.38 (Table 9).

Table 9. Spatial statistics (i.e. sCor) evaluating a 36-year average historical period (1979-2014) of the raw CMIP model ensemble and the bias corrected and spatially downscaled CMIP model ensemble, against the NARR/TerraClimate validation dataset. Temporal statistics (i.e. tCor) are based on 36 years of monthly averages. Standard deviation is shown in parentheses. Spatial correlations are significant at p < 0.001.

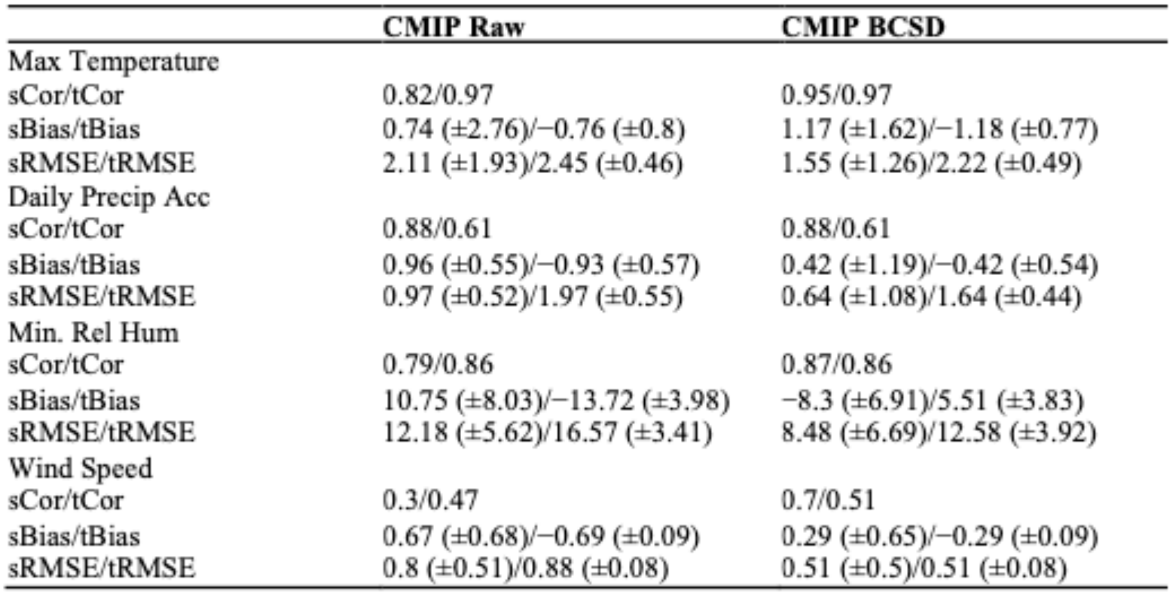

	CMIP Raw	**CMIP BCSD**
Max Temperature		
sCor/tCor	0.82/0.97	0.95/0.97
sBias/tBias	0.74 (±2.76)/−0.76 (±0.8)	1.17 (±1.62)/−1.18 (±0.77)
sRMSE/tRMSE	2.11 (±1.93)/2.45 (±0.46)	1.55 (±1.26)/2.22 (±0.49)
Daily Precip Acc		
sCor/tCor	0.88/0.61	0.88/0.61
sBias/tBias	0.96 (±0.55)/−0.93 (±0.57)	0.42 (±1.19)/−0.42 (±0.54)
sRMSE/tRMSE	0.97 (±0.52)/1.97 (±0.55)	0.64 (±1.08)/1.64 (±0.44)
Min. Rel Hum		
sCor/tCor	0.79/0.86	0.87/0.86
sBias/tBias	10.75 (±8.03)/−13.72 (±3.98)	−8.3 (±6.91)/5.51 (±3.83)
sRMSE/tRMSE	12.18 (±5.62)/16.57 (±3.41)	8.48 (±6.69)/12.58 (±3.92)
Wind Speed		
sCor/tCor	0.3/0.47	0.7/0.51
sBias/tBias	0.67 (±0.68)/−0.69 (±0.09)	0.29 (±0.65)/−0.29 (±0.09)
sRMSE/tRMSE	0.8 (±0.51)/0.88 (±0.08)	0.51 (±0.5)/0.51 (±0.08)

tCor stayed the same for maximum temperature, daily precipitation accumulation and minimum relative humidity, but was higher for wind speed in CMIP6 BCSD relative to the CMIP6 Raw. Similar to the spatial statistics, maximum temperature's tBias was the only metric that was not lower in the CMIP6 BCSD.

In addition to the statistical metrics, a monthly climatology of each variable was generated for the CMIP6 Raw, CMIP6 BCSD, and the observational ensemble (Figure 23). BCSD successfully shifted the summertime temperatures downwards towards the observations, however, temperatures were slightly overestimated in the winter months (Figure 23a). Both the CMIP6 Raw and BCSD overestimated daily rainfall accumulation in the winter, however, the BCSD more closely approximated the observations throughout the year (Figure 23b).

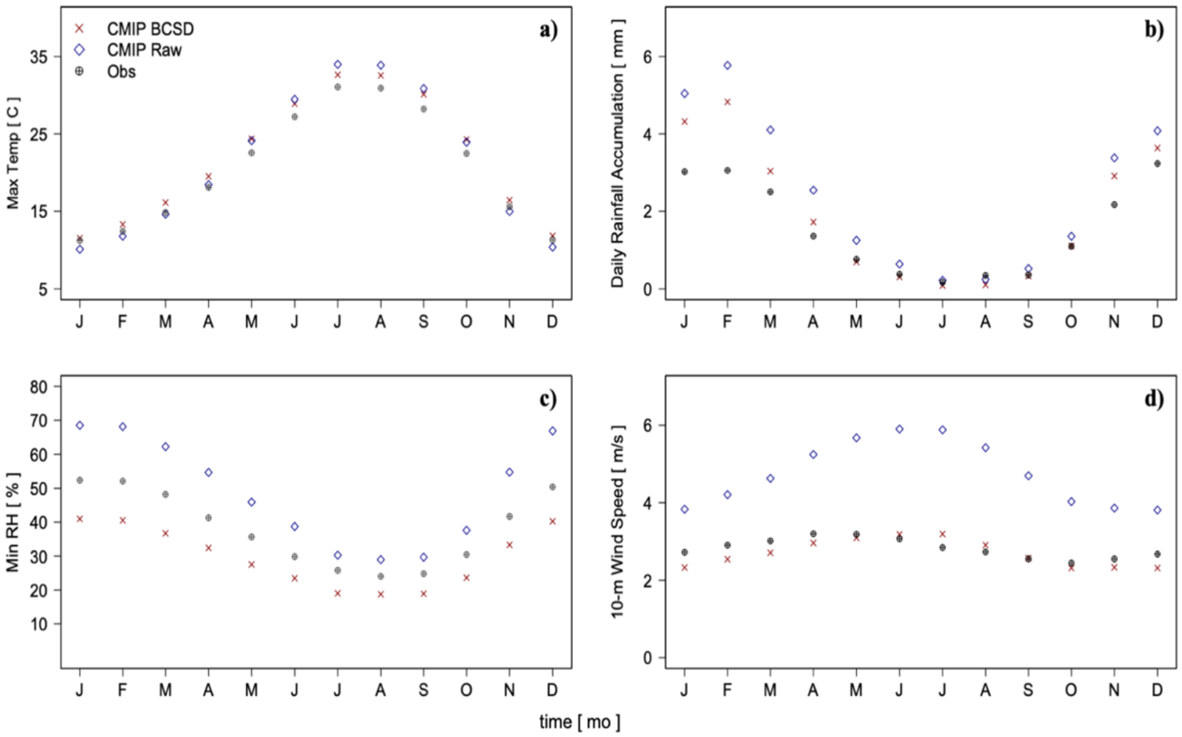

Figure 23. State-wide average monthly climatology (1979-2014) for the CMIP6 Raw and BCSD model ensembles. Observational data are an ensemble of NARR and TerraClimate. (a) Maximum temperature; (b) Daily Rainfall accumulation; (c) Minimum relative humidity; (d) 10-m wind speed.

The NARR minimum relative humidity fell between the CMIP6 Raw and BCSD monthly climatology, however, even though BCSD slightly underestimated winter relative humidity, the difference was smaller in all months than it was for CMIP6 Raw (Figure 23c). CMIP6 BCSD 10-m wind speed was very well simulated in California compared to CMIP6 Raw (Figure 23d).

4.3.2 Fire Weather Anomalies and Relative Change

FWI time series anomalies indicated increasing trends in both the mid- and late-century periods in all ecoregions, except the MWCM, which displayed a decrease in average FWI relative to the historical period (Figure 24). JJA relative change during the mid-century period ranged from −21.62 in the MWCM to 19.41 in the Central Valley, while late-century change ranged from −20.9 in the MWCM to 21.88 in the Central Valley. Furthermore, mid-century SON relative change ranged from −7.73 in the MWCM to 21.69 in the Cascades, and −8.23 in the MWCM to 25.44 in the Cascades during the late-century period.

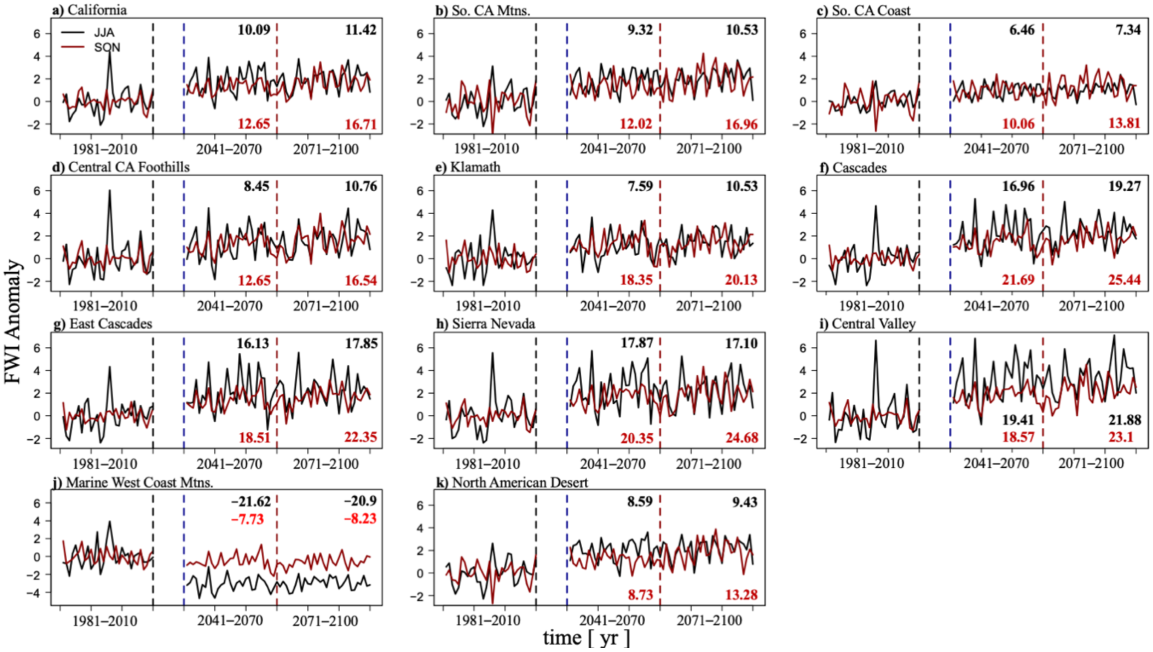

Figure 24. Canadian Fire Weather Index anomaly relative to the historical period of 1981-2010. Solid black line represents the summer season of June, July, and August while the solid red line represents the fall season of September, October, November. The dashed vertical black line represents the end of the historical period, while the dashed vertical blue and red lines represent the breaks between the mid- and late-century periods, respectively. The black and red text within the figure is the relative change (%) for the mid- and late-century periods (relative to the historical period) in the JJA and SON seasons, respectively. (a) California; (b) Southern California Mountains; (c) Southern California Coast; (d) Central California Foothills; (e) Klamath; (f) Cascades; (g) East Cascades; (h) Sierra Nevada; (i) Central Valley; (j) Marine West Coast Mountains; (k) North American Desert.

Overall, JJA and SON anomalies showed increasing average FWI between 2041-2100 (except MWCM), however, relative change during the SON season was greater than JJA in all ecoregions except the Central Valley during the mid-century period. FWI in the MWCM decreased relative to the historical baseline in both seasons, however, decreases during the SON were of much smaller magnitude, and are basically a continuation of historical conditions. In both the mid- and late-century periods, the central and northern California C, EC, SN, and Central Valley ecoregions experienced greater relative change in FWI compared to the southern California ecoregions SCC and SCM.

JJA and SON vapor pressure deficit increased relative to an historical baseline in all ecoregions during both the mid- and late-century time periods (Figure 25). Relative change of VPD during the fall was greater than in the summer in all ecoregions. JJA VPD during the mid-century period ranged from 14.96 in the SCC to 25.14 in the EC, and 22.08 in the SCC to 39 in the K during the late-century. On the other hand, mid-century SON vapor pressure deficit ranged from 15.68 in the SCC to 27.46 in the K, and from 26.16 in the SCC to 41.91 in the K ecoregion, during the late-century period.

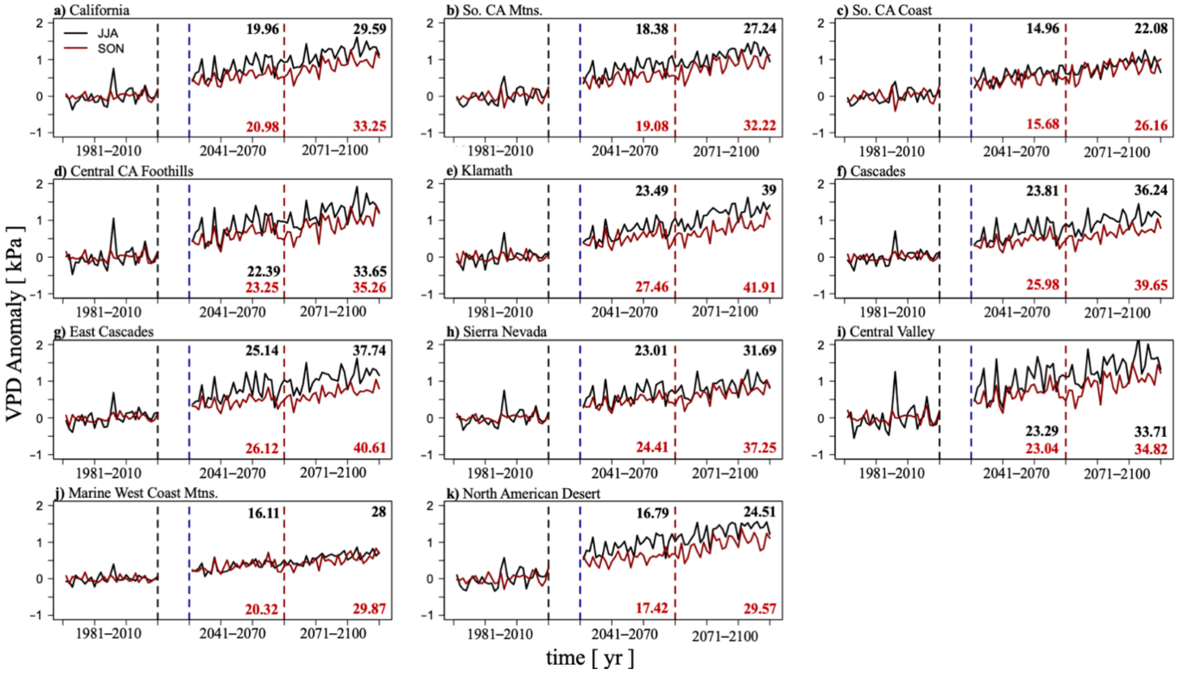

Figure 25. Vapor pressure deficit anomaly relative to the historical period of 1981-2010. Solid black line represents the summer season of June, July, and August while the solid red line represents the fall season of September, October, November. The dashed vertical black line represents the end of the historical period, while the dashed vertical blue and red lines represent the breaks between the mid- and late-century periods, respectively. The black and red text within the figure is the relative change (%) for the mid- and late-century periods (relative to the historical period) in the JJA and SON

seasons, respectively. (a) California; (b) Southern California Mountains; (c) Southern California Coast; (d) Central California Foothills; (e) Klamath; (f) Cascades; (g) East Cascades; (h) Sierra Nevada; (i) Central Valley; (j) Marine West Coast Mountains; (k) North American Desert.

Similar to FWI, JJA and SON relative change in VPD in the mid- and late-century periods increased more in the central and northern California ecoregions of the K, C, EC, SN, and Central Valley compared to the southern California ecoregions SCC and SCM (Figure 25). While FWI decreased in the MWCM ecoregion relative to its historical baseline (Figure 24j), VPD increased in both the mid- and late-century periods (Figure 25j). Differences between JJA and SON seasonal changes in VPD were greater than for FWI, however lower average historical values during SON led to comparable relative change (to the JJA season) in the mid- and late-century periods. Overall, both JJA and SON vapor pressure deficit is expected to increase linearly throughout 2041-2100, in all ecoregions.

4.3.3 95th Percentile Exceedance Maps

To further investigate the impact of climate change on extreme fire weather, we calculated the number of days that FWI and VPD were greater than or equal to the 95th percentile (calculated using a time series of daily average values for each ecoregion, not per pixel) (Figure 26). On average, JJA VPD_{95} increased substantially in all ecoregions in both the mid- and late-century periods (Table 10).

Table 10. Ecoregion average number of VPD_{95} and FWI_{95} days per year in each time period.

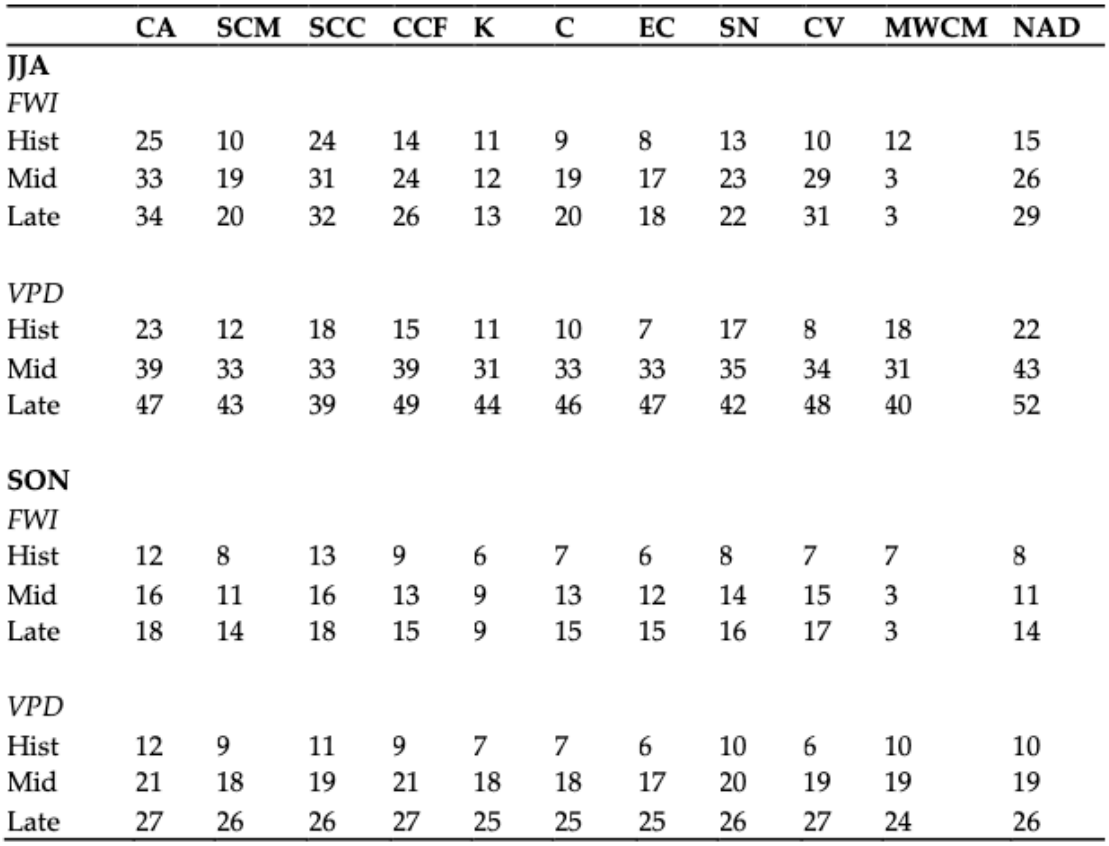

	CA	SCM	SCC	CCF	K	C	EC	SN	CV	MWCM	NAD
JJA											
FWI											
Hist	25	10	24	14	11	9	8	13	10	12	15
Mid	33	19	31	24	12	19	17	23	29	3	26
Late	34	20	32	26	13	20	18	22	31	3	29
VPD											
Hist	23	12	18	15	11	10	7	17	8	18	22
Mid	39	33	33	39	31	33	33	35	34	31	43
Late	47	43	39	49	44	46	47	42	48	40	52
SON											
FWI											
Hist	12	8	13	9	6	7	6	8	7	7	8
Mid	16	11	16	13	9	13	12	14	15	3	11
Late	18	14	18	15	9	15	15	16	17	3	14
VPD											
Hist	12	9	11	9	7	7	6	10	6	10	10
Mid	21	18	19	21	18	18	17	20	19	19	19
Late	27	26	26	27	25	25	25	26	27	24	26

The average number of days per year with VPD greater than the 95th percentile doubled in all ecoregions by 2100. In fact, from 2071-2100, over half the total number of summer days in the CCF, C, EC, CV, and NAD ecoregions had a VPD greater than the historical 95th percentile.

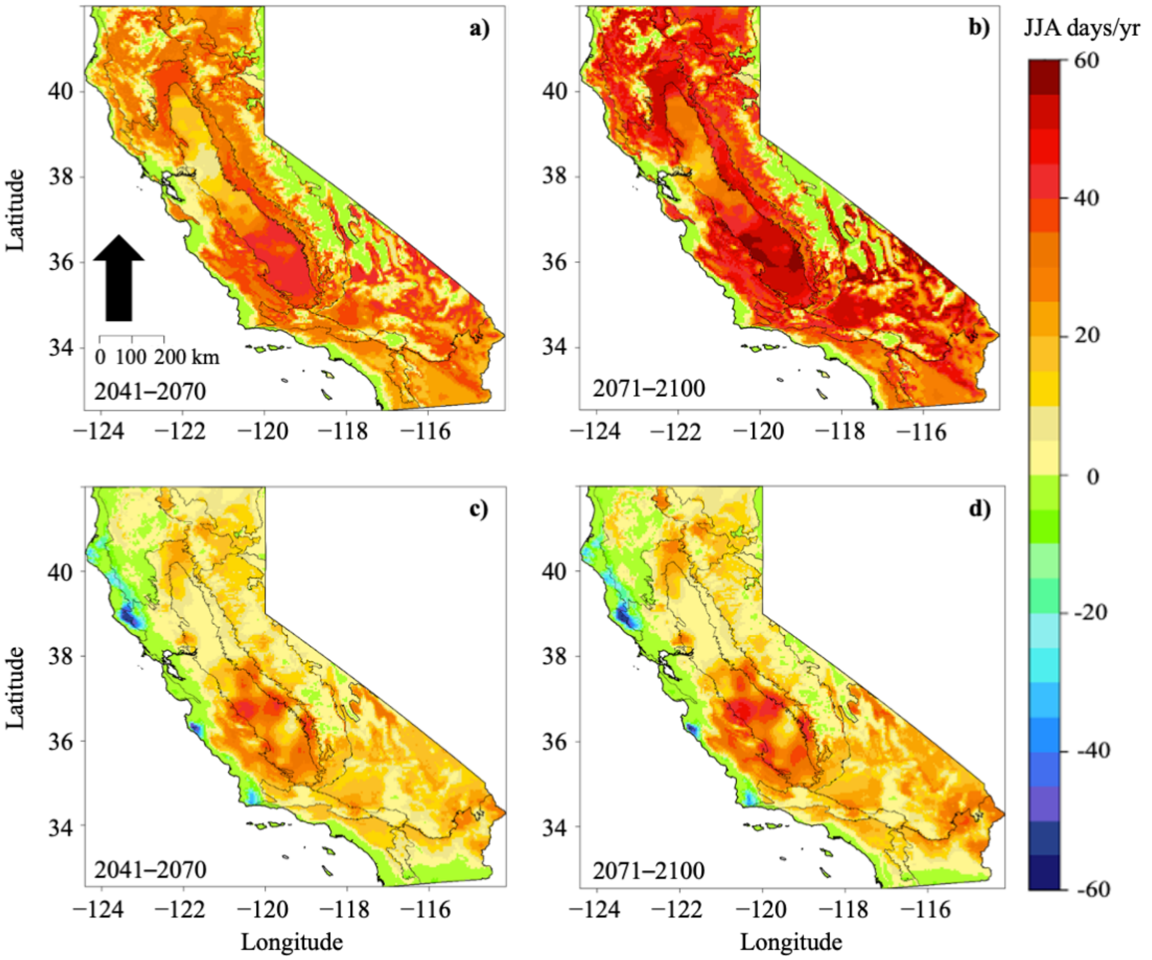

Figure 26. Average frequency (in days/yr) with which VPD and FWI exceed the ecoregion specific daily average JJA 95th percentile in the mid-century (left) and late-century (right) relative to the historic period. Higher values indicate more JJA days each year that exceeded the 95th percentile. (a,b) Vapor pressure deficit (c,d) Fire Weather Index.

The largest increases in VPD_{95} days occurred in the desert southwest region of California, particularly in the late-century period, where some areas are expected to experience historical VPD_{95} on nearly two-thirds of all summer days. Other areas expected to experience large increases in VPD_{95} days are the SCC ecoregion east of Los Angeles (34°N, 117°W), the southern portion of the Central Valley and the Central California Foothills, the western border of the Sierra Nevada, and scattered areas of the northern California Klamath, Cascades, and Eastern Cascades regions (Figure 26a-c).

JJA FWI_{95} days increased in both the mid- and late-century in all ecoregions except the MWCM, which experienced an average decrease in FWI_{95} days (Table 10). While the increase in average number of days with FWI_{95} is smaller than that of VPD_{95}, the SCM, C, EC, and CV double the number of FWI_{95} days by 2100. In addition, the greatest magnitude of change of FWI_{95} days occurred between the historical and the mid-century periods; the total change between the mid- and late-century was much smaller (Table 10). The most substantial increases in FWI_{95} days occurred in the desert southwest, the CV, the southern tip of the SN, the CCF, and the C and EC in northern California. However, there was a clear pattern of decreased numbers of FWI_{95} and VPD_{95} days (particularly FWI) in the mid- and late-century periods along the coast of California where the ocean moderates temperature. Furthermore, there was an apparent influence of topography in northern California (K, C, SN ecoregions), where high elevation areas showed little or even negative change, while, for example, the lower elevation, western slopes of the Sierra Nevada showed pronounced positive change. The dramatic increase in VPD_{95} and FWI_{95} days in the NAD ecoregion is an important climatic signal for human health and well-being, as well as for agriculture, but these increases are not likely to translate into increases in annual area burned because of a near total lack of continuous and flammable vegetation.

Historical 95th percentile thresholds were also calculated for each ecoregion for the SON season. The average number of VPD_{95} days increased in all ecoregions (Table 10). In fact, the average number of VPD_{95} days tripled by the end of the late-century period in the CCF, K, C, EC, and CV ecoregions, and doubled in the SCC, SN, MWCM, and NAD ecoregions (relative to the historical period). The average number of VPD_{95} days in the late-century period was substantially lower than it was in JJA, however, these results still imply that VPD is expected to increase dramatically for the entire duration of the summer and fall in all ecoregions (Table 10). Increases in the number of SON VPD_{95} days occurred in many of the same areas as JJA, including the NAD, the western and lower elevation portions of the Sierra Nevada, the southern region of the Central Valley, the Southern California Coast, and Central Foothills, as well as large portions of northern California's ecoregions, including Klamath, Cascades, and Eastern Cascades (Figures 27a-c).

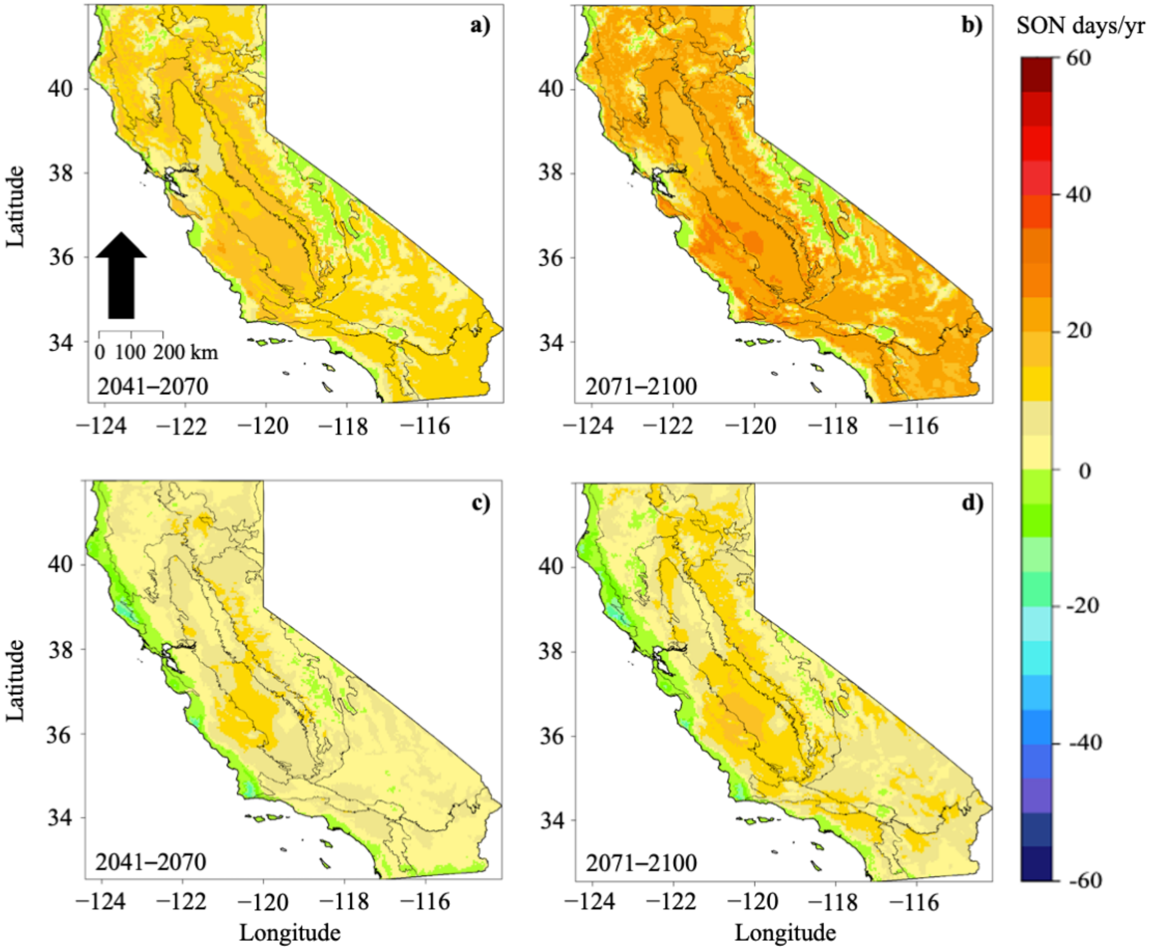

Figure 27. Average frequency (in days/yr) with which VPD and FWI exceed the ecoregion specific daily average SON 95th percentile in the mid-century (left) and late-century (right) relative to the historic period. Higher values indicate more SON days that exceeded the 95th percentile. (a,b) Vapor pressure deficit (c,d) Fire Weather Index.

SON FWI_{95} days increased in all ecoregions except the MWCM, which decreased from an average of 7 days/yr between 1981-2010 to 3 days/yr between 2071-2100 (Table 10). The

C, EC, and CV ecoregions doubled in the number of days experiencing FWI values greater than the historical 95th percentile. Overall changes in the occurrence of FWI_{95} days were smaller for the SON season compared to JJA, however, many of the same areas that were impacted in the summer show continued increases in extreme fire weather carrying into the fall, relative to the fall historical 95th percentile (Figure 27f). Some of the most affected areas include the region east of Los Angeles (34°N, 117°W), the south western region of the CCF (35-36°N, 120-121°W), western border of the Sierra Nevada, and the northern California Cascades and Eastern Cascades (Figure 27). Similar to the summer season, there was a moderating influence on FWI along the coast of California, as well as a topographic influence in the K and SN ecoregions. In fact, nearly the entire state of California, apart from the coastal and high elevation areas, displayed a positive signal in VPD_{95} by the end of the 21st century.

4.3.4 Fire Weather Frequency Distributions

The 30-year spatial averages of FWI and VPD were calculated for each of the 10 ecoregions during the historical, mid- and late-century periods. The frequency with which each FWI and VPD value occurred was plotted (as an area), along with the ecoregion specific 95th percentile value and the area that exceeded the threshold value in the three time periods (Figure 28).

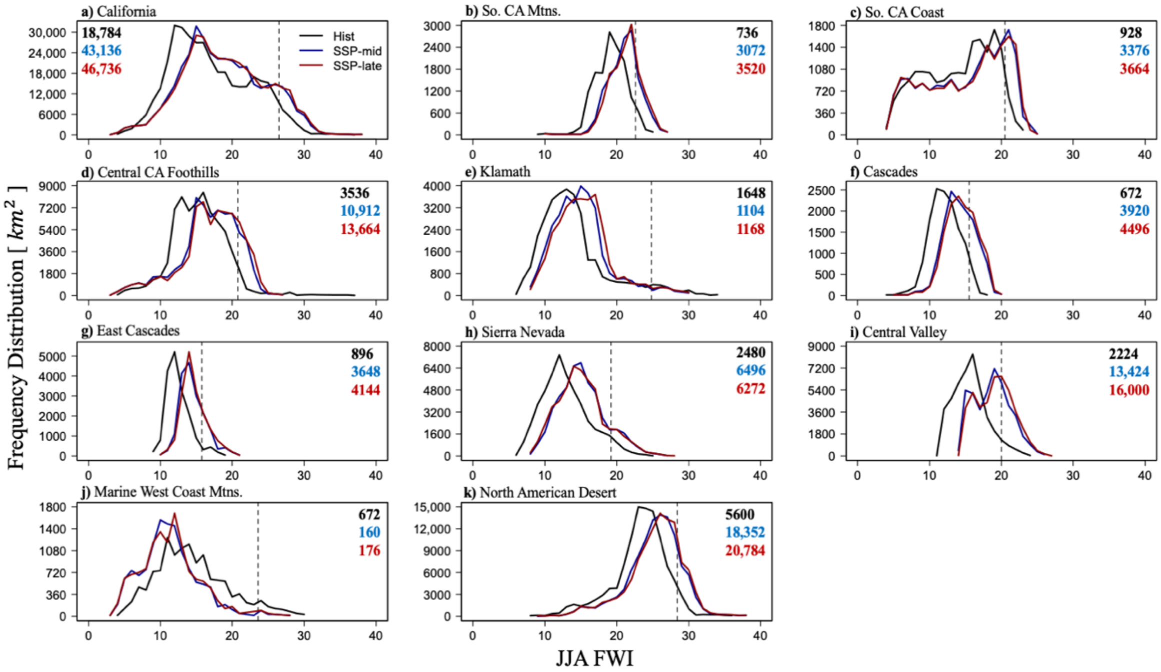

Figure 28. Frequency distributions depicting the area experiencing particular JJA FWI values. The dashed line represents the ecoregion specific 30-year average spatial 95th percentile value. The black, blue and red lines represent the historical, mid-century, and late-century time periods, respectively. The color-coded text are areal units (km^2) experiencing greater than the 95th percentile value for that ecoregion. (a) California; (b) Southern California Mountains; (c) Southern California Coast; (d) Central California Foothills; (e) Klamath; (f) Cascades; (g) East Cascades; (h) Sierra Nevada; (i) Central Valley; (j) Marine West Coast Mountains; (k) North American Desert.

The total land area that was projected to experience FWI greater than the 95th percentile value increased in all ecoregions apart from Klamath and the Marine West Coast Mountains (Figures 28e, j). The largest increases in area occurred in the Central Valley and the Cascades ecoregions (over seven and six times the historical area, respectively). Furthermore, the increase in area experiencing extreme fire weather in the SCM and the EC, followed by the SCC, CCF, and NAD ecoregions, increased by a factor of four and three, respectively. In many cases, including in the SCM, K, C, EC, SN, CV, and NAD ecoregions, the distribution of average FWI values shifted towards the 95th percentile threshold, indicating that mid- and late-century average FWI values could be closer to what is now considered extreme. The JJA

FWI_{95} percentile values ranged from 15.5 in the Cascades to 28.4 in the North American Desert, while the state-wide California JJA FWI_{95} was 26.5.

The increase in the amount of land area likely to experience FWI greater than the historical 95th percentile was even greater for SON than JJA, however, the MWCM ecoregion is projected to have a decline in the total land area with extreme fire weather (Table 11). The ecoregions projected to see the largest changes include the Central Valley, Cascades, and SCM, with ten, eight, and seven times the area under 95th percentile FWI by late-century, relative to the historical period. In addition, the NAD, EC, and SCC ecoregions increased by a factor of six, and the SN by a factor of five. Whereas the area within the Klamath ecoregion with FWI greater than the 95th percentile decreased in the summer, FWI_{95} area is projected to double in SON by the end of the 21st century. Additionally, the SON FWI_{95} percentile values ranged from 8.71 in the Cascades to 16.6 in the North American Desert, while the state-wide California SON FWI_{95} is 15.4.

Table 11. The extent of each ecoregion experiencing SON FWI and VPD greater than the 95th percentile. Calculated from the ecoregion 30-year average. Units: km^2.

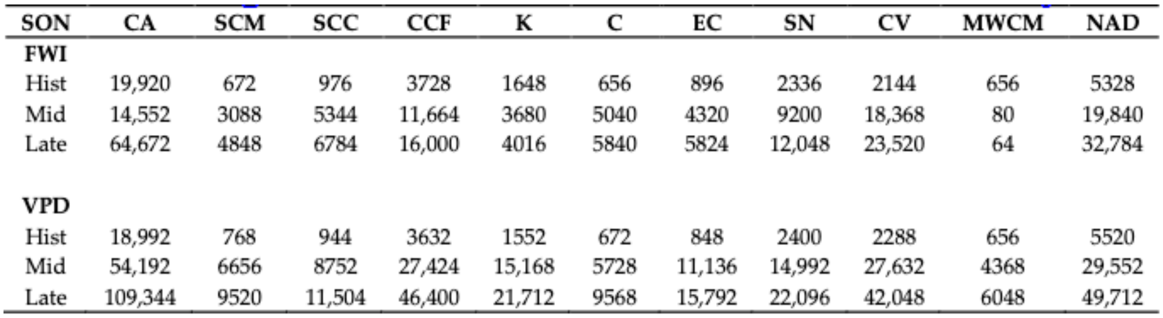

SON	CA	SCM	SCC	CCF	K	C	EC	SN	CV	MWCM	NAD
FWI											
Hist	19,920	672	976	3728	1648	656	896	2336	2144	656	5328
Mid	14,552	3088	5344	11,664	3680	5040	4320	9200	18,368	80	19,840
Late	64,672	4848	6784	16,000	4016	5840	5824	12,048	23,520	64	32,784
VPD											
Hist	18,992	768	944	3632	1552	672	848	2400	2288	656	5520
Mid	54,192	6656	8752	27,424	15,168	5728	11,136	14,992	27,632	4368	29,552
Late	109,344	9520	11,504	46,400	21,712	9568	15,792	22,096	42,048	6048	49,712

Ecoregion increases in JJA VPD_{95} area were even more substantial than FWI_{95} (Figure 29). The increase in VPD is so significant that the distribution of JJA VPD values shifts in a way that the peak VPD value in the mid- and late-century will exceed that of the historical 95th percentile threshold (Figures 29b-d, f, g, i, k). The largest increases in area exceeding

VPD_{95} occurred in the Central Valley and East Cascades, with a 17-fold increase, followed by the Cascades (13-fold), and the CCF and SCC (12-fold). The JJA VPD_{95} percentile values ranged from 3.12 in the MWCM to 6.98 in the North American Desert, while the state-wide California JJA VPD_{95} was 6.6.

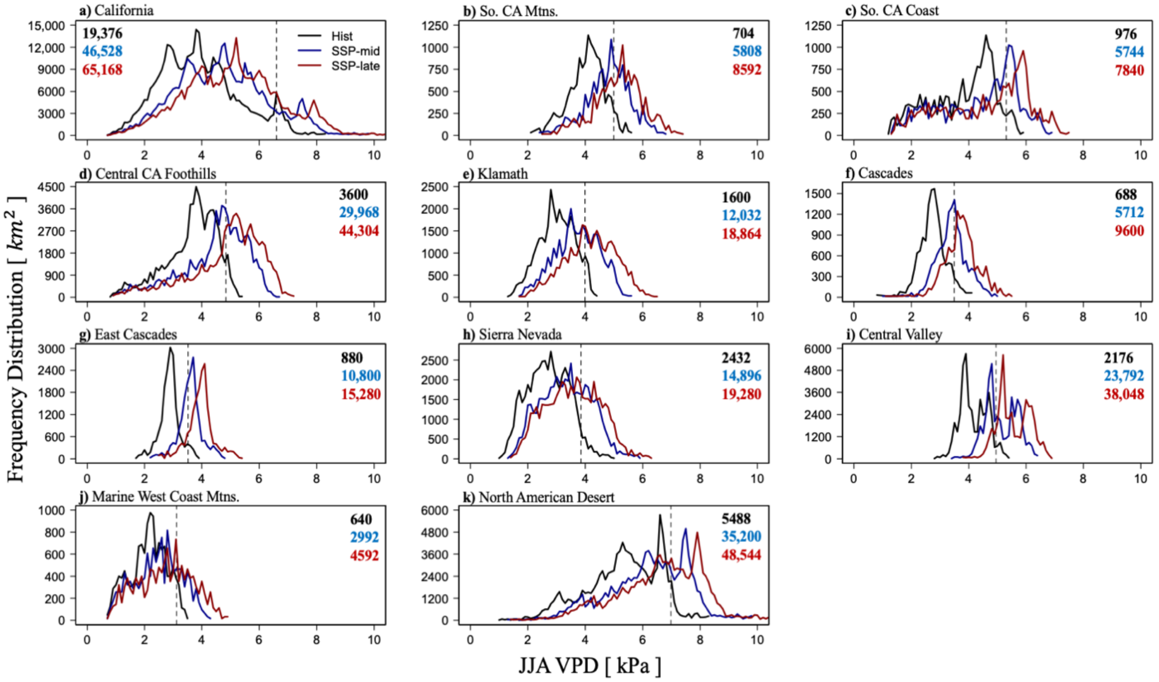

Figure 29. Frequency distribution depicting the area experiencing particular JJA VPD values. The dashed line represents the ecoregion specific 30-year average spatial 95th percentile value. The black, blue and red lines represent the historical, mid-century, and late-century time periods, respectively. The color-coded text are areal units (km^2) experiencing greater than the 95th percentile value for that ecoregion. (a) California; (b) Southern California Mountains; (c) Southern California Coast; (d) Central California Foothills; (e) Klamath; (f) Cascades; (g) East Cascades; (h) Sierra Nevada; (i) Central Valley; (j) Marine West Coast Mountains; (k) North American Desert.

The average projected area with extreme SON VPD was also large, implying that conditions in California will be conducive to wildfire for a minimum of half the year, extending the typical fire season into the fall, and contributing to the widespread desiccation of fuels. Unlike with patterns seen in the MWCM FWI values, VPD_{95} area was projected to increase in the MWCM in both the JJA and SON by a factor of seven and nine, respectively

(Figure 29j, Table 10). Additionally, the SON VPD_{95} percentile values ranged from 2.01 in the East Cascades to 4.28 in the North American Desert, while the state-wide California JJA VPD_{95} was 3.97.

4.3.5 Fire Weather Index Julian Day Climatologies

Climatologies ordered by Julian day of VPD indicated an increase in peak VPD in the summer, as well as an earlier start and a delayed end to the fire season in all ecoregions of California (Figure 30). For example, by 2100, the average onset of high spring VPD (defined here as VPD $\geq$ 3) is a month or more earlier in the SCC, CCF, K, C, SN ecoregions. Furthermore, the decrease of VPD below the critical value is delayed by a month or more in the C, EC and SN. Our results indicated that climate change will likely increase summer and autumn average VPD and lengthen the amount of time each year that conditions favor large wildfires in California (Figure 30).

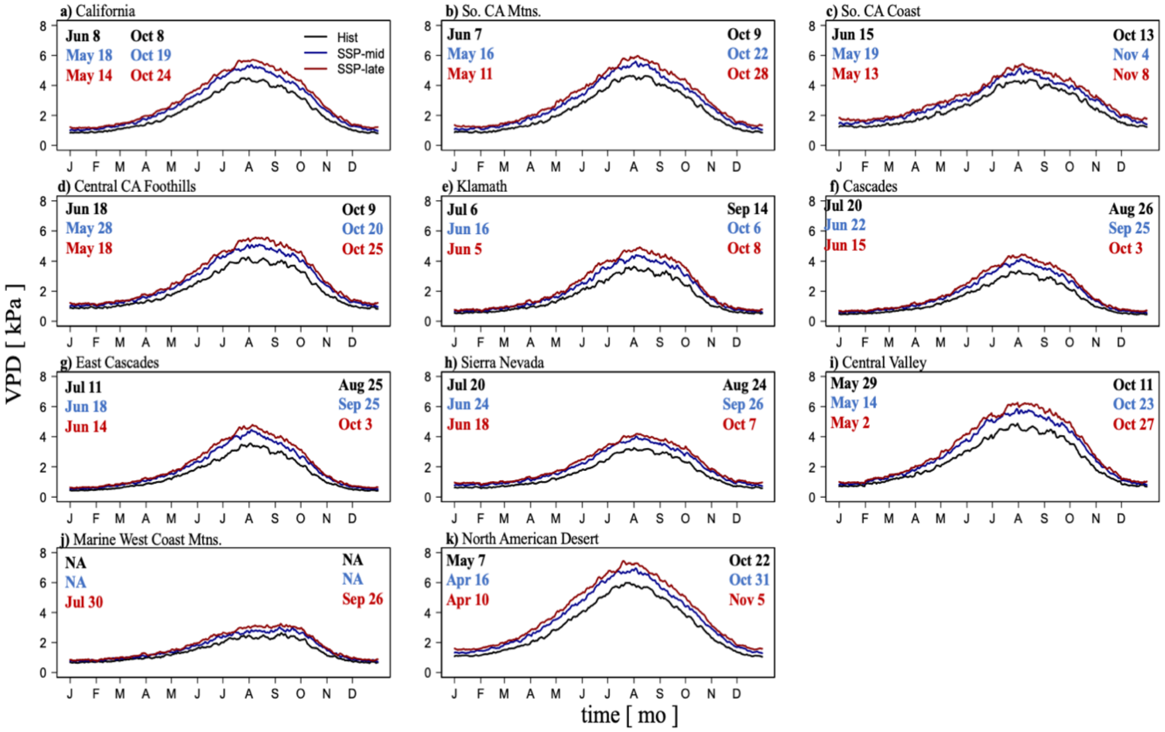

Figure 30. Thirty-year average Julian day VPD value by ecoregion. The black, blue, and red lines represent the historical, mid-century, and late-century averages, respectively. The color-coded text shows the average date for each respective time period that VPD exceeds (left) and falls below (right) a value of 3. (a) California; (b) Southern California Mountains; (c) Southern California Coast; (d) Central California Foothills; (e) Klamath; (f) Cascades; (g) East Cascades; (h) Sierra Nevada; (i) Central Valley; (j) Marine West Coast Mountains; (k) North American Desert. Units: kPa.

Climatologies ordered by Julian days of FWI indicated that the average summer peak FWI value will increase, and the fire season, defined here by the onset of average FWI greater than 15, will begin earlier and end later in the mid- and late-century periods relative to the historic period. However, the effect of climate change on the growth of the fire season was greater for VPD than it was for FWI (Figure 31). The greatest impact was to the onset of the fire season, with late-century average FWI exceeding a value of 15 anywhere from 6 days (SCC) to one month (NAD) before the historical average.

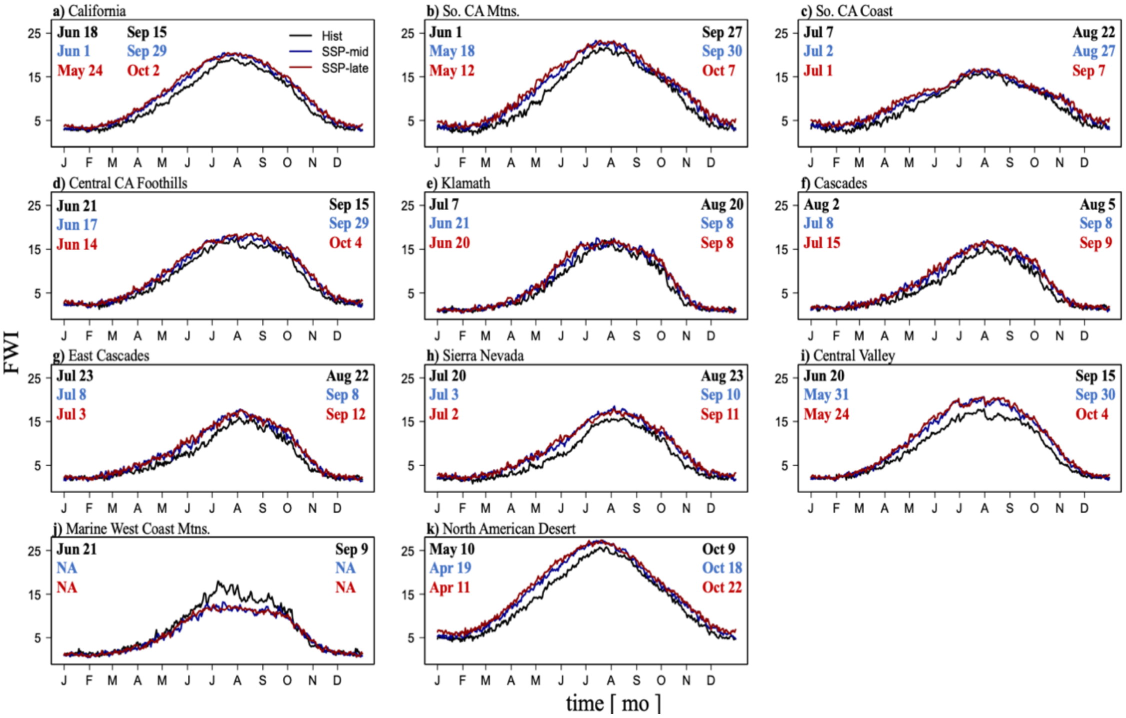

Figure 31. Thirty-year average Julian day Fire Weather Index value by ecoregion. The black, blue, and red lines represent the historical, mid-century, and late-century averages, respectively. The color-coded text shows the average date for each respective time period that FWI exceeds (left) and falls below (right) a value of 15. (a) California;

(b) Southern California Mountains; (c) Southern California Coast; (d) Central California Foothills; (e) Klamath; (f) Cascades; (g) East Cascades; (h) Sierra Nevada; (i) Central Valley; (j) Marine West Coast Mountains; (k) North American Desert.

Studies show that the role of temperature and humidity are strongest in FWI, with precipitation and wind speed playing important, but secondary roles (Dong et al. 2022; Jain et al. 2022). However, our results indicated that the increase of VPD in the mid- and late-century periods was much greater than FWI, especially in the MWCM, which experienced a decrease in summer FWI, implying that precipitation and wind patterns can play a strong role in FWI trajectory (Figure 31j). However, the sensitivity of the FWI to incremental changes in input variables is outside the scope of this study.

4.4 Discussion

4.4.1 Extreme Fire Weather in California's Future Will Become More Severe and Last Longer

California's fire weather season length has increased in the past three decades due to increases in surface air temperature, decreases in relative humidity, and longer annual rain-free periods (Jolly et al. 2015; Dong et al. 2022). Our results provide further evidence that fire weather conditions conducive to large wildfires will become more extreme and extend later into the fall season in most areas of California by 2100 (Goss et al. 2020; Dong et al. 2022). The peak effects of hot and dry summers will be extended by 30 days into late October and November. This timing will coincide with the Santa Ana wind season (which normally runs from October to March), as well as a projected delay in the onset of the rainy season—producing a high risk period during a time that has normally been outside of California's typical "fire season" for emergency preparedness (Swain 2021; Dong et al. 2022). The catastrophic consequences of severe fire weather towards the end of the typical California fire season were seen in 2020, with the August Complex Fire (August 2020), SCU Lightning Complex (August 2020), Creek (September 2020), LNU Lightning Complex (August 2020), and the North Complex (August 2020)—together accounting for five of the 10 largest wildfires in California history (Parks et al. 2014; CALFIRE 2022). In addition, the increase in land area experiencing extreme VPD and FWI expected by the end of the mid-century (2070) and late-century (2100) period, as well as the extension of the fire season late into the fall, will prime large portions of California for the spread of large wildfires, given an ignition (Figures 30 and 31).

4.4.2 Climate Change Impacts on California Ecoregions

Several conceptual frameworks exist that seek to determine the biophysical controls on wildfire ignition and probability of spread. For example, wildfire has been shown to thrive in the middle of a continuum between aridity (dry) and productivity (wet) (Bonan 2015). Similar to the way that plants have evolved traits that reflect biotic tradeoffs in favor of various survival strategies, wildfire regime is commonly controlled by the abundance and moisture content of fuels (Meyn et al. 2007; Archibald et al. 2013; Parks et al. 2016). For example, the tropics experience large amounts of rainfall, have high biomass production, and contain the necessary fuels for large wildfires—however, they are rarely dry enough to burn (Meyn et al. 2007; Parks et al. 2016). On the other hand, where moisture is limited and biomass production is low, wildfire does not have the necessary fuel to spread. Therefore, wildfire would be most likely to occur and spread in ecosystems that are dry for sufficient periods of time so that vegetation becomes water-stressed, but wet enough to support enough biomass that provide continuous fuels such that large wildfires may burn. These environmental gradients impact all aspects of fire regime, including fire frequency, occurrence, intensity, severity, and total area burned (Meyn et al. 2007; Bradstock 2010; Parks et al. 2016). This phenomenon implies that the projected impacts of climate change on temperature and atmospheric aridity will have a more significant effect on northern California forested ecoregions sensitive to extended dry periods than on the more consistently hot and dry southern California regions that are adapted to such conditions, and are more likely to lack the necessary abundance and continuity of fuel for large wildfires (McKenzie and Littell 2017). These climate-fire relationships are critical for the interpretation of our results, as the most substantial changes to the amount of area experiencing extreme fire weather (Figures 28 and 29), as well as the time added to the onset and end of the fire season (Figures 30 and 31), are projected to occur in forested northern California, where they could have the most dire implications for annual area burned throughout the 21st century.

In southern California, a large variety of topographies, vegetation types, climate regimes, and human populations contribute to a fire regime dominated by frequent wildfires. The precipitation season is confined to a few core months (Dec.-Mar.) with some rain occurring in the shoulder season of November and April, which in combination with the warm and dry summers, leads to an extended annual fire season (Jolly et al. 2015). In addition, annual Santa Ana winds advected from the eastern deserts towards the coast, move downslope at high speeds and increase the risk of severe wildfire during the fall season. Vegetation types are predominately herbaceous plants (chaparral), grasslands, shrubs, and patches of forest that recover relatively quickly following wildfire. The rapid re-generation of herbaceous fuels after wildfire are a factor in the frequent fire return interval throughout southern California (1-5 years) (Meng et al. 2014). Studies show that the impacts of climate change on fire regime in southern California thus far are primarily a result of increasing temperatures and atmospheric aridity, as well as changing patterns of precipitation, that in turn influence the state of the environmental constraints on wildfire activity discussed above (Krawchuk et al. 2011). Compared to forested regions of northern California, fire regime in non-forested regions of southern California are less susceptible to shifts in moisture availability and more so to availability of fuel, however, these chaparral and grassland ecosystems are sensitive to rainfall patterns in the year or two prior to fire occurrence because the influx of moisture promotes the growth of vegetation (Keeley and Syphard 2019; Williams et al. 2019). Our results indicate that while the increases in land area experiencing extreme fire weather are smaller than in northern California, and the extension of the fire season is not as substantial, changes to southern California JJA and SON extreme fire weather, in succession, still have the potential to tax vegetation-management and fire-fighting resources.

Conceptual frameworks help to attribute controlling factors to different fire regimes, given the complex web of climate, human activity, topography, vegetation, hydrology, prior wildfire, fire suppression, and fire management, with their practically infinite combination. Our ecoregion specific results show a future consisting of more persistent extreme fire weather that occurs in a greater land surface area than in the past. Therefore, with the aid of climate-fire frameworks, we may deduce the range of impacts that this increase in aridity and fire potential may have on sensitive ecosystems. While northern and southern California ecoregion’s fire regimes are controlled by different factors, the simultaneous increasing trends in atmospheric aridity and fire potential indicate a future in which fire suppression and management resources throughout the state are stretched thin. In order to offset the dangers of extended fire seasons throughout much of California by 2100, alongside the expansion of the wildland urban interface, fire management must implement innovative combinations of new and existing strategies intended to limit the destruction of property and loss of life.

4.4.3 Limitations

Impact studies that utilize global climate model output generally require the use of many models, however, due to the recent release of CMIP6, limited availability of the fire weather variables required to perform the FWI and VPD calculations restricted our ability to increase the number of models used (Araya-Ossess et al. 2020). Despite this, the evaluation of the ensemble-mean of the three models chosen for this study showed good agreement with observational data. In addition, we acknowledge that all statistical downscaling methods are subject to issues of stationarity. To be clear, there are assumptions made regarding the application of historical climatic patterns to projected data, however, the thin plate spline and linear regression method employed here advantageously utilizes data surrounding each grid point in the calculation of its smoothed estimate. This interpolation technique works best with continuous data but it may be adapted to perform well with discontinuous climate variables such as precipitation, and to some extent wind speed. Additionally, it is important to consider the climate-wildfire-vegetation feedback when attempting to predict annual area burned, however, this work focuses on the impacts of climate on extreme fire weather, so the complex relationships among annual area burned, climate patterns, and vegetation distribution are outside the scope of this study (Hurteau et al. 2019). Lastly, it should be noted that projected increases in California’s summer and fall VPD and FWI are not synonymous with a corresponding increase in annual area burned, as wildfire is inherently dependent on an ignition source and flammable vegetation (Keeley and Syphard 2016).

4.5 Conclusions

We analyzed the impacts of climate change on extreme fire weather in ten different California ecoregions throughout historical, mid- and late-century periods using two prominent fire weather indices. Climate model output from three CMIP6 models were bias corrected and statistically downscaled using empirical quantile mapping in addition to a simple thin plate spline interpolation method. Historical average baselines for each index were calculated for each ecoregion and used to generate anomalies for 2041-2100. Relative change analysis indicates that FWI and VPD are projected to increase in all ecoregions, except the MWCM, which displayed a decrease in JJA and SON FWI in the mid- and late-century periods. In addition, the average daily 95th percentile value for the historical period (for each ecoregion) was implemented as a threshold in order to calculate the number of summer and fall extreme fire weather days, and to evaluate the spatial distribution of these changes. The frequency of 95th percentile days for JJA and SON VPD and FWI is projected to increase significantly in all ecoregions, except the MWCM, which shows a decline in FWI 95th percentile days. Furthermore, we analyzed the 30-year spatial average of each index and generated frequency distributions to investigate the average change in land area projected to experience extreme fire weather, relative to the historical benchmark. We found that JJA VPD land area exceeding the 95th percentile will increase by a factor of 2 and 17 in different ecoregions by the end of 2100. Lastly, Julian-day climatologies of each index were generated to assess the changing duration of a typical California fire season. We found that the window of extreme fire weather will expand into the spring and late autumn in all ecoregions (apart from the MWCM), extending the amount of time vegetation is exposed to increased atmospheric demand for moisture, and heightening the overall risk for the ignition and spread of large wildfire.

The ecoregion-level spatial scale adopted for this study increases the amount of local information, as well as the resolution with which fire and land managers can implement strategies and counter-measures when addressing issues related to climate change. The spatial downscaling algorithm tested and implemented in this study was computationally inexpensive (compared to dynamical downscaling) and may be readily applied to further climate change scenarios in other Mediterranean and temperate regions (Abatzoglou and Brown 2012; Zhang et al. 2020). High resolution, daily meteorological data is not only useful for wildfire impact studies (and for investigating the post-fire environment), but can be implemented in the research of agricultural productivity, urban heat islands, hydrology, and human health. This intuitive, practical, and simple interpolation method will not only contribute to the improved understanding of the complexities of California’s climate-fire dynamics, but will provide the means for more efficiently obtaining climate model data of high spatial and temporal resolution.

Chapter 5. Conclusions

5.1 Summary of Results

The objectives of this dissertation research were to (1) investigate the impacts of wildfire on the surface energy balance in California; (2) assess the influence of wildfire burn severity on the five-year postfire recovery trajectory of three biophysical variables, including vegetation abundance, land surface temperature, and surface shortwave albedo; and (3) quantify and evaluate the impacts of climate change on the occurrence of extreme fire weather during an historical (1979-2014), mid-century (2041-2070), and a late-century (2071-2100) period. These objectives were met using a variety of research tools, methodologies, and techniques, along with a suite of climatological and remote sensing datasets. Each chapter provides a unique perspective on the bi-directional climate-wildfire feedback system, in which wildfire both drives, and responds to, meteorological changes. For example, the removal of vegetation and the deposition of ash following a large wildfire may lead to a decrease in evapotranspiration and an increase in land surface temperatures for more than five years after ignition. The suppression of latent heat flux after wildfires of sufficient size and severity may even impact precipitation patterns. On the other hand, climatic changes throughout the 21st century, such as increases in temperature and aridity, may lead to an increased occurrence of extreme fire weather.

The research presented in Chapter 2 investigated the impact of wildfire on surface energy exchange through the assessment of six California wildfires that occurred since 2003. A burned-unburned binary mask was generated from monthly date-of-burn product and implemented into a land surface model for a series of simulations. Simulations show a decrease in latent heat flux in every case study except the Rush fire, which occurred in Lassen county in August 2012. Post-fire changes in net radiation and sensible heat followed similar trends, decreasing in each of the domains except the Rush and Cedar fires - which was likely caused by the increase in sensible heat flux from ash deposition dominating over the decrease in latent heat flux from vegetation removal. Initial increases in sensible heat flux, caused by the decrease in albedo from ash deposition, are balanced by decreases in latent heat flux in the Zaca, Rim, and Basin Complex case studies. Overall, the largest changes to net radiation were primarily caused by decreases in latent heat flux following wildfire-induced vegetation removal.

The vegetation recovery and surface albedo change components of Chapter 2 were developed in Chapter 3 through a more comprehensive investigation into the temporal patterns of biophysical change following wildfires of varying degrees of severity. In this study, a collection of MODIS datasets was used to investigate the impact of burn severity on vegetation recovery, albedo change, and land surface temperature in seven California ecoregions. A statewide MODIS-derived RdNBR dataset was generated using surface reflectance data and used to analyze the impact of burn severity on the five-year postfire early-summer averages of each biophysical variable between the years 2003-2020. The highest prefire EVI and the greatest decrease of EVI after one year, regardless of burn severity, were found in the Klamath, Cascades, and the Sierra Nevada ecoregions. High severity fire was associated with the largest decreases in EVI one year later, and EVI did not recover to prefire levels after 5 years in any burn severity class in any ecoregion. Also, EVI recovered most rapidly during the first 2 years postfire after high severity fires. Furthermore, LST increased in the first year postfire in all ecoregions regardless of burn severity, and the greatest increases in LST were associated with high severity fires. Similar to EVI, postfire LST did not return to prefire levels after five years in any burn severity class.

In Chapter 4, a bias correction and statistical downscaling technique was implemented to obtain high-resolution, daily meteorological conditions for input into two fire weather indices: vapor pressure deficit and the Canadian Fire Weather Index System. The results from Chapter 4 provide evidence that fire weather conditions will become more extreme and extend into the spring and fall seasons in most areas of California by 2100, extending the amount of time vegetation is exposed to increased atmospheric demand for moisture, and heightening the overall risk for the ignition and spread of large wildfires.

5.2 Key Contributions and Findings

The studies that comprise this dissertation contribute to the literature by detailing a land surface modeling technique that allows for the simulation of wildfire-induced vegetation removal, applicable anywhere in the world. Also, a computationally inexpensive bias correction and statistical downscaling technique is explained that may allow researchers to obtain high-resolution meteorological data, which may be useful for wildfire impact assessments, as well as in research areas such as agricultural productivity, urban heat islands, hydrology, and human health. Further, the biophysical response to wildfires of varying degrees of severity provide critical indications of ecosystem health and can inform fire and land management in their efforts to effectively mitigate and suppress large wildfires in key areas. Also, the quantification of postfire change in albedo and land surface temperature may improve the accuracy and inform the conceptualization of future modeling of wildfire impacts.

References

Abatzoglou JT, Brown TJ (2012) A comparison of statistical downscaling methods suited for wildfire applications: Statistical downscaling for wildfire applications. Int J Clim 32: 772–780. https://doi.org/10.1002/joc.2312.

Abatzoglou JT (2013) Development of gridded surface meteorological data for ecological applications and modelling. Int J Climatol 33: 121–131.

Abatzoglou JT, Kolden CA (2013) Relationships between climate and macroscale area burned in the western United States. Int J Wildland Fire 22(7): 1003–1020. https://doi.org/10.1071/WF13019

Abatzoglou JT, Williams AP (2016) Impact of anthropogenic climate change on wildfire across western US forests. Proc Natl Acad Sci USA 113: 11770–11775. https://doi.org/10.1073/PNAS.1607171113.

Abatzoglou JT, Kolden CA, Williams AP, Lutz JA, Smith AMA (2017) Climatic influences on interannual variability in regional burn severity across western US forests. Int J Wildland Fire 26(4): 269. doi:10.1071/wfl6165

Abatzoglou JT, Dobrowski SZ, Parks SA, Hegewisch KC (2018) Terraclimate, a high-resolution global dataset of monthly climate and climatic water balance from 1958–2015. Sci Data 5: 170191. https://doi.org/10.1038/sdata.2017.191.

Amiro B, Orchansky A, Barr A, Black T, Chambers S, Chapin F, et al. (2006) The effect of post-fire stand age on the boreal forest energy balance. Agric For Meteorol 140: 41–50.

André JC, Bougeault P, Mahfouf JF, Mascart P, Noilhan J, Pinty JP (1989) Impact of forests on mesoscale meteorology. Philos Trans R Soc 324: 407–422

Anthes RA (1984) Enhancement of convective precipitation by mesoscale variations in vegetative covering in semiarid regions. J Clim Appl Meteorol 23(4): 541–554. https://doi.org/10.1175/1520-0450(1984)023<0541:EOCPBM>2.0.CO;2

Araya-Osses D, Casanueva A, Román-Figueroa C, Uribe J.M, Paneque M (2020) Climate change projections of temperature and precipitation in Chile based on statistical downscaling. Clim Dyn 54: 4309–4330. https://doi.org/10.1007/s00382-020-05231-4.

Archibald S, Lehmann CER, Gomez-Dans JL, Bradstock RA (2013) Defining pyromes and global syndromes of fire regimes. Proc Nat Acad Sci USA 110: 6442–6447. https://doi.org/10.1073/pnas.1211466110.

Arnold JD, Brewer SC, Dennison PE (2014) Modeling climate-fire connections within the great basin and upper Colorado River Basin, western United States. Fire Ecology 10(2): 64–75. https://doi.org/10.4996/fireecology.1002064

Barbero R, Abatzoglou JT, Larkin NK, Kolden CA, Stocks B. Climate change presents increased potential for very large fires in the contiguous United States. Int J Wildland Fire 24(7): 892. https://doi.org/10.1071/WF15083.

Bendix J, Commons MG (2017) Distribution and frequency of wildfire in California riparian ecosystems. Environ Res Lett 12(7): 075008. doi: 10.1088/1748-9326/aa7087

Beringer J, Chapin FS, Thompson CC, McGuire AD (2005) Surface energy exchanges along a tundra-forest transition and feedbacks to climate. Agric For Meteorol 131(3–4): 143–161. https://doi.org/10.1016/j.agrformet.2005.05.00

Bodí MB, Martin DA, Balfour VN, Santín C, Doerr SH, Pereira P, Cerdà A, Mataix-Solera J (2014) Wildland fire ash: Production, composition and eco-hydro-geomorphic effects. Earth-Science Reviews 130: 103–127. https://doi.org/10.1016/j.earscirev.2013.12.007

Bonan GB (2008) Forests and climate change: Forcings, feedbacks, and the climate benefits of forests. Science 320: 1444–1449. https://doi.org/10.1126/science.1155121.

Bonan G (2015) Ecological climatology: Concepts and applications; Cambridge University Press: Cambridge, UK. ISBN 978-1107619050.

Bradstock RA (2010) A biogeographic model of fire regimes in Australia: Current and future implications: A biogeographic model of fire in Australia. Glob Ecol Biogeogr 19: 145–158. https://doi.org/10.1111/j.1466-8238.2009.00512.x.

Bremer D, Ham J (1999) Effect of spring burning on the surface energy balance in a tallgrass prairie. Agric For Meteorol 97: 43–54. doi:10.1016/S0168-1923(99)00034-9.

Bright BC, Hudak AT, Kennedy RE, Braaten JD, Khalyani AH (2019) Examining post-fire vegetation recovery with Landsat time series analysis in three western North American forest types. Fire Ecol 15(8). https://doi.org/10.1186/s42408-018-0021-9.

CAL FIRE (2022) Top 20 Largest California Wildfires. Retrieved May 9, 2022, from https://www.fire.ca.gov/communications/downloads/fact_sheets/Top20_Acres.pdf

Chambers SD, Chapin FS (2003) Fire effects on surface-atmosphere energy exchange in Alaskan black spruce ecosystems: Implications for feedbacks to regional climate. J Geophys Res 108(D1). https://doi.org/10.1029/2001jd000530

Chambers SD, Beringer J, Randerson JT, Chapin IS (2005) Fire effects on net radiation and energy partitioning: Contrasting responses of tundra and boreal forest ecosystems. J Geophys Res Atmos 110(9): 1–9. https://doi.org/10.1029/2004JD005299

Collins BM, Roller GB (2013) Early Forest Dynamics in stand-replacing fire patches in the Northern Sierra Nevada, California, USA. Landsc Ecol 28(9): 1801–1813. https://doi.org/10.1007/s10980-013-9923-8.

Crotteau JS, Morgan Varner J, Ritchie MW (2013) Post-fire regeneration across a fire severity gradient in the Southern Cascades. For Ecol Manag 287: 103–112. https://doi.org/10.1016/j.foreco.2012.09.022.

Daly C, Taylor GH, Gibson WP (1997) The PRISM approach to mapping precipitation and temperature. In: Proc. 10th Conf. on Appl Climatol, Reno, NV, October 20-23. American Meteorology Society, p 10–12

Davis LR, Fishburn KA, Lestinsky H, Moore LR, Walter JL (2019) US Topo Product Standard (ver. 2.0, February 2019): U.S. Geological Survey Techniques and Methods book 11, chap. B2, 20 p., 3 plates, scales 1:24,000, 1:25000, and 1:20,000. https://doi.org/10.3133/tm11b2

De Sales F, Xue Y, Okin GS (2016) Impact of burned areas on the northern African seasonal climate from the perspective of regional modeling. Climate Dynamics 47(11): 3393–3413. https://doi.org/10.1007/s00382-015-2522-4

De Sales F, Okin GS, Xue Y, Dintwe K (2018) On the effects of wildfires on precipitation in southern Africa. Climate Dynamics 52: 951–967. https://doi.org/10.1007/s00382-018-4174-7

Dennison PE, Moritz MA, Taylor RS (2008) Evaluating predictive models of critical live fuel moisture in the Santa Monica Mountains, California. Int J Wildland Fire 18–27

Didan K (2015) MOD13A1 MODIS/Terra Vegetation Indices 16-Day L3 Global 500m SIN Grid V006. NASA EOSDIS Land Processes DAAC. https://doi.org/10.5067/MODIS/MOD13A1.006

Dintwe K, Okin GS, Xue Y (2017) Fire-induced albedo change and surface radiative forcing in sub-Saharan Africa savanna ecosystems: Implications for the energy balance. J Geophys Res 122(12): 6186–6201. https://doi.org/10.1002/2016JD026318

Dong L, Leung LR, Qian Y, Zou Y, Song F, Chen X (2021) Meteorological environments associated with California wildfires and their potential roles in wildfire changes during 1984–2017. J Geophys Res Atmos 126(5). https://doi.org/10.1029/2020JD033180.

Dong C, Williams AP, Abatzoglou JT, Lin K, Okin GS, Gillespie TW, Long D, Lin YH, Hall A, MacDonald GM (2022) The season for large fires in Southern California is projected to lengthen in a changing climate. Commun Earth Environ 3: 22. https://doi.org/10.1038/s43247-022-00344-6.

Fernandez-Manso A, Quintano C, Roberts DA (2016) Burn severity influence on post-fire vegetation cover resilience from Landsat MESMA fraction images time series in Mediterranean forest ecosystems. Remote Sens Environ 184: 112–123. https://doi.org/10.1016/j.rse.2016.06.015.

Flannigan MD, Krawchuk MA, de Groot WJ, Wotton BM, and Gowman LM (2009) Implications of changing climate for global wildland fire. Int J Wildland Fire 18, no. 5: 483. https://doi.org/10.1071/WF08187.

Flint LE, Underwood EC, Flint AL, Hollander AD (2019) Characterizing the influence of fire on hydrology in southern California. Natural Areas Journal 39(1): 108. https://doi.org/10.3375/043.039.0108

French NHF, Kasischke ES, Hall RJ, Murphy KA, Verbyla DL, Hoy EE, et al. (2008) Using Landsat data to assess fire and burn severity in the North American boreal forest region: An overview and summary of results. Int J Wildland Fire 17(4): 443. https://doi.org/10.1071/WF08007.

Friedl MA, McIver DK. Hodges JCF, Zhang XY, Muchoney D, Strahler AH, et al. (2002) Global land cover mapping from MODIS: Algorithms and early results, Remote Sens Environ 83(1–2): 287–302, doi:10.1016/S0034-4257(02)00078-0.

Friedl MA, Sulla-Menashe D, Tan B, Schneider A, Ramankutty N, Sibley A, Huang XM (2010) MODIS Collection 5 global land cover: Algorithm refinements and characterization of new datasets, Remote Sens Environ 114(1): 168–182, doi:10.1016/j.rse.2009.08.016.

Friedl, M., & Sulla-Menashe, D (2019) MCD12Q1 MODIS/Terra+Aqua land cover type yearly L3 Global 500m SIN Grid V006 [Data set]. NASA EOSDIS Land Processes DAAC. Accessed 2020-12-16 from https://doi.org/10.5067/MODIS/MCD12Q1.006

Fu G, Viney NR, Charles SP (2010) Evaluation of various root transformations of daily precipitation amounts fitted with a normal distribution for Australia. Theor Appl Climatol 99: 229–238. https://doi.org/10.1007/s00704-009-0137-6.

Gatebe C K, Ichoku CM, Poudyal R, Román MO, Wilcox E (2014) Surface albedo darkening from wildfires in northern sub-Saharan Africa. Environ Res Lett 9(6). https://doi.org/10.1088/1748-9326/9/6/065003

Giglio L, Justice C, Boschetti L, Roy D (2015) MCD64A1 MODIS/Terra+Aqua Burned Area Monthly L3 Global 500m SIN Grid V006. distributed by NASA EOSDIS Land

Processes DAAC, https://doi.org/10.5067/MODIS/MCD64A1.006. Accessed 2022-02-25.

Gitas IZ, de Santis A, Mitri GH (2009) Remote sensing of burn severity. In Earth Observation of wildland fires in Mediterranean ecosystems pp. 129-148. doi:10.1007/978-3-642-01754-4_10.

Goss M, Swain DL, Abatzoglou JT, Sarhadi A, Kolden CA, Williams AP, Diffenbaugh NS (2020) Climate change is increasing the likelihood of extreme autumn wildfire conditions across California. Environ Res Lett 15(9). https://doi.org/10.1088/1748-9326/ab83a7.

Govaerts YM, Pereira JM, Pinty B, Mota B (2002) Impact of fires on surface albedo dynamics over the African continent. J Geophys Res 107(D22): 4629. doi:10.1029/2002JD002388

Griffith GE, Omernik JM, Smith DW, Cook TD, Tallyn E, Moseley K, et al. (2016) Ecoregions of California (poster): U.S. Geological Survey Open-File Report 2016–1021, with map, scale 1:1,100,000. http://dx.doi.org/10.3133/ofr20161021.

Hancock PA, Hutchinson MF (2006) Spatial interpolation of large climate data sets using Bivariate Thin Plate Smoothing Splines. Environ Model Softw 21, 1684–1694. https://doi.org/10.1016/j.envsoft.2005.08.005.

Hansen MC, DeFries RS, Townshend JR, Sohlberg R (2000) Global land cover classification at 1 km spatial resolution using a classification tree approach. Int J Remote Sens 21: 1303–1330

Harris S, Veraverbeke S, Hook S (2011) Evaluating spectral indices for assessing fire severity in chaparral ecosystems (southern California) using MODIS/ASTER (MASTER) Airborne Simulator Data. Remote Sens 3(11): 2403–19. https://doi.org/10.3390/rs3112403.

Havel A, Tasdighi A, Arabi M (2018) Assessing the long-term hydrologic response to wildfires in mountainous regions. Hydrology and Earth System Sciences Discussions, 1–39

Hislop S, Jones S, Soto-Berelov M, Skidmore A, Haywood A, Nguyen TH (2018) Using Landsat spectral indices in time-series to assess wildfire disturbance and recovery. Remote Sens 10: 460. doi:10.3390/rs10030460.

Hoar T, Nychka D (2022) Statistical downscaling of the Community Climate System Model (CCSM) monthly temperature and precipitation projections [White Paper]. IMAGe/NCAR. Available online: http://www.gisclimatechange.org/Downscaling.pdf (accessed on 1 May 2022).

Hope A, Tague C, Clark R (2007) Characterizing post-fire vegetation recovery of California chaparral using TM/ETM+ time-series data. Int J Remote Sens 28: 1339–1354. https://doi.org/10.1080/ 01431160600908924.

Hostetler SW, Bartlein PJ, Alder JR (2018) Atmospheric and surface climate associated with 1986–2013 wildfires in North America. J Geophys Res Biogeosciences 123(5): 1588–1609. https://doi.org/10.1029/2017JG004195

Huang S, Dahal D, Liu H, Jin S, Young C, Li S, Liu S, Jin S (2015) Spatiotemporal variation of surface shortwave forcing from fire-induced albedo change in interior Alaska. Can J For Res 45(3): 276–285. https://doi.org/10.1139/cjfr-2014-0309

Hudak AT, Morgan P, Bobbitt MJ, Smith AMS, Lewis SA, Lentile LB, et al. (2007) The relationship of multispectral satellite imagery to immediate fire effects. Fire Ecol 3: 64–90.

Hulley G (2017) MYD21A2N MODIS/Aqua Land Surface Temperature/3-Band Emissivity 8-Day L3 Global 1km SIN Grid V006 [Data set]. NASA EOSDIS Land Processes DAAC. Accessed 2020-10-13 from https://doi.org/10.5067/MODIS/MYD21A2.006.

Hurteau MD, Liang S, Westerling AL, Wiedinmyer C (2019) Vegetation-fire feedback reduces projected area burned under climate change. Sci Rep 9: 2838. https://doi.org/10.1038/s41598-019-39284-1.

Intergovernmental Panel on Climate Change (IPCC) (2001) Climate Change 2001: The Scientific Basis: Contribution of Working Group I to the Third Assessment Report of the Intergovernmental Panel on Climate Change, edited by J. T. Houghton et al., 881 pp., Cambridge Univ. Press, New York

Jain P, Castellanos-Acuna D, Coogan SC, Abatzoglou JT, Flannigan MD (2022) Observed increases in extreme fire weather driven by atmospheric humidity and temperature. Nat Clim Chang 12: 63–70. https://doi.org/10.1038/s41558-021-01224-1.

Jensen D, Reager JT, Zajic B, Rousseau N, Rodell M, Hinkley E (2018) The sensitivity of US wildfire occurrence to pre-season soil moisture conditions across ecosystems. Environ Res Lett 13: 014021

Jin Y, Roy D P (2005) Fire-induced albedo change and its radiative forcing at the surface in northern Australia. Geophys Res Lett 32(13): 1–4. https://doi.org/10.1029/2005GL022822

Jin M, Liang S (2006) An improved land surface emissivity parameter for land surface models using global remote sensing observations. J Clim 19(12): 2867–81. https://doi.org/10.1175/JCLI3720.1.

Jin Y, Randerson JT, Faivre N, Capps S, Hall A, Goulden ML (2014) Contrasting controls on wildland fires in southern California during periods with and without Santa Ana winds: controls on southern California fires. J Geophys Res Biogeosciences 119(3): 432–50. https://doi.org/10.1002/2013JG002541.

Jin Y, Randerson JT, Goulden ML, Goetz SJ (2012) Post-fire changes in net shortwave radiation along a latitudinal gradient in boreal North America. Geophys Res Lett 39(13): 1–7. https://doi.org/10.1029/2012GL051790

Jin Y, Randerson JT, Goetz SJ, Beck PSA, Loranty MM, Goulden ML (2012) The influence of burn severity on postfire vegetation recovery and albedo change during early succession in North American boreal forests. J of Geophys Res Biogeosciences 117: G01036. https://doi.org/10.1029/2011JG001886.

Jin Y, Goulden ML, Faivre N, Veraverbeke S, Sun F, Hall A, Hand MS, Hook S, Randerson JT (2015) Identification of two distinct fire regimes in southern California: Implications for economic impact and future change. Environ Res Lett 10(9). https://doi.org/10.1088/1748-9326/10/9/094005

Johnstone JF, Allen CD, Franklin JF, Frelich LE, Harvey BJ, Higuera PE (2016) Changing disturbance regimes, ecological memory, and forest resilience. Frontiers Ecol Environ 14:369–378.

Jolly WM, Cochrane MA, Freeborn PH, Holden ZA, Brown TJ, Williamson GJ, Bowman DM (2015) Climate-induced variations in global wildfire danger from 1979 to 2013. Nat Commun 6: 7537. https://doi.org/10.1038/ncomms8537.

Juras J (1994) Some common features of probability distributions for precipitation. Theor Appl Climatol 49: 69–76. https://doi.org/10.1007/bf00868191.

Keeley JE (2009) Fire intensity, fire severity and burn severity: A brief review and suggested usage. Int J Wildland Fire 18(1): 116. https://doi.org/10.1071/WF07049.

Keeley JE, Safford H, Fotheringham CJ, Franklin J, Moritz M (2009) The 2007 southern California wildfires: Lessons in complexity. J For 107(6): 287–296. https://doi.org/10.1093/jof/107.6.287

Keeley JE, Syphard A (2016) Climate change and future fire regimes: examples from California. Geosciences 6(3): 37. doi:10/3390/geosciences6030037

Keeley JE, Syphard AD (2019) Twenty-first century California, USA, wildfires: Fuel-Dominated vs. wind-dominated fires. Fire Ecol 15: 24. https://doi.org/10.1186/s42408-019-0041-0.

Key C, Benson N (2005) Landscape assessment: ground measure of severity; the Composite Burn Index, and remote sensing of severity, the Normalized Burn Index. In FIREMON: Fire Effects Monitoring and Inventory System (USDA Forest Service, Rocky Mountains Research Station, General Technical Report RMRS-GTR-164-CD LA, pp. 1–51); Fort Collins, CO

Key C (2006) Ecological and sampling constraints on defining landscape fire severity. Fire Ecol 2: 34–59. doi:10.4996/FIREECOLOGY.0202034.

Kinoshita AM, Hogue TS (2011) Spatial and temporal controls on post-fire hydrologic recovery in southern California watersheds. Catena 87(2): 240–252. https://doi.org/10.1016/j.catena.2011.06.005

Krawchuk MA, Moritz MA (2011) Constraints on global fire activity vary across a resource gradient. Ecology 92: 121–132. https://doi.org/10.1890/09-1843.1.

Lawson BD (1977) Fire Weather Index—The basis for Fire Danger Rating in British Columbia; Canadian Fisheries and Environment Canada, Canadian Forestry Service: Victoria, QC, Canada.

Lawson BD, Armitage OB (2008) Weather guide for the Canadian Forest Fire Danger Rating System; Natural Resources Canada, Canadian Forest Service: Edmonton, AB, Canada.

Lenihan JM, Bachelet D, Neilson RP, Drapek R (2008) Response of vegetation distribution, ecosystem productivity, and fire to climate change scenarios for California. Climatic Change 87(Suppl.), 215–230. doi:10.1007/S10584-007-9362-0

Level III and IV Ecoregions of Continental United States. Available online: https://www.epa.gov/eco-research/level-iii-and-iv-ecoregions-continental-united-states (accessed on 20 July 2021).

Li H, Sheffield J, Wood EF (2010) Bias correction of monthly precipitation and temperature fields from Intergovernmental Panel on Climate Change AR4 models using equidistant quantile matching. J Geophys Res 115, D10. https://doi.org/10.1029/2009JD012882.

Lippitt CL, Stow DA, O’Leary JF, Franklin J (2013) Influence of short-interval fire occurrence on post-fire recovery of fire-prone shrublands in California, USA. Int J Wildland Fire 22(2): 184. doi:10.1071/wf10099

Littell JS (2018) Drought and fire in the Western USA: Is climate attribution enough? Curr Clim Chang Rep 4: 396–406. https://doi.org/10.1007/s40641-018-0109-y.

Liu Z, Ballantyne AP, Cooper LA (2018) Increases in land surface temperature in response to fire in Siberian boreal forests and their attribution to biophysical processes. Geophys Res Lett 45(13): 6485–6494. https://doi.org/10.1029/2018GL078283

Lutes DC, Keane RE, Caratti JF, Key CH, Benson NC, Sutherland S, et al. (2006) FIREMON: Fire effects monitoring and inventory system. Gen. Tech. Rep. RMRS-GTR-164-CD. Fort Collins, CO: U.S. Department of Agriculture, Forest Service, Rocky Mountain Research Station.

Lyons EA, Jin Y, Randerson JT (2008) Changes in surface albedo after fire in boreal forest ecosystems of interior Alaska assessed using MODIS satellite observations. J Geophys Res Biogeosciences 113(2): 1–15. https://doi.org/10.1029/2007JG000606

Ma X, Jin J, Liu J, Niu G (2019) An improved vegetation emissivity scheme for land surface modeling and its impact on snow cover simulations. Clim Dyn 53(9–10): 6215–26. https://doi.org/10.1007/s00382-019-04924-9.

McKenzie D, Littell JS (2017) Climate change and the eco-hydrology of fire: Will area burned increase in a warming Western USA? Ecol Appl 27: 26–36. https://doi.org/10.1002/eap.1420.

Meigs GW, Dunn CJ, Parks SA, Krawchuk MA (2020) Influence of topography and fuels on fire refugia probability under varying fire weather conditions in forests of the Pacific Northwest, USA. Canadian J For Res 50(7): 636–647. https://doi.org/10.1139/cjfr-2019-0406.

Meng R, Dennison PE, D'Antonio CM, Moritz MA (2014) Remote sensing analysis of vegetation recovery following short-interval fires in southern California shrublands. PLOS One 9(10): e110637. doi:10.1371/journal.pone.0110637

Meng R, Dennison PE, Huang C, Moritz MA, D'Antonio C (2015) Effects of fire severity and post-fire climate on short-term vegetation recovery of mixed-conifer and red fir forests in the Sierra Nevada mountains of California. Remote Sens of Environ 171: 311–25. https://doi.org/10.1016/j.rse.2015.10.024.

Mesinger F, DiMego G, Kalnay E, Mitchell K (2006) North American Regional Reanalysis. Bull Am Meteorol Soc 87: 343–360. doi:10.1175/BAMS-87-3-343

Meyn A, White PS, Buhk C, Jentsch A (2007) Environmental drivers of large, infrequent wildfires: The emerging conceptual model. Prog Phys Geogr 31: 287–312. https://doi.org/10.1177/0309133307079365.

Miller NL, Schlegel NJ (2006) Climate change projected fire weather sen- sitivity: California Santa Ana wind occurrence. Geophysical Research Letters 33, L15711. doi:10.1029/2006GL025808

Miller JD, Thode AE (2007) Quantifying burn severity in a heterogeneous landscape with a relative version of the delta normalized burn ratio (DNBR). Remote Sens Environ 109(1): 66–80. https://doi.org/10.1016/j.rse.2006.12.006.

Parks S, Dillon G, Miller C (2014) A new metric for quantifying burn severity: The relativized burn ratio. Remote Sensing 6(3): 1827–44. https://doi.org/10.3390/rs6031827.

Parks SA, Parisien MA, Miller C, Dobrowski SZ (2014) Fire activity and severity in the western US vary along proxy gradients representing fuel amount and fuel moisture. PLOS One 9: e99699. https://doi.org/10.1371/journal.pone.0099699.

Parks SA, Miller C, Abatzoglou JT, Holsinger LM, Parisien MA, Dobrowski SZ (2016) How will climate change affect wildland fire severity in the western US? Environ Res Lett 11: 035002. https://doi.org/10.1088/1748-9326/11/3/035002.

Parks SA, Holsinger LM, Panunto MH, Jolly WM, Dobrowski SZ, Dillon GK (2018) High-severity fire: Evaluating its key drivers and mapping its probability across western US forests. Environ Res Lett 13(4): 044037. https://doi.org/10.1088/1748-9326/aab791.

Parks SA, Dobrowski SZ, Panunto MH (2018a) What drives low-severity fire in the southwestern USA? Forests 9(4): 165. doi:10.3390/f9040165.

Petropoulos GP, Griffiths HM, Kalivas DP (2014) Quantifying spatial and temporal vegetation recovery dynamics following a wildfire event in a Mediterranean landscape using EO data and GIS. Appl Geography 50: 120–131.

Rother D, De Sales F (2020) Impact of wildfire on the surface energy balance in six California case studies. Boundary-Layer Meteorol 178: 143-166. https://doi.org/10.1007/s10546-020-00562-5.

Roy D, Lewis P, Justice C (2002) Burned area mapping using multi- temporal moderate spatial resolution data: a bi-directional reflectance model-based expectation approach. Remote Sens Environ 83:263–286

Roy DP, Boschetti L, Justice CO, Ju J (2008) The collection 5 MODIS burned area product - Global evaluation by comparison with the MODIS active fire product. Remote Sens Environ 112(9): 3690–3707. https://doi.org/10.1016/j.rse.2008.05.013

Samain O, Kergoat L, Hiernaux P, Guichard F, Mougin E, Timouk F, Lavenu F (2008) Analysis of the in situ and MODIS albedo variability at multiple timescales in the Sahel. J Geophys Res Atmos 113(14): 1–16. https://doi.org/10.1029/2007JD009174

Schaaf C, Wang Z (2015) MCD43A3 MODIS/Terra+Aqua BRDF/Albedo Daily L3 Global - 500m V006 [Data set]. NASA EOSDIS Land Processes DAAC. Accessed 2019-12-27 from https://doi.org/10.5067/MODIS/MCD43A3.006

Seager R, Hooks A, Williams AP, Cook B, Nakamura J, Henderson N (2015) Climatology, variability, and trends in the U.S. vapor pressure deficit, an important fire-related meteorological quantity. J Appl Meteorol Climatol 54: 1121–1141. https://doi.org/10.1175/JAMC-D-14-0321.1.

Shvetsov EG, Kukavskaya EA, Buryak LV, Barrett K (2019) Assessment of post-fire vegetation recovery in southern Siberia using remote sensing observations. Environ Res Lett 14(5): 055001. https://doi.org/10.1088/1748-9326/ab083d.

Soverel NO, Perrakis DDB, Coops NC (2010) Estimating burn severity from Landsat DNBR and RdNBR indices across western Canada. Remote Sens Environ 114(9): 1896–1909. https://doi.org/10.1016/j.rse.2010.03.013.

Spracklen DV, Mickley LJ, Logan JA, Hudman RC, Yevich R, Flannigan MD, et al. (2009) Impacts of climate change from 2000 to 2050 on wildfire activity and carbonaceous aerosol concentrations in the western United States. J Geophys Res 114(D20), D20301. https://doi.org/10.1029/2008JD010966.

Stevens-Rumann CS, Prichard SJ, Strand EK, Morgan P (2016) Prior wildfires influence burn severity of subsequent large fires. Canadian J For Res 46(11):1375–1385. https://doi.org/10.1139/cjfr-2016-0185

Stull RB (1988) An introduction to boundary layer meteorology. Dordrecht: Kluwer Academic.

Swain DL (2021) A shorter, sharper rainy season amplifies California wildfire risk. Geophys Res Lett 48: e2021GL092843. doi:10/1029/2021GL092843.

Syphard AD, Franklin J, Keeley JE (2006) Simulating the effects of frequent fire on southern California coastal shrublands. Ecol Appl 16(5): 1744–1756. https://doi.org/10.1890/1051-0761(2006)016[1744:STEOFF]2.0.CO;2

Thompson JR, Spies TA (2009) Vegetation and weather explain variation in crown damage within a large mixed-severity wildfire. For Ecol Manag 258: 1684-1694.

Touma D, Stevenson S, Lehner F, Coats S (2021) Human-driven greenhouse gas and aerosol emissions cause distinct regional impacts on extreme fire weather. Nat Commun 12(212). https://doi.org/10.1038/s41467-020-20570-w.

Trouet V, Taylor AH, Carleton AM, Skinner CN (2006) Fire-climate interaction in forests of the American Pacific coast. Geophys Res Lett 33(18). https://doi.org/10.1029/2006GL027502

van Mantgem PJ, Nesmith JCB, Keifer M, Knapp EE, Flint A, Flint L (2013) Climate stress increases forest fire severity across the western United States. Ecol Lett 16(9): 1151–1156. doi:10.1111/ele.12151

van Wagner CE (1987) The development and structure of the Canadian Forest Fire Weather Index System; Canadian Forest Service: Ottawa, ON, Canada.

Van Wagtendonk JW, Root RR, Key CH (2004) Comparison of AVIRIS and Landsat ETM+ detection capabilities for burn severity. Remote Sens Environ 92: 397–408.

Veraverbeke S, Lhermitte S, Verstraeten WW, Goossens R (2010) The temporal dimension of differenced normalized burn ratio (DNBR) fire/burn severity studies: The case of the large 2007 Peloponnese wildfires in Greece. Remote Sens Environ 114(11): 2548–63. https://doi.org/10.1016/j.rse.2010.05.029.

Veraverbeke S, Lhermitte S, Verstraeten WW, Goossens R (2011) A time-integrated MODIS burn severity assessment using the multi-temporal differenced normalized burn ratio (dNBRMT). Int J Appl Earth Obs Geoinformation 13: 52–58. doi:10.1016/J.JAG.2010.06.006.

Veraverbeke S, Verstraeten WW, Lhermitte S, Van De Kerchove R, Goossens R (2012) Assessment of post-fire changes in land surface temperature and surface albedo, and their relation with fire-burn severity using multitemporal MODIS imagery. Int J Wildland Fire 21(3): 243. https://doi.org/10.1071/WF10075

Vlassova L, Pérez-Cabello F, Mimbrero M, Llovería R, García-Martín A (2014) Analysis of the relationship between land surface temperature and wildfire severity in a series of Landsat images. Remote Sens 6(7): 6136–62. https://doi.org/10.3390/rs6076136.

Wang K, Wan Z, Wang P, Sparrow M, Liu J, Haginoya S (2007) Evaluation and improvement of the MODIS Land Surface Temperature/Emissivity products using ground-based measurements at a semi-desert site on the western Tibetan Plateau. Int J Remote Sens 28(11): 2549–65. https://doi.org/10.1080/01431160600702665.

Wang K, Liang S (2009) Evaluation of ASTER and MODIS Land Surface Temperature and Emissivity products using long-term surface longwave radiation observations at SURFRAD sites. Remote Sens Environ 113(7): 1556–65. https://doi.org/10.1016/j.rse.2009.03.009.

Wendt CK, Beringer J, Tapper NJ, Hutley LB (2007) Local boundary-layer development over burnt and unburnt tropical savanna: An observational study. Boundary-Layer Meteorol 124(2): 291–304. https://doi.org/10.1007/s10546-006-9148-3.

Westerling AL, Hidalgo HG, Cayan DR, Swetnam TW (2006) Warming and earlier spring increase western U.S. forest wildfire activity. Science 313(5789): 940–943. https://doi.org/10.1126/science.1128834

Westerling AL, Bryant BP (2008) Climate change and wildfire in California. Climatic Change 87(December 2007). https://doi.org/10.1007/s10584-007-9363-z

Westerling AL, Bryant BP, Preisler HK, Holmes TP, Hidalgo HG, Das T, et al. (2011) Climate change and growth scenarios for California wildfire. Climatic Change 109(S1): 445–63. https://doi.org/10.1007/s10584-011-0329-9.

Williams JW, Jackson ST, Kutzbach JE (2007) Projected distributions of novel and disappearing climates by 2100 AD. Proc Natl Acad Sci USA 104: 5738–5742. https://doi.org/10.1073/pnas.0606292104.

Williams AP, Abatzoglou JT (2016) Recent advances and remaining uncertainties in resolving past and future climate effects on global fire activity. Current Climate Change Reports 2(1): 1–14. https://doi.org/10.1007/s40641-016-0031-0

Williams AP, Abatzoglou JT, Gershunov A, Guzman-Morales J, Bishop DA, Balch JK, Lettenmaier DP (2019) Observed impacts of anthropogenic climate change on wildfire in California. Earth's Future 7: 892-910. https://doi.org/10.1029/2019EF001210

Xia Y, et al. (2012) Continental-scale water and energy flux analysis and validation for the North America Land Data Assimilation System project phase 2 (NLDAS-2): 1. Intercomparison and application of model products. J Geophys Res 117. doi:10.102932011JD016048

Xu M, Liang XZ, Samel A, Gao W (2014) MODIS consistent vegetation parameter specifications and their impacts on regional climate simulations. J Clim 27(22): 8578–8596. https://doi.org/10.1175/JCLI-D-14-00082.1

Xue Y, Sellers PJ, Kinter JL, Shukla J (1991) A simplified biosphere model for global climate studies. J Clim 4(3): 345–364. doi:10.1175/1520-0442(1991)004<0345:asbmfg>2.0.co;2

Yang J, Pan S, Dangal S, Zhang B, Wang S, Tian H (2017) Continental-scale quantification of post-fire vegetation greenness recovery in temperate and boreal North America. Remote Sens Environ 199: 277–290. https://doi.org/10.1016/j.rse.2017.07.022.

Zhang L, Xu Y, Meng C, Li X, Liu H, Wang C (2020) Comparison of statistical and dynamic downscaling techniques in generating high-resolution temperatures in China from CMIP5 GCMs. J Appl Meteorol Climatol 59(2):207–35. https://doi.org/10.1175/JAMC-D-19-0048.1.

Zheng Z, Zeng Y, Li S, Huang W (2016) A new burn severity index based on land surface temperature and enhanced vegetation index. Int J Appl Earth Obs Geoinformation 45: 84-94. http://dx.doi.org/10.1016/j.jag2015.11.002.

Zhong S, Wang T, Sciusco P, Shen M, Pei L, Nikolic J, et al. (2021) Will land use land cover change drive atmospheric conditions to become more conducive to wildfires in the United States?. Int J Climatol 1-20. doi:10.1002/joc.7036.

Zhuang Y, Fu R, Santer BD, Dickinson RE, Hall A (2021) Quantifying contributions of natural variability and anthropogenic forcings on increased fire weather risk over the western United States. Proc Natl Acad Sci USA 118, e2111875118. https://doi.org/10.1073/pnas.2111875118.